UNIVERSITY OF CALIFORNIA, SAN DIEGO

State Preparation and Metrology of Nitrogen Nuclear Spin in Diamond

A dissertation submitted in partial satisfaction of the
requirements for the degree
Doctor of Philosophy

in

Physics

by

Kilhyun Bang

Committee in charge:

Professor Lu Jeu Sham, Chair
Professor Leonid Butov
Professor Young-Han Kim
Professor David Meyer
Professor Congjun Wu

2012

The dissertation of Kilhyun Bang is approved, and it is acceptable in quality and form for publication on microfilm and electronically:

_____

_____

_____

_____

_____

Chair

University of California, San Diego

2012

DEDICATION

To my wife, Lime,

and my father

TABLE OF CONTENTS

LIST OF FIGURES

LIST OF TABLES

ACKNOWLEDGEMENTS

First and foremost, I express my gratitude to my supervisor, Professor Lu Jeu Sham. He has taught me not only physics but also attitudes to be a physicist such as patience and passion. I am grateful to Lu for his patience. I had a few personal stories during my program, and Lu always waited for me to be ready to work. I may not have completed my degree without his thoughtful consideration. Thanks, Lu.

I thank Dr. Wen Yang. He was my mentor as a physicist and a friend. I spent more than two years in the same office with him. He was always willing to help physical problems I faced with. I could not realized how much I helped me until he left. Many parts of this dissertation are the results of the discussion with him. I would also like to thank David Toily. He explained me how diamond experiments work whenever I had problems.

I am also grateful to Professor Leonid Butov, Congjun Wu, David Meyer, and Young-Han Kim for being my thesis committee and spending their valuable time in listening to my talk.

I would like to thank my undergraduate advisor, Professor Byung-Il Min. My adventure in physics began with him. I was a chemistry student and he led me to the world of physics. I have really enjoyed the adventure.

I thank my Korean friends in physics department at UCSD, Diana, Minsu, Jaehyeok, and Sunjae. Without them, I might have felt lonely while I was swimming in physics. It was good to have someone to talk about physics and the future as a physicist in Korean.

I thank my wife and family for encouragement and pray. I am really grateful to my father for every support. I wish I could show this dissertation to him.

Finally, I thank the U. S. Army Research Office for the support during my doctoral program (2009-2012).

The text of chapter 3, in part, is a reprint of the material that is being prepared for publication as Bang, K.; Yang, W.; Sham, L. J. *Optical Initialization of Nitrogen Nuclear Spins in Nitrogen-Vacancy Center*. The co-authors in this publication directed, supervised, and co-worked on the research which forms the basis of this chapter.

The text of chapter 4, in part, is a reprint of the material that has been submitted

for publication as Bang, K.; Yang, W.; Sham, L. J. *Quantum measurement of hyperfine interaction in nitrogen-vacancy center*. The co-authors in this publication directed, supervised, and co-worked on the research which forms the basis of this chapter.

VITA

2006	B. S. in Physics *summa cum laude*, Postech, Pohang, South Korea
2007-2008	Teaching Assistant, Department of Physics, University of California, San Diego
2009-2012	Research Assistant, Department of Physics, University of California, San Diego
2012	Ph. D. in Physics, University of California, San Diego

FIELDS OF STUDY

Major Field: Physics

Studies in Theoretical Condensed Matter Physics

Professor Lu Jeu Sham

ABSTRACT OF THE DISSERTATION

State Preparation and Metrology of Nitrogen Nuclear Spin in Diamond

by

Kilhyun Bang

Doctor of Philosophy in Physics

University of California, San Diego, 2012

Professor Lu Jeu Sham, Chair

A negatively-charged nitrogen-vacancy (NV) center in diamond is a promising system for quantum computation and quantum information. It has the diamond structure with a substitutional nitrogen atom and a neighboring vacancy. An electron spin in the NV center has an exceptionally long coherence time at room temperature. Thus the NV center has a potential to realize a room-temperature quantum computer which is more efficient than a classical computer.

In this dissertation, we focus on the nitrogen nuclear spin as well as the electron spin in the NV center. Every NV center has the nitrogen nuclear spin. Because of the long coherence time of the nitrogen nuclear spin, it is a good candidate for a quantum memory. Thus it is important to prepare the nitrogen nuclear spin qubit in a given pure state for quantum computation. We provide a theoretical understanding of the popular

nuclear spin initialization technique. Furthermore, we propose an optimal condition for the initialization of the nitrogen nuclear spin by including the local strain in the NV center. We expect that this optimal condition can improve the purity of the nuclear spin initialization.

We also propose an efficient quantum measurement protocol for the hyperfine interaction between the electron spin and the ^{15}N nuclear spin in the NV center. A precise knowledge of the hyperfine interaction is important to reduce an error in a coherent control of the ^{15}N nuclear spin. In this protocol, a sequence of quantum operations with successively increasing duration is utilized to estimate the hyperfine interaction with successively higher precision approaching the quantum metrology limit. Unlike common quantum metrological methods, this protocol does not need the preparation of the nuclear spin in a pure state. In the presence of realistic operation errors and electron spin decoherence, we show the overall precision of our protocol still surpasses the standard quantum limit.

Chapter 1

Introduction

Quantum computation is a field of study based on quantum mechanics. Quantum computation utilizes quantum mechanical properties such as superposition and entanglement to accomplish a given task more efficient than classical computers. For example, a quantum computer can estimate a physical parameter more precisely than classical computers with spending the same amount of resources.

The realization of a quantum computer begins from building the smallest unit of quantum computation (*quantum bit* or *qubit*) and manipulating it individually. Like a classical bit, which is the unit of classical computation, a qubit consists of two different states. Thus, in principle, any system with two distinguishable quantum states can become a qubit. So far, the construction and coherent control of qubits have been demonstrated in different physical systems including trapped ions [11], superconductors [10], semiconductor quantum dots [53], and diamond defects [39].

The information in a qubit is expected to be protected against errors during quantum operations. However, qubits in solid-state systems interact with environments, which diminishes or erases the information. This deleterious effect due to the interactions with environments is called decoherence. As a result, most of solid-state qubits such as electron and nuclear spins require low temperatures to surpress decoherence and perform quantum operations. This is one of the main challenges in implementing quantum computers in a real life.

An electron spin of the negatively charged nitrogen-vacancy (NV) center in diamond, however, has a long coherence time ($> 350\ \mu$s) at room temperature. This long

coherence time enables to achieve a coherent control of the electron spin at room temperature since its coherent control in the NV center takes several nanoseconds [39, 67]. Moreover, the NV center has more than one qubit it a unit cell. In addition to the electron spin, it has an intrinsic nitrogen nuclear spin and it can have up to three carbon-13 (^{13}C) nuclear spins. These nuclear spins can also be utilized as qubits. In particular, they can be entangled with the electron spin or to each other at room temperature [22, 51, 50]. Because of these properties of the NV center, the NV center has been a prominent candidate for several applications such as quantum communication [9] and magnetic sensing [46, 63].

Other than the room-temperature controllability of the spins in the NV center, the NV center is a good source of a single photon [40]. This photon can be used as a messenger to transfer information from one NV center to other centers. Recently, the entanglement between the electron spin in the NV center and the emitted photon has been created at low temperature [64]. While a room-temperature entanglement has not been achieved yet, the NV center has a potential to bring a scalable quantum computer to a real life [60].

In this dissertation, we focus on the electron spin and the nitrogen nuclear spin in a single NV center. Nuclear spins are promising applicants for a quantum memory because of their long coherence time. The ^{13}C nuclear spin is easier to access directly by a microwave because of its relatively strong coupling to the electron spin and to the external fields. However, the ^{13}C nuclear spin is also strongly coupled to the environments, which results in its short coherence time as a quantum memory. Also increasing the concentration of ^{13}C in diamond produces a stronger decoherence effect to the electron spin since the ^{13}C nuclear spins in the environment interact with the electron spin in the center. Moreover, the initialization of the ^{13}C nuclear spin is probabilistic rather than deterministic [51]. On the other hand, every NV center has the nitrogen nuclear spin. The nitrogen spin can be initialized deterministically in a given state [38]. Because of its weak coupling to the environments, it is an ideal candidate for a quantum memory. The direct control of the nitrogen nuclear spin with a radio frequency is possible [65], but the indirect methods in manipulating and detecting the nitrogen nuclear spin have been also introduced by means of the hyperfine interaction with the electron spin to increase

the speed of computation [25, 49].

In particular, we are interested in the initialization of the nitrogen nuclear spin. As pointed out by DiVincenzo, the ability to initialize the qubit in a given pure state is one of the most important criteria for the implementation of quantum computation [17]. However, it is very difficult to prepare a spin qubit in a *pure* state. The impurity of the prepared qubit may cause an error of quantum computers. Therefore, it is crucial to prepare a qubit as pure as possible. The nitrogen nuclear spin in the NV center can be deterministically initialized by optical pumping with 98% of success rate [38], but the current theoretical understanding of the initialization mechanism is not complete. Moreover, the current experiments with the nitrogen nuclear spins do not consider the effect of the local strain in initializing the nitrogen nuclear spins. In chapter 3, we first numerically solve the dynamics of the initialization process, then suggest that a better initialization is possible by considering the local strain of the NV center into account.

The other topic in this dissertation is an application of the NV center to quantum metrology. Quantum metrology seeks a quantum measurement method which is more efficient than classical measurement. A efficient method means more precise than classical methods with the same amount of resources. The resources include the number of particles in the measurements, the number of repeated measurements, or time spent during the measurements. Most quantum measurement methods require the qubits in a pure state and the entanglement between them to surpass the classical limit. However, because of the difficulty in initializing qubits and in creating a large-scale entanglement, a quantum measurement protocol with mixed-state qubits is also desired.

In chapter 4, we propose an efficient mixed-state quantum measurement protocol which estimates the hyperfine interaction between the electron spin and ^{15}N nuclear spin. In addition to the reasons why mixed-state quantum metrology is necessary as discussed above, the precise estimation of the hyperfine interaction is also important for the coherent control of the ^{15}N nuclear spin. Since the coupling between the ^{15}N nuclear spin and the external field is weak, its coherent control requires a relatively long duration of the pulse. Thus the detuning (energy mismatch) of the pulse may cause an error in the control of the nuclear spin qubit. By estimating the hyperfine interaction precisely, the accuracy of the control and the fidelity of the qubit can be improved. Our

protocol has several advantages over common quantum estimation methods. First, the protocol does not need a preparation of the nitrogen nuclear spin, which removes the difficulty of its initialization. Even if we have an impure qubit at the beginning, our protocol can estimate the hyperfine interaction more precise than the classical limit by the benefit of quantum mechanics. Next, the protocol does not need an entanglement, which is a common source in quantum metrology. The model utilizes the time τ of a sequence of quantum operations as well as the number N of repeated sequences to increase the precision of the estimation. While in the classical limit the standard deviation of the estimation is proportional to $1/\sqrt{N}$, the quantum operations in time τ enables the standard deviation to decrease faster as $1/\tau$ instead of the equivalent classical limit of $1/\sqrt{\tau}$. Thus, total estimation result is more precise than the classical limit. Finally, by taking a basic operation error and decoherence into account, we prove that the proposed protocol is feasible at room temperature.

Chapter 2

Electron spin qubit in diamond and its control

2.1 Qubit

The *bit* is the smallest unit of classical computation. It has either 0 or 1 as its value. In quantum computation, the smallest unit is the *quantum bit* or *qubit*. A qubit has two quantum mechanical states $|0\rangle$ and $|1\rangle$, which correspond to 0 and 1 of a bit. The difference between bits and qubits is that a qubit can be in both $|0\rangle$ and $|1\rangle$ states at the same time. One example of such a state is

$$|+\rangle = \frac{1}{\sqrt{2}} \left(|0\rangle + |1\rangle\right).$$

This is a pure quantum state which is different from $|0\rangle$ and $|1\rangle$. It is a linear combination of $|0\rangle$ and $|1\rangle$. A linear combination is one of the most important property of a qubit. Most quantum algorithms require a linear combination of a single qubit or multiple qubits to outperform classical algorithms [52].

A general state of a qubit is written as

$$|\psi\rangle = \alpha\,|0\rangle + \beta\,|1\rangle\,, \tag{2.1}$$

where $\alpha, \beta \in \mathbb{C}$ and $|\alpha|^2 + |\beta|^2 = 1$. Eq. (2.1) is also expressed as

$$|\psi\rangle = \cos\frac{\theta}{2}\,|0\rangle + e^{i\phi} \sin\frac{\theta}{2}\,|1\rangle \tag{2.2}$$

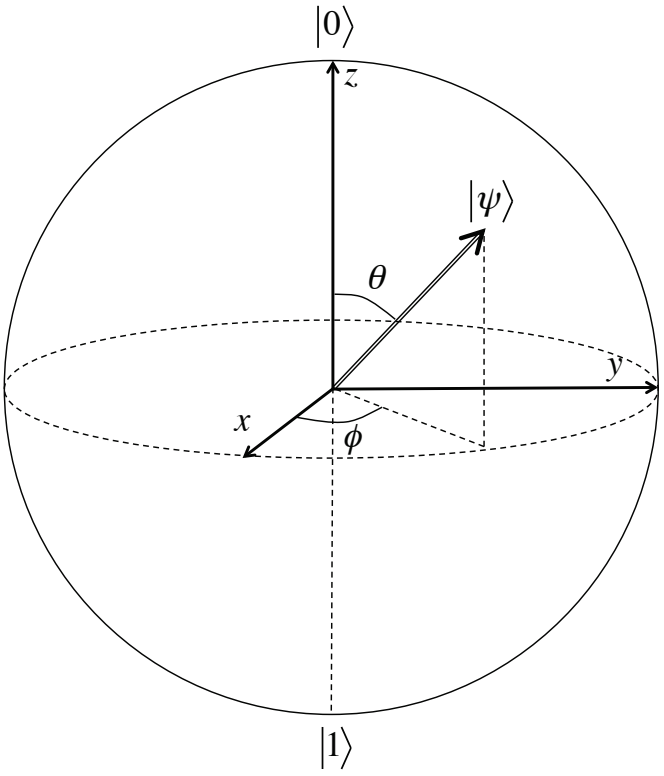

Figure 2.1: Bloch sphere representation of a qubit.

where $\theta, \phi \in \mathbb{R}$. Thus $|\psi\rangle$ can be represented by a radial vector pointing on the unit sphere. This sphere is called the Bloch sphere (Fig. 2.1). The Bloch sphere is useful to understand quantum operations on a qubit.

2.2 Nitrogen-vacancy center in diamond: Overview

The electron spin of a negatively charged nitrogen-vacancy (NV) center in diamond has fascinating properties as a qubit. The NV center consists of a substitutional nitrogen impurity and a neighboring vacancy with an excess electron in diamond structure (Fig. 2.2). The electron spin has well-separated energy levels under an external magnetic field. It is initialized in a given pure state by optical pumping [36]. It can be coherently controlled by a microwave [39]. Its state can be detected optically [35, 40]. Moreover, the electron spin in the NV center has an exceptionally long coherence time $T_2^e \geq 350$ μs at room temperature [3, 29]. This long coherence time makes the initial-

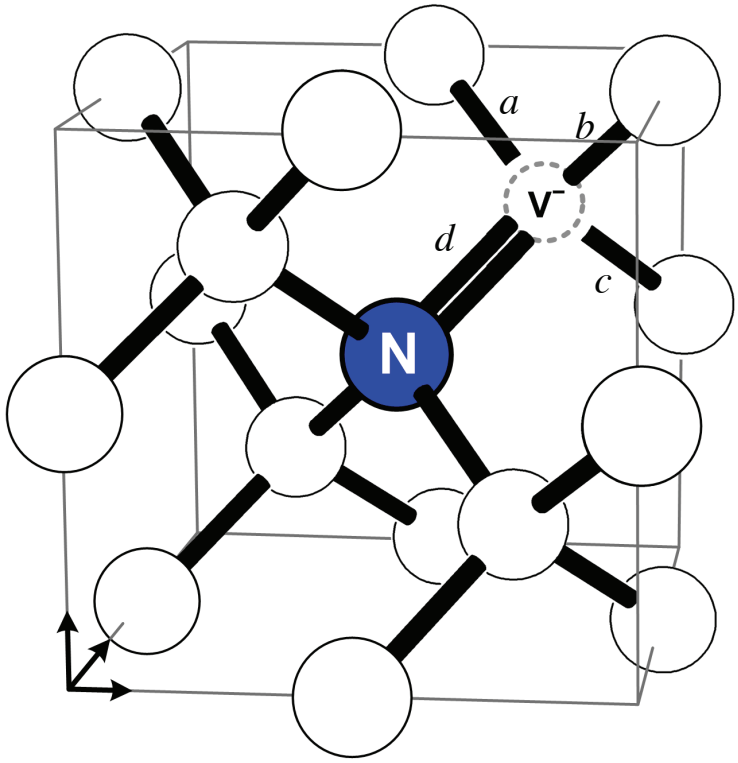

Figure 2.2: A negatively charged nitrogen-vacancy center in diamond.

ization, control, and readout of the electron spin possible at room temperature.

In addition to the electron spin, the NV center can have up to four nuclear spins in a unit cell: one nitrogen nuclear spin (either ^{14}N or ^{15}N) and up to three carbon nuclear spins (^{13}C). These nuclear spins are coupled to the electron spin by the hyperfine interaction and show distinguishable energy levels. Thus a coherent control of the nuclear spins are possible at room temperature directly or indirectly [8, 22, 25]. Furthermore, the entanglement between the electron spin and the carbon nuclear spins can be created in the NV center [51].

2.3 Electronic structure of NV center

The electronic structure of the NV center has been intensively studied with group theory and with first-principle calculation [18, 19, 30, 43, 44, 45]. In this section, we follow the reference [44, 45] and briefly explain the electronic structure of the NV center

up to orbital level.

The NV center has six electrons and four sp^3 orbitals (a, b, c, and d in Fig. 2.2). These four orbitals are not orthonormal, but they can be normalized by considering the symmetry of the NV center. For convenience, we take the symmetry axis of the NV center as $\hat{z}$-axis. From a three-fold rotational symmetry (C_{3v}) of the NV center with respect to the $\hat{z}$-axis, two basis orbitals with C_{3v} symmetry can be constructed by

$$v = (a + b + c)/\sqrt{3 + 6S},$$
$$u = (d - \lambda v)/\sqrt{1 - \lambda^2},$$

where $S = \langle a|b\rangle$ and $\lambda = \langle d|v\rangle$ are overlap integrals. Other two basis orbitals, which are orthonormal to u and v,

$$e_X = (2c - a - b)\sqrt{6 - 6S},$$
$$e_Y = (a - b)\sqrt{2 - 2S},$$

have a directional property. u is mostly localized on the nitrogen and thus has the lowest energy. The energy of v is lower than e_X and e_Y since v has a higher symmetry.

2.3.1 Ground state

The ground-state electron spin configuration is $u^2v^2e_Xe_Y$, depicted in Fig 2.3. We consider only the lone-pair electrons to build the wave functions for the NV center. It is

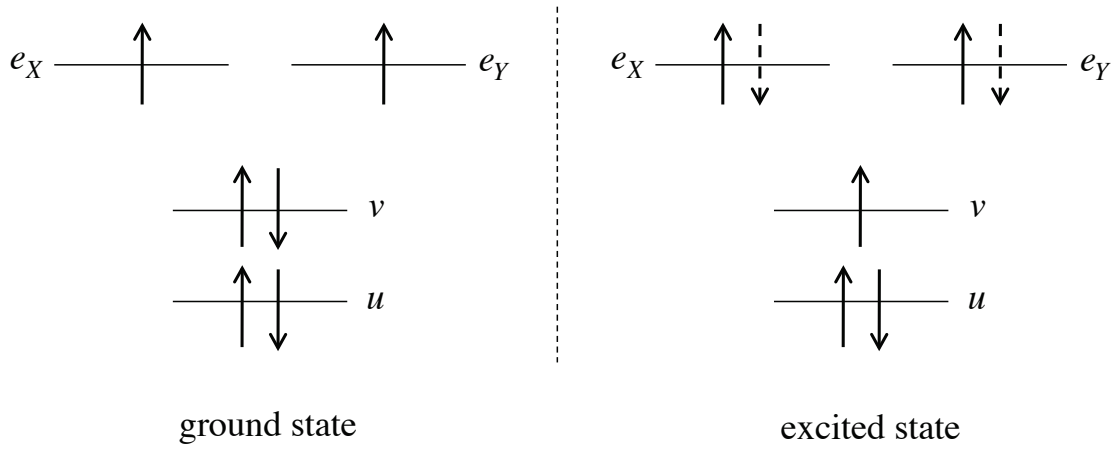

Figure 2.3: Electron spin configuration of the ground state and the lowest excited state in the NV center.

known from experiments and first-principle calculation that the ground state of the NV center is spin triplet. Thus the orbital state of the ground state is given by

$$\left|\Phi_{A_2}\right\rangle = \frac{1}{\sqrt{2}} \left|e_X e_Y - e_Y e_X\right\rangle .$$

The subscript A_2 denotes that Φ_{A_2} transforms as A_2 symmetry (+1 under the C_{3v} rotation and -1 under the reflection σ). The total wave functions for the ground state can be obtained by a product of the orbital wave function and the spin triplet states,

$$\begin{aligned}
|\Psi_+\rangle &= \left|\Phi_{A_2}\right\rangle \otimes |\uparrow\uparrow\rangle , \\
|\Psi_0\rangle &= \left|\Phi_{A_2}\right\rangle \otimes \frac{1}{\sqrt{2}} \left(|\uparrow\downarrow\rangle + |\downarrow\uparrow\rangle\right) , \\
|\Psi_-\rangle &= \left|\Phi_{A_2}\right\rangle \otimes |\downarrow\downarrow\rangle .
\end{aligned}$$

The spin-orbit coupling

$$\hat{H}_{so} = \frac{1}{2m_e^2 c^2} \sum_j \left[\vec{\nabla}\hat{V}_e(\vec{r}_j) \times \vec{p}_j\right] \cdot \vec{s}_j$$

and the spin-spin coupling

$$\hat{H}_{ss} = \frac{1}{2} \frac{\mu_0 g_e^2 \mu_B^2}{4\pi\hbar^2} \sum_{i \neq j} \left[\frac{\vec{s}_i \cdot \vec{s}_j}{|r_{ij}|^3} - \frac{3(\vec{s}_i \cdot \vec{r}_i)(\vec{s}_j \cdot \vec{r}_j)}{|r_{ij}|^5}\right]$$

give the perturbation to the NV center and lift degeneracy. Reference [44] has shown that the diagonal matrix elements of $\hat{H}_{so}$ vanish in the ground state . On the other hand, $\hat{H}_{ss}$ brings the energy splitting to the ground state

$$D_{\mathrm{GS}} = \langle\Psi_\pm| \hat{H}_{ss} |\Psi_\pm\rangle - \langle\Psi_0| \hat{H}_{ss} |\Psi_0\rangle .$$

Therefore, along with the Zeeman interaction, the ground-state Hamiltonian of the electron spin is effectively written as

$$\hat{H}^e_{\mathrm{GS}} = D_{\mathrm{GS}} \hat{S}_z + g_e \mu_B \vec{B} \cdot \vec{S}. \tag{2.3}$$

Under the external magnetic field along the $\hat{z}$-axis, the energy levels of $|m_s\rangle$ are well-separated. Thus, two of three states can be chosen as a qubit.

There is also a spin singlet state in the $u^2v^2e_Xe_Y$ configuration. From group theory, the total wave functions of the singlet state are written as

$$\begin{aligned}
\left|\Psi_{A_1}\right\rangle &= \frac{1}{\sqrt{2}}\left|e_Xe_X + e_Ye_Y\right\rangle \otimes \frac{1}{\sqrt{2}}\left(\left|\uparrow\downarrow\right\rangle - \left|\downarrow\uparrow\right\rangle\right), \\
\left|\Psi_{E_X}\right\rangle &= \frac{1}{\sqrt{2}}\left|e_Xe_Y + e_Ye_X\right\rangle \otimes \frac{1}{\sqrt{2}}\left(\left|\uparrow\downarrow\right\rangle - \left|\downarrow\uparrow\right\rangle\right), \\
\left|\Psi_{E_Y}\right\rangle &= \frac{1}{\sqrt{2}}\left|e_Xe_X - e_Ye_Y\right\rangle \otimes \frac{1}{\sqrt{2}}\left(\left|\uparrow\downarrow\right\rangle - \left|\downarrow\uparrow\right\rangle\right).
\end{aligned}$$

These levels are located between the ground state and the optical excited state. The singlet states are not used as a qubit, but they have an important role in the initialization of the electron spin. Several studies have discussed the energy levels and properties of the singlet states [2, 16, 43, 45, 56].

2.3.2 Excited state

The electron configuration of the lowest excited state is $u^2ve_X^2e_Y$ or $u^2ve_Xe_Y^2$ (Fig. 2.3). Since the excited state is also known as a spin triplet, the orbital wave function of the excited state can be written as

$$\begin{aligned}
\left|\Phi'_X\right\rangle &= \frac{1}{\sqrt{2}}\left|ve_X - e_Xv\right\rangle, \\
\left|\Phi'_Y\right\rangle &= \frac{1}{\sqrt{2}}\left|ve_Y - e_Yv\right\rangle.
\end{aligned}$$

The corresponding total wave functions are

$$\begin{aligned}
\left|\Psi'_{X(Y)+}\right\rangle &= \left|\Phi'_{X(Y)}\right\rangle \otimes \left|\uparrow\uparrow\right\rangle, \\
\left|\Psi'_{X(Y)0}\right\rangle &= \left|\Phi'_{X(Y)}\right\rangle \otimes \frac{1}{\sqrt{2}}\left(\left|\uparrow\downarrow\right\rangle + \left|\downarrow\uparrow\right\rangle\right), \\
\left|\Psi'_{X(Y)-}\right\rangle &= \left|\Phi'_{X(Y)}\right\rangle \otimes \left|\downarrow\downarrow\right\rangle.
\end{aligned}$$

The symmetrized eigenstates can be obtained by taking a linear combination of the above primitive wave functions.

In the excited state, the spin-orbit coupling $\hat{H}_{so}$ gives nonzero energy shifts in the first order perturbation [5, 44]. At room temperature, however, the spin-orbit splitting is quenched by time averaging of the two orbital branches [19, 58]. Since we are interested

in the room-temperature properties and applications of the NV center, we do not include the spin-orbit coupling in our studies.

The resemblance between the ground-state wave functions and the excited-state wave functions implies that the spins-spin interaction $\hat{H}_{ss}$ lifts degeneracy of the excited state and produces a zero-field splitting

$$D_{\mathrm{ES}} = \langle \Psi_{X(Y)\pm} | \hat{H}_{ss} | \Psi_{X(Y)\pm} \rangle - \langle \Psi_{X(Y)0} | \hat{H}_{ss} | \Psi_{X(Y)0} \rangle .$$

Hence the excited-state Hamiltonian of the electron spin under the external magnetic field is given by

$$\hat{H}^{e}_{\mathrm{ES}} = D_{\mathrm{ES}} \hat{S}_z + g_e \mu_B \vec{B} \cdot \vec{S}. \tag{2.4}$$

Under the magnetic field $\vec{B} = B\hat{z}$, $|m_s\rangle$ is an eigenstate of $\hat{H}^{e}_{\mathrm{ES}}$ with an orbital doublet, and their energies are well-separated. Thus two of these states can be selected as the excited-state electron qubit.

2.4 Initialization of the electron spin qubit

Fig. 2.4 illustrates the electronic structure of the NV center discussed in the previous section. The excited state is located 1.945 eV (637 nm) higher than the ground state [40]. As mentioned above, the electron spin of the NV center in the ground state and the optically excited state has a spin triplet ($S = 1$). The excited state is also an orbital doublet, but this doublet is averaged at room temperature [58]. Thus the electron spin in both the ground state and the excited state can be described with the basis $\{|m_s = 0\rangle, |m_s = \pm 1\rangle\}$ under the external magnetic field aligned along the $\hat{z}$-axis [19, 26, 58].

The most popular technique for the initialization of the electron spin in the NV center is optical pumping. The 532 nm laser pumps the electron spin to the phonon-sideband of the excited state, and the electron spin quickly sits onto the excited state [8]. The electron spin m_s is conserved during optical pumping.

The electron spin in the excited state experiences two different decay process. First, the electron spin in both $|m_s = 0\rangle_{\mathrm{ES}}$ and $|m_s = \pm 1\rangle_{\mathrm{ES}}$ optically decays to the ground state with emitting a photon, and the electron spin is conserved during the decay. At the

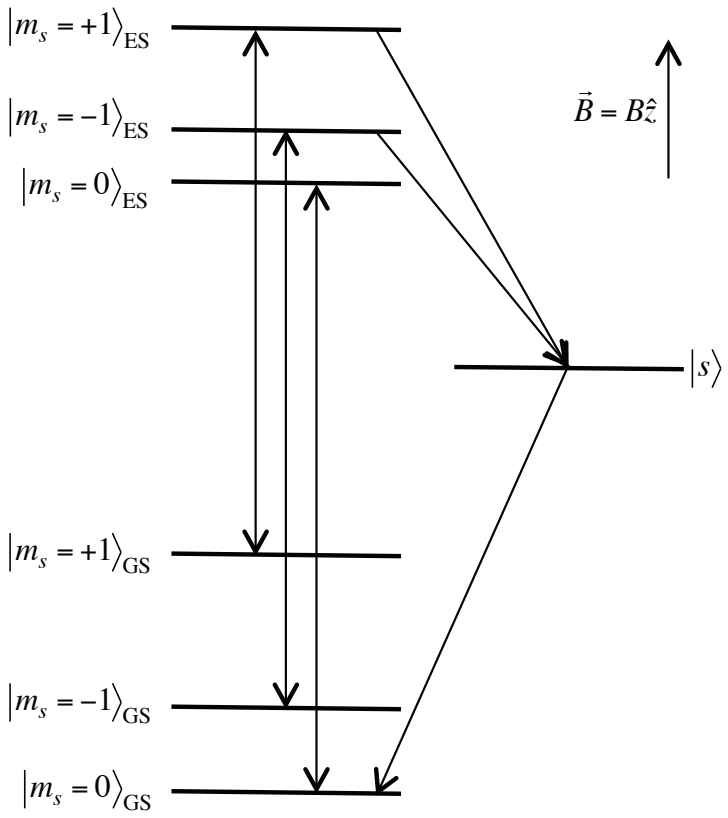

Figure 2.4: Electronic structure of the NV center under an external magnetic field $\vec{B} = B\hat{z}$. Both the ground state and the excited state have $S = 1$. While optical transitions are spin conserving, the decay from $|m_s = \pm 1\rangle_{ES}$ to $|m_s = 0\rangle_{GS}$ via $|s\rangle$ is nonradiative.

same time, the electron spin in $|m_s = \pm 1\rangle_{ES}$ experiences the nonradiative intersystem decay to the singlet state $|s\rangle$, and the electron spin in the singlet state relaxes to the ground state $|m_s = 0\rangle_{GS}$. Since the intersystem decay is a spin-selective process, the unpolarized electron spin is initialized in $|m_s = 0\rangle_{GS}$ with several cycles of optical pumping and the intersystem decay. The timescale of the initialization process is a few microseconds [8].

2.5 Coherent control of the electron spin

The coherent control of the qubit is an essential technique in quantum computation. For the NV center, the electron spin can be coherently controlled by a classical microwave. To illustrate the coherent control of the electron spin, we take $|0\rangle \equiv |m_s = 0\rangle_{GS}$ and $|1\rangle \equiv |m_s = -1\rangle_{GS}$ as the qubit states. We assume that the external magnetic field

$\vec{B} = B\hat{z}$ is strong enough to move the $|m_s = +1\rangle_{\mathrm{GS}}$ state away from the other states.

The interaction between the electron spin and the classical microwave with the frequency ω is, after rotating wave approximation [47], written as

$$\hat{V}(t) = \frac{i\Omega}{2}\left(e^{-i\omega t}\,|1\rangle\langle 0| - e^{i\omega t}\,|0\rangle\langle 1|\right). \tag{2.5}$$

Here Ω denotes the coupling strength between the electron spin and the microwave, which is called the Rabi frequency. The Hamiltonian of the electron spin within the $\{|0\rangle, |1\rangle\}$ subspace is given by

$$\hat{H}_0 = -\frac{\omega_0}{2}\,|0\rangle\langle 0| + \frac{\omega_0}{2}\,|1\rangle\langle 1|, \tag{2.6}$$

where $\omega_0 = D_{\mathrm{GS}} - g_e\mu_B B$ is the energy difference between $|0\rangle$ and $|1\rangle$. The total Hamiltonian of the system is then $\hat{H} = \hat{H}_0 + \hat{V}(t)$.

The state of the qubit $|\psi\rangle$ is governed by the Schrödinger equation ($\hbar = 1$)

$$i\frac{d}{dt}\,|\psi(t)\rangle = \left(\hat{H}_0 + \hat{V}(t)\right)|\psi(t)\rangle. \tag{2.7}$$

The qubit in an arbitrary state can be written as

$$|\psi(t)\rangle = \alpha(t)\,|0\rangle + \beta(t)\,|1\rangle.$$

With $\tilde{\alpha}(t) = \alpha(t)e^{-i\omega t}$ and $\tilde{\beta}(t) = \beta(t)e^{i\omega t}$, the Schrödinger equation becomes

$$i\frac{d}{dt}\begin{bmatrix}\tilde{\alpha}(t)\\ \tilde{\beta}(t)\end{bmatrix} = \frac{1}{2}\begin{bmatrix}\delta & -i\Omega\\ i\Omega & -\delta\end{bmatrix}\begin{bmatrix}\tilde{\alpha}(t)\\ \tilde{\beta}(t)\end{bmatrix} = \hat{V}_I\begin{bmatrix}\tilde{\alpha}(t)\\ \tilde{\beta}(t)\end{bmatrix} \tag{2.8}$$

with the basis $\{|0\rangle, |1\rangle\}$, where $\delta = \omega - \omega_0$ is the detuning of the microwave.

If the frequency of the microwave is resonant with the energy splitting of the qubit (*i.e.* $\delta = 0$), the solution of Eq. (2.8) is

$$\begin{bmatrix}\tilde{\alpha}(t)\\ \tilde{\beta}(t)\end{bmatrix} = \begin{bmatrix}\cos\frac{\theta}{2} & -\sin\frac{\theta}{2}\\ \sin\frac{\theta}{2} & \cos\frac{\theta}{2}\end{bmatrix}\begin{bmatrix}\tilde{\alpha}(t_0)\\ \tilde{\beta}(t_0)\end{bmatrix}, \tag{2.9}$$

where $\theta = \Omega(t - t_0)$. This is simply a rotation of the qubit along the y-axis on the Bloch sphere (Fig. 2.5). The rotation angle can be controlled by the duration $t - t_0$ of the microwave. For example, if $|\psi(t_0)\rangle = |0\rangle$, we have $|\psi(t)\rangle = |1\rangle$ by choosing t such that $t - t_0 = \pi/\Omega$. The resonant microwave pulse with the duration of $t_0 + \pi/\Omega$ is called a

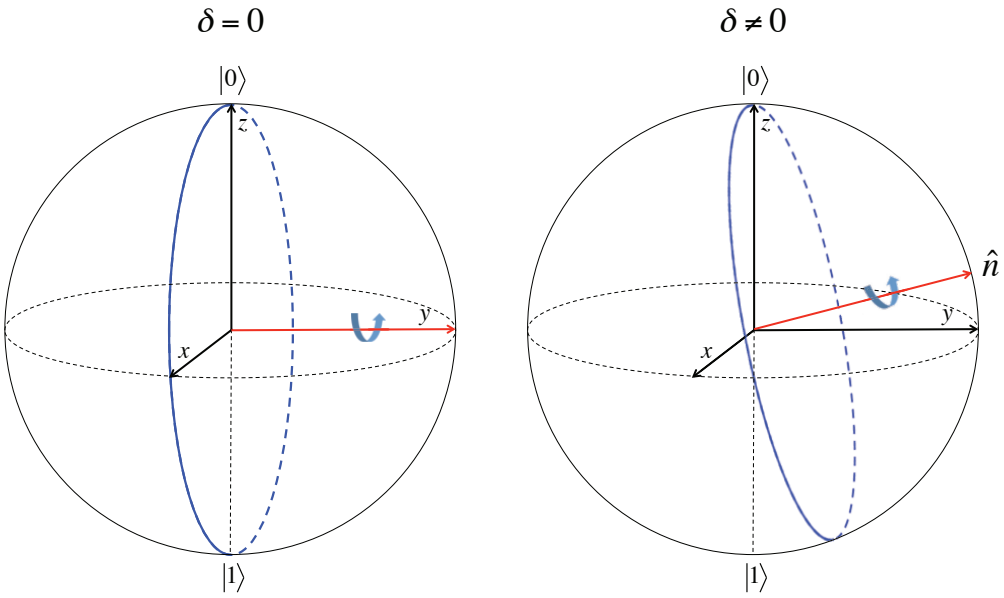

Figure 2.5: Coherent control of a qubit on the Bloch sphere for $\delta = 0$ and $\delta \neq 0$

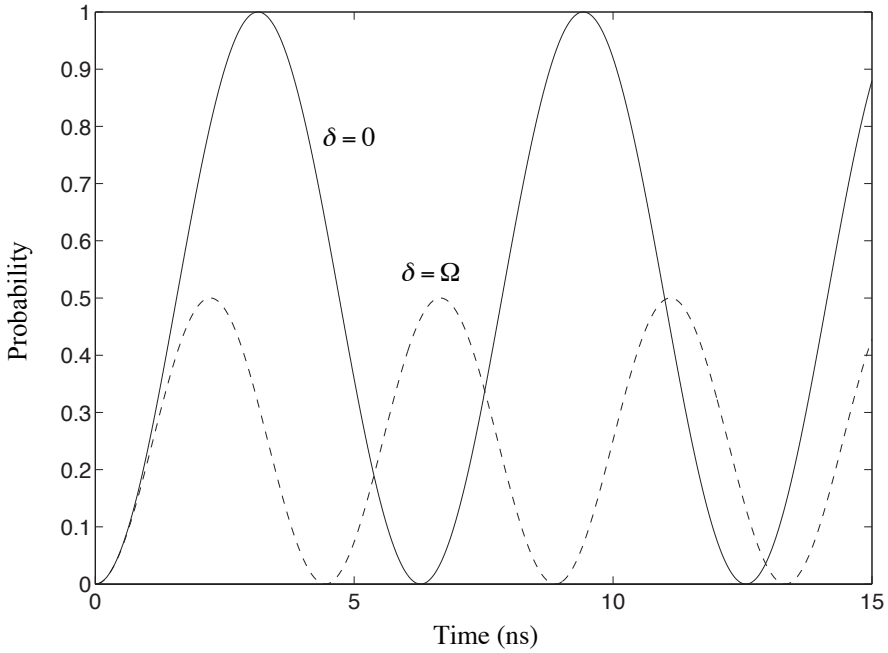

Figure 2.6: Probability $|\beta(t)|^2$ for the qubit to be found in $|1\rangle$. In the calculation, $\beta(0) = 0$ and $\Omega = 1$ GHz.

π-pulse. In this way, the qubit can be coherently controlled from one state to another state. For the NV center, it takes a few nanoseconds to rotate the qubit from $|0\rangle$ to $|1\rangle$ with $\Omega = 1$ GHz as depicted in Fig. 2.6.

The analytic solution of Eq. (2.8) is also available for $\delta \neq 0$. The interaction $\hat{V}_I$ is decomposed as

$$\hat{V}_I = \frac{1}{N^2}\begin{bmatrix} i\Omega & -\delta - \Omega_R \\ \delta + \Omega_R & -i\Omega \end{bmatrix}\begin{bmatrix} -\Omega_R & 0 \\ 0 & \Omega_R \end{bmatrix}\begin{bmatrix} -i\Omega & \delta + \Omega_R \\ -\delta - \Omega_R & i\Omega \end{bmatrix}. \tag{2.10}$$

where $\Omega_R = \sqrt{\Omega^2 + \delta^2}$ and $N = \sqrt{2\Omega_R(\Omega_R + \delta)}$. Since $\hat{V}_I$ is time independent, the solution of Eq. (2.8) is given by

$$\begin{bmatrix} \tilde{\alpha}(t) \\ \tilde{\beta}(t) \end{bmatrix} = \exp\left(-i\hat{V}_I \frac{t - t_0}{2}\right)\begin{bmatrix} \tilde{\alpha}(t_0) \\ \tilde{\beta}(t_0) \end{bmatrix}. \tag{2.11}$$

Using Eq. (2.10), the solution becomes

$$\begin{aligned}\begin{bmatrix} \tilde{\alpha}(t) \\ \tilde{\beta}(t) \end{bmatrix} &= \begin{bmatrix} \cos\left(\frac{\Omega_R(t-t_0)}{2}\right) - i\frac{\delta}{\Omega_R}\sin\left(\frac{\Omega_R(t-t_0)}{2}\right) & -\frac{\Omega}{\Omega_R}\sin\left(\frac{\Omega_R(t-t_0)}{2}\right) \\ \frac{\Omega}{\Omega_R}\sin\left(\frac{\Omega_R(t-t_0)}{2}\right) & \cos\left(\frac{\Omega_R(t-t_0)}{2}\right) + i\frac{\delta}{\Omega_R}\sin\left(\frac{\Omega_R(t-t_0)}{2}\right) \end{bmatrix}\begin{bmatrix} \tilde{\alpha}(t_0) \\ \tilde{\beta}(t_0) \end{bmatrix} \\ &= \begin{bmatrix} \cos\left(\frac{\theta}{2}\right) - in_z\sin\left(\frac{\theta}{2}\right) & -n_y\sin\left(\frac{\theta}{2}\right) \\ n_y\sin\left(\frac{\theta}{2}\right) & \cos\left(\frac{\theta}{2}\right) + in_z\sin\left(\frac{\theta}{2}\right) \end{bmatrix}\begin{bmatrix} \tilde{\alpha}(t_0) \\ \tilde{\beta}(t_0) \end{bmatrix}\end{aligned} \tag{2.12}$$

The geometrical meaning of Eq. (2.12) is a rotation of the qubit along a rotational axis $\hat{n} = n_y\hat{y} + n_z\hat{z}$ with an angle θ on the Bloch sphere (Fig. 2.5) [59]. The detuning δ causes a deviation of the rotational axis from $\hat{y}$ to $\hat{n}$ and changes the rotational frequency to Ω_R. As a result, a complete electron spin-flip $|0\rangle \leftrightarrow |1\rangle$ cannot be achieved with an off-resonant microwave (Fig. 2.6). It is important to tune the pulse at the resonant frequency to reduce an error in a coherent rotation.

2.6 Readout of the electron spin state

At room temperature, a readout of the electron spin in the NV center can be achieved by measuring a fluorescence signal from the NV center. First, the 532 nm laser is used to pump the electron spin to the excited state (Fig. 2.7). Then the electron spin emits a photon when it decays optically, while it does not when it experiences the intersystem decay through the singlet state. The laser is applied for several microseconds

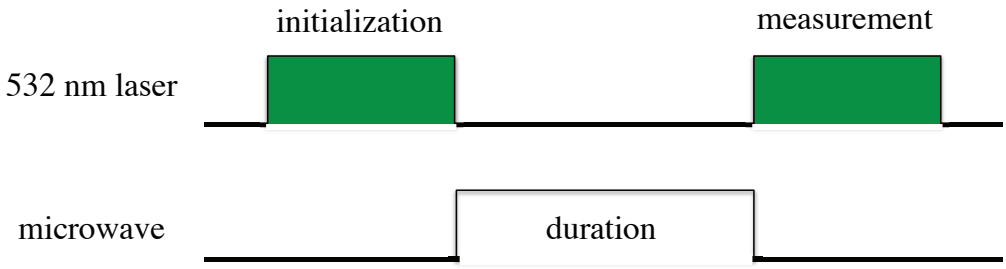

Figure 2.7: Pulse sequence for the initialization, operation, and measurement of the electron spin qubit in the NV center.

to make the electron spin cycle, and a photon detector counts the number of photons during this procedure. The fluorescence signal F (or the number of photons) is proportional to the population of $|m_s = 0\rangle$ in the ground state. Therefore, if the fluorescence signal is measured as a function of the duration of the resonant microwave pulse, the result becomes a sinusoidal function like the $\delta = 0$ graph in Fig. 2.6. By renormalizing the fluorescence signal as $\max(F) \rightarrow 0$ and $\min(F) \rightarrow 1$, it is possible to estimate the average value of the population in $|m_s = 0\rangle$.

The fluorescence measurement is not a single-shot readout of the qubit state – it provides the *average* value of the population. A single-shot readout of the electron spin state at room temperature has not been accomplished yet. However, a single-shot readout of the electron spin has been done at low temperature with the resonant 637 nm laser [7, 57]. A room-temperature single-shot readout of the electron spin state in the NV center is a challenging problem.

Chapter 3

Optical Initialization of Nitrogen Nuclear Spins in Nitrogen-Vacancy Center

The nitrogen nuclear spin of the nitrogen-vacancy center in the diamond is a good candidate for quantum memory because of its long lifetime at room temperature ($\sim$ 1 s) [49]. However, it is hard to directly access due to its weak coupling to the external fields. For this reason, techniques of indirect control and readout of the nitrogen nuclear spin through its hyperfine interaction with the NV center electron spin have been developed recently [25, 49]. The first step in this development is dynamic nuclear spin polarization, in which the nitrogen nuclear spin is prepared into a given Zeeman sublevel in an external magnetic field. This has been achieved by optical pumping of the electron spin at the level anticrossing point of the orbital excited state [26, 38, 61, 62]. In a typical NV center, the local strain is unavoidable. It leads to additional electron energy level splitting and has a strong influence on the optical pumping and hence dynamic polarization of the nitrogen nuclear spin. However, this issue remains unexplored so far.

In this chapter, we provide a theory (based on the Lindblad equation of motion of the electron-nuclear spin system) for the dynamic polarization of the ^{15}N nuclear spin in the NV center. Our theory shows that in the presence of local strain, the maximal degree of ^{15}N polarization is achieved away from the electron spin level anticrossing point, in contrast to previous understanding. We further show that the same conclusion

is true for the dynamic polarization of the ^{14}N nuclear spin in the NV center.

3.1 Initialization mechanism of ^{15}N nuclear spin

The initialization mechanism of the electron spin is explained in chapter 2. We use $|0\rangle \equiv |m_s = 0\rangle$ and $|\pm1\rangle \equiv |m_s = \pm1\rangle$ as a basis of the electron spin qubit. In this section, we explain the physics of the optical pumping induced dynamic polarization of the electron spin and the ^{15}N nuclear spin as outlined in Ref. [38].

The ^{15}N nuclear spin-1/2 (with two Zeeman sublevels $|\uparrow\rangle$ and $|\downarrow\rangle$ in the external magnetic field) is coupled to the electron spin through the hyperfine interaction and provides an additional energy splitting to $|\pm1\rangle_{\mathrm{GS}}$ and $|\pm1\rangle_{\mathrm{ES}}$. The hyperfine interaction strength $A_{\mathrm{ES}} = 61$ MHz in the excited state (ES) is much stronger than that ($A_{\mathrm{GS}} = 3.0$ MHz) in the ground state (GS) [26]. This feature is the key for the dynamic polarization of the ^{15}N nuclear spin [38]. The external magnetic field shifts $|+1\rangle_{\mathrm{ES}}$ away from other two ESs, so that the spin-flip transition $|+1,\downarrow\rangle_{\mathrm{ES}} \leftrightarrow |0,\uparrow\rangle_{\mathrm{ES}}$ induced by the hyperfine interaction is negligible compared to the transition $|0,\downarrow\rangle_{\mathrm{ES}} \leftrightarrow |-1,\uparrow\rangle_{\mathrm{ES}}$. Thus, in this section, we focus on the $\{|0\rangle_{\mathrm{ES}}, |-1\rangle_{\mathrm{ES}}\}$ subspace to explain the dynamic polarization of the ^{15}N nuclear spin.

Under an external magnetic field along the N-V axis (defined as the z axis), the ES Hamiltonian of the NV center is given by

$$\begin{aligned} \hat{H}_{\mathrm{ES}} &= \hat{H}_0 + \hat{H}_\perp \\ H_0 &= D_{\mathrm{ES}}\hat{S}_z^2 + g_e\mu_B B\hat{S}_z + A_{\mathrm{ES}}\hat{S}_z\hat{I}_z \\ \hat{H}_\perp &= A'_{\mathrm{ES}}\frac{\hat{S}_+\hat{I}_- + \hat{S}_-\hat{I}_+}{2} \end{aligned} \tag{3.1}$$

where $D_{\mathrm{ES}} = 1.43$ GHz is the zero-field splitting, $g_e = 2.01$ is the electron g-factor [26], and $A'_{\mathrm{ES}} = 41$ MHz is the transverse hyperfine interaction strength [31], which differs from the longitudinal hyperfine interaction strength $A_{\mathrm{ES}} = 61$ MHz. In the absence of $\hat{H}_\perp$, the energy difference between $|0,\downarrow\rangle_{\mathrm{ES}}$ and $|-1,\uparrow\rangle_{\mathrm{ES}}$ is $\delta_0(B) \equiv D_{\mathrm{ES}} - g_e\mu_B B - A_{\mathrm{ES}}/2$. They cross each other at the critical magnetic field $B_{\mathrm{LAC}} \approx 500$ G determined by $\delta_0(B_{\mathrm{LAC}}) = 0$. Within the subspace $\{|0\rangle_{\mathrm{ES}}, |-1\rangle_{\mathrm{ES}}\}$, the presence of $\hat{H}_\perp$ mixes $|0,\downarrow\rangle_{\mathrm{ES}}$ and

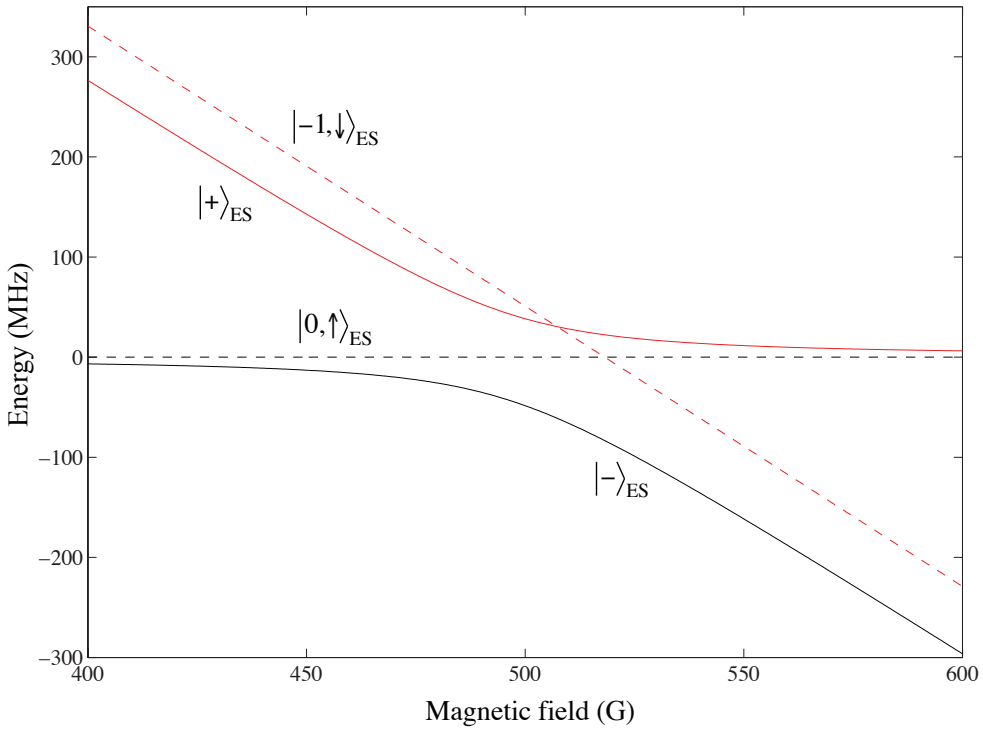

Figure 3.1: Eiegenenergies of the excited-state Hamiltonian $\hat{H}_{ES}$ within $\{|0\rangle_{ES}, |-1\rangle_{ES}\}$ subspace.

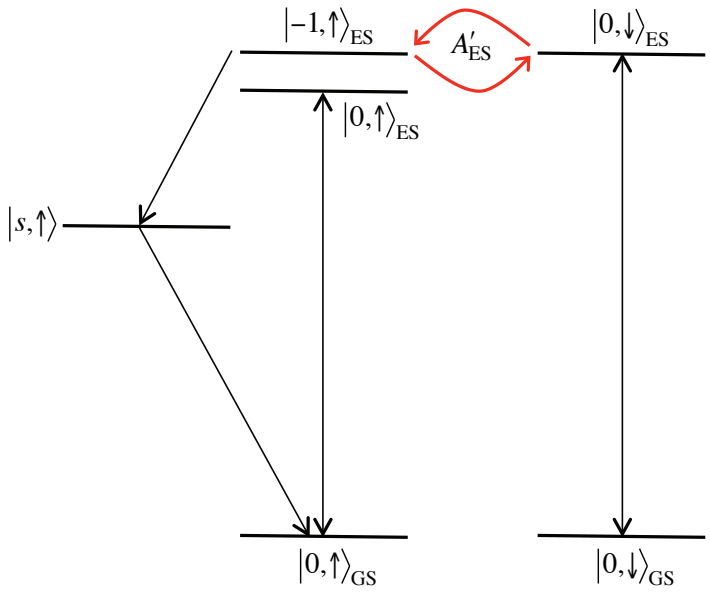

Figure 3.2: ^{15}N nuclear spin polarization mechanism near the level anticrossing $B \approx 500$ G under optical pumping. Only relevant states to the mechanism are depicted.

$|-1,\uparrow\rangle_{\mathrm{ES}}$ into two eigenstates

$$|+\rangle_{\mathrm{ES}} = \alpha\,|0,\downarrow\rangle_{\mathrm{ES}} + \beta\,|-1,\uparrow\rangle_{\mathrm{ES}}\,,$$
$$|-\rangle_{\mathrm{ES}} = -\beta\,|0,\downarrow\rangle_{\mathrm{ES}} + \alpha\,|-1,\uparrow\rangle_{\mathrm{ES}}\,,$$

with eigenenergies

$$\lambda_{\pm} = \frac{\delta_0 \pm \sqrt{\delta_0^2 + 2A_{\mathrm{ES}}'^2}}{2},$$

respectively, where α and β are given by

$$\alpha = \frac{A_{\mathrm{ES}}'/\sqrt{2}}{\sqrt{\lambda_+^2 + A_{\mathrm{ES}}'^2/2}},$$
$$\beta = \frac{\lambda_+}{\sqrt{\lambda_+^2 + A_{\mathrm{ES}}'^2/2}}.$$

Correspondingly, the level crossing at B_{LAC} becomes a level anti-crossing. Far from the anti-crossing point ($|\delta_0(B)| \gg A_{\mathrm{ES}}'$), the mixing is negligible $|+\rangle_{\mathrm{ES}} \approx |-1,\uparrow\rangle_{\mathrm{ES}}$ and $|-\rangle_{\mathrm{ES}} \approx |0,\downarrow\rangle_{\mathrm{ES}}$. Near the anti-crossing point ($|\delta_0(B)| \ll A_{\mathrm{ES}}'$), the $|0,\downarrow\rangle_{\mathrm{ES}}$ and $|-1,\uparrow\rangle_{\mathrm{ES}}$ states are equally mixed into the new eigenstates $|\pm\rangle_{\mathrm{ES}} \approx (\pm\,|0,\downarrow\rangle_{\mathrm{ES}} + |-1,\uparrow\rangle_{\mathrm{ES}})/\sqrt{2}$. At this point, the optical pumping excites the electron spin from $|0,\downarrow\rangle_{\mathrm{GS}}$ to $|0,\downarrow\rangle_{\mathrm{ES}} = (|+\rangle_{\mathrm{ES}} - |-\rangle_{\mathrm{ES}})/\sqrt{2}$, followed by the Rabi oscillation between $|0,\downarrow\rangle_{\mathrm{ES}}$ and $|-1,\uparrow\rangle_{\mathrm{ES}}$ induced by the hyperfine interaction $\hat{H}_{\perp}$. During the Rabi oscillation, the electron spin may go from $|-1,\uparrow\rangle_{\mathrm{ES}}$ to $|0,\uparrow\rangle_{\mathrm{GS}}$ through the intersystem crossing process (Fig. 3.2). Thus optical pumping transfers the population from $|0,\downarrow\rangle_{\mathrm{GS}}$ to $|0,\uparrow\rangle_{\mathrm{GS}}$. Similarly, optical pumping also transfers the population from $|\pm1\rangle_{\mathrm{GS}}$ into $|0\rangle_{\mathrm{GS}}$. Therefore, optical pumping of the electron spin can polarize both the electron spin and the ^{15}N nuclear spin at the same time. The complete picture of dynamic polarization of both the electron spin and the ^{15}N nuclear spin is illustrated in Fig. 3.3.

The dynamic polarization of the ^{15}N nuclear spin is sensitive to the magnetic field alignment [38]. If the magnetic field alignment deviates from the N-V axis by θ, near the excite-state level anticrossing, all the four states are mixed. Even for a small angle θ (*e.g.* $\theta = 1^{\circ}$), the strength $g_e\mu_B B\sin\theta \sim 24$ MHz of the mixing Hamiltonian by the magnetic field misalignment would be comparable to A_{ES}'. This mixing Hamiltonian induces the precession $|0,\uparrow\rangle_{\mathrm{ES}} \leftrightarrow |-1,\uparrow\rangle_{\mathrm{ES}}$ which, together with the optical pumping $|0,\uparrow\rangle_{\mathrm{GS}} \rightarrow$

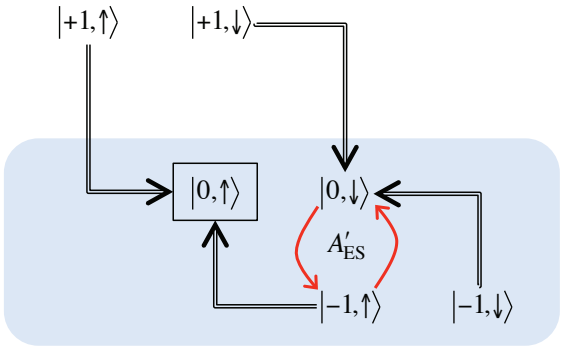

Figure 3.3: Polarization mechanism of the electron spin and the ^{15}N nuclear spin in the NV center. Black arrows represent the polarization of the electron spin by the intersystem crossing decay. Red arrows denote the precession between $|0,\downarrow\rangle$ and $|-1,\uparrow\rangle$ in the excited state due to the hyperfine interaction. The spins are polarized in $|0,\uparrow\rangle$ near the level anticrossing.

$|0,\uparrow\rangle_{ES}$, transfers the population back from $|0,\uparrow\rangle_{GS}$ to $|-1,\uparrow\rangle_{ES}$. This process competes with the the dynamic nuclear polarization process $|-1,\uparrow\rangle_{ES} \rightarrow |s,\uparrow\rangle \rightarrow |0,\uparrow\rangle_{GS}$ and hence partially depolarizes the ^{15}N nuclear spin.

In reference [38], Jacques *et. al.* measured the polarization of the ^{15}N nuclear spin after optical pumping of duration of several μs and found finite polarization over a broad range of the external magnetic field strength. They attribute the experimental data to the steady-state nuclear spin polarization determined by the competition between the dynamic nuclear spin polarization and the nuclear spin depolarization. To fit the data, they use a nuclear spin depolarization time $\sim$ 10 μs that is two orders of magnitude shorter than the reported value (longer than 1 ms under optical pumping [49]). A solution to this discrepancy is desirable.

3.2 Numerical calculation: Lindblad equations

In this section, we provide the numerical result for the nuclear spin polarization by optical pumping. We use the Lindblad equation ($\hbar = 1$)

$$\frac{d\hat{\rho}}{dt} = -i[\hat{H},\hat{\rho}] + \sum_{jk} \Gamma_{jk} \left(\hat{L}_{jk}\rho\hat{L}_{jk}^{\dagger} - \frac{\rho\hat{L}_{jk}^{\dagger}\hat{L}_{jk} + \hat{L}_{jk}^{\dagger}\hat{L}_{jk}\rho}{2} \right), \tag{3.2}$$

where $\hat{L}_{jk} \equiv |j\rangle\langle k|$ is the transition operator from $|k\rangle$ to $|j\rangle$ with the transition rate Γ_{jk}. Recent studies provide the decay rates of the electron spin in the NV center at room temperature: the optical decay rate $\gamma_0 = 0.0563\ \text{ns}^{-1}$ from the ES to the GS, the intersystem crossing decay rate $\gamma_1 = 0.0555\ \text{ns}^{-1}$ from $|\pm 1\rangle_{\text{ES}}$ to the intermediate singlet state $|s\rangle$, and the decay rate $\gamma_s = 0.0046\ \text{ns}^{-1}$ from the singlet state to $|0\rangle_{\text{GS}}$ [2, 28]. (See Fig. 3.6.) The dephasing rate of the ES is $\gamma_2^* = 0.092\ \text{ns}^{-1}$ [28]. We use $W = 10\gamma_0$ as the optical pumping rate. The coherent dynamics within the GS and the ES is governed by the corresponding Hamiltonian

$$\hat{H}_{\text{GS}} = D_{\text{GS}}\hat{S}_z^2 + g_e\mu_B B\hat{S}_z + A_{\text{GS}}\vec{S}\cdot\vec{I}, \tag{3.3}$$

and $\hat{H}_{\text{ES}}$ in Eq. (3.1), respectively. Here $D_{\text{GS}} = 2.87$ GHz is a zero-field splitting of the GS. The electron g-factor of the GS is the same as the ES ($g_e = 2.01$) [26]. We assume

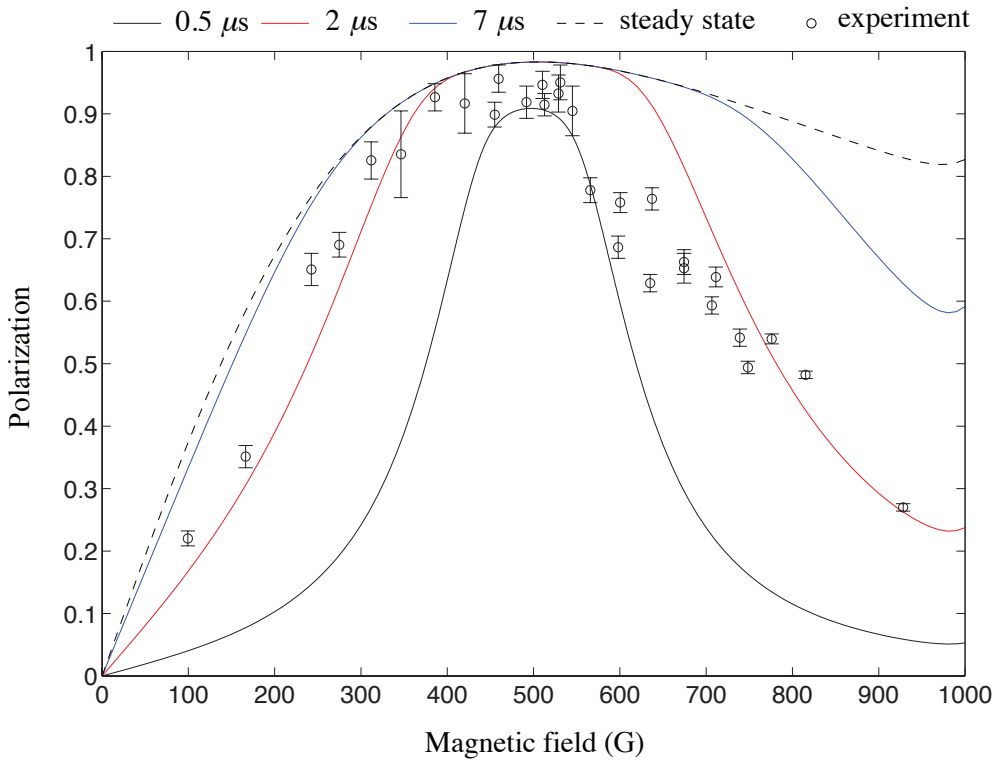

Figure 3.4: Polarization of the ^{15}N nuclear spin in the NV center after optical pumping as a function of the magnitude of the magnetic field with different durations of pumping time. The circles with the error bars denote the experimental data in [38] with permission. The pumping rate is $W = 10\gamma_0$.

that the initial state of the electron and the nuclear spins is unpolarized. After a finite duration of pumping, 2 μs of waiting time is included in the calculation to ensure that the electron spin is relaxed to the GS. We define the polarization of the ^{15}N nuclear spin as

$$P \equiv \frac{p'_{|0,\uparrow\rangle_{\mathrm{GS}}} - p'_{|0,\downarrow\rangle_{\mathrm{GS}}}}{p'_{|0,\uparrow\rangle_{\mathrm{GS}}} + p'_{|0,\downarrow\rangle_{\mathrm{GS}}}}, \tag{3.4}$$

where p'_j is a population of j-state at 2 μs after pumping. This definition is in accordance with the definition of the polarization in [38].

Fig. 3.4 depicts the polarization of the ^{15}N nuclear spin after optical pumping as a function of the magnetic field strength with various pumping times. The polarization of the nuclear spin is saturated within a few μs near the level anticrossing $B \approx 500$ G, while it takes longer time for the nuclear spin to reach the steady state away from the level anti-crossing point. We find that using the 2 μs pumping time as used in the experiment [38] gives the best fit to the experimental data. Therefore, the experimental observation in Ref. [38] may be the transient nuclear spin polarization after a finite pumping time

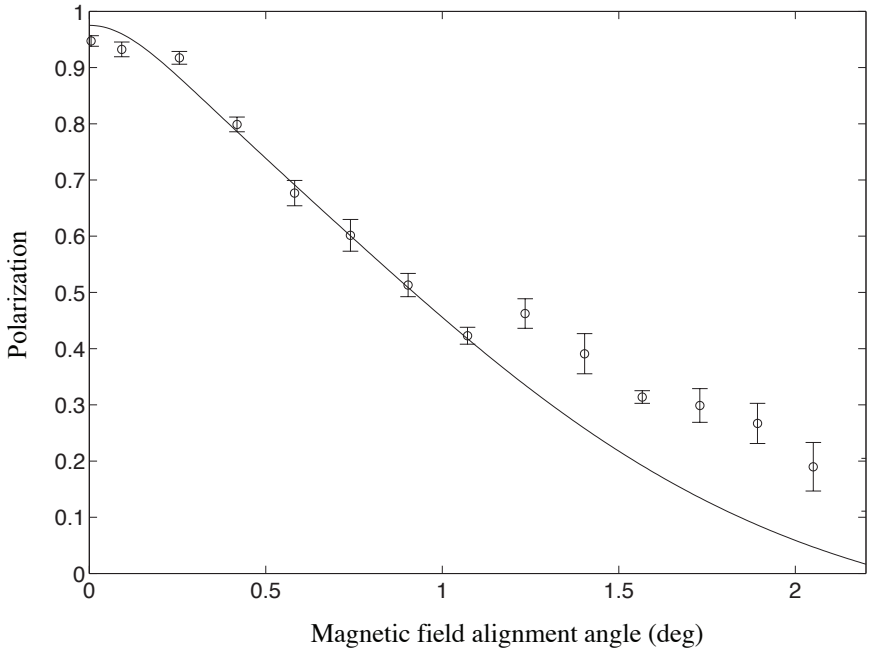

Figure 3.5: Polarization of the ^{15}N nuclear spin as a function of the magnetic field alignment angle with its magnitude $B = 472$ G. The circles with the error bars denote the experimental data in [38] with permission. The pumping rate is $W = 10\gamma_0$.

instead of the steady-state nuclear spin polarization. This provides a possible solution to the discrepancy between the nuclear spin depolarization time $\sim$ 10 μs as used in the theoretical fitting [38] and the reported nuclear spin depolarization time $\gtrsim$ 1 ms [49]. With a longer pumping time, a significant amount of polarization can be achieved even if the magnetic field is far away from the anticrossing point where the transition probability between $|0,\downarrow\rangle_{\mathrm{ES}}$ and $|-1,\uparrow\rangle_{\mathrm{ES}}$ is small.

The validity of the Lindblad equations approach is further confirmed by the magnetic field angle dependence of the ^{15}N nuclear spin polarization, which has not been calculated before. The calculation result of the Lindblad equations with 2 μs pumping time at B = 472 G well describes the experimental result in [38] (Fig.3.5).

3.3 Rate equations

The optical pumping used in polarizing the ^{15}N nuclear spin is incoherent. The initial state of the electron and the nuclear spin is also an incoherent mixture with no off-diagonal elements. Thus the rate equations approach can capture the essential physics in the Lindblad equations. In this approach, the Rabi oscillations between $|-1,\uparrow\rangle_{\mathrm{ES}}$ and $|0,\downarrow\rangle_{\mathrm{ES}}$ due to the hyperfine interaction is treated as spin-flip transitions with rates $\Gamma_{\pm}$ (Fig. 3.6). The rate equations are given by

$$
\begin{aligned}
\dot{p}_{|+1,\uparrow\rangle_{\mathrm{ES}}} &= -(\gamma_0+\gamma_1)p_{|+1,\uparrow\rangle_{\mathrm{ES}}} + Wp_{|+1,\uparrow\rangle_{\mathrm{GS}}} \\
\dot{p}_{|+1,\downarrow\rangle_{\mathrm{ES}}} &= -(\gamma_0+\gamma_1+\Gamma_+)p_{|+1,\downarrow\rangle_{\mathrm{ES}}} + \Gamma_+ p_{|0,\uparrow\rangle_{\mathrm{ES}}} + Wp_{|+1,\downarrow\rangle_{\mathrm{GS}}} \\
\dot{p}_{|0,\uparrow\rangle_{\mathrm{ES}}} &= \Gamma_+ p_{|+1,\downarrow\rangle_{\mathrm{ES}}} - (\gamma_0+\Gamma_+)p_{|0,\uparrow\rangle_{\mathrm{ES}}} + Wp_{|0,\uparrow\rangle_{\mathrm{GS}}} \\
\dot{p}_{|0,\downarrow\rangle_{\mathrm{ES}}} &= -(\gamma_0+\Gamma_-)p_{|0,\downarrow\rangle_{\mathrm{ES}}} + \Gamma_- p_{|-1,\uparrow\rangle_{\mathrm{ES}}} + Wp_{|0,\downarrow\rangle_{\mathrm{GS}}} \\
\dot{p}_{|-1,\uparrow\rangle_{\mathrm{ES}}} &= \Gamma_- p_{|0,\downarrow\rangle_{\mathrm{ES}}} - (\gamma_0+\gamma_1+\Gamma_-)p_{|-1,\uparrow\rangle_{\mathrm{ES}}} + Wp_{|-1,\uparrow\rangle_{\mathrm{GS}}} \\
\dot{p}_{|-1,\downarrow\rangle_{\mathrm{ES}}} &= -(\gamma_0+\gamma_1)p_{|-1,\downarrow\rangle_{\mathrm{ES}}} + Wp_{|-1,\downarrow\rangle_{\mathrm{GS}}} \\
\dot{p}_{|+1,\uparrow\rangle_{\mathrm{GS}}} &= \gamma_0 p_{|+1,\uparrow\rangle_{\mathrm{ES}}} - Wp_{|+1,\uparrow\rangle_{\mathrm{GS}}} \\
\dot{p}_{|+1,\downarrow\rangle_{\mathrm{GS}}} &= \gamma_0 p_{|+1,\downarrow\rangle_{\mathrm{ES}}} - Wp_{|+1,\downarrow\rangle_{\mathrm{GS}}}
\end{aligned}
$$

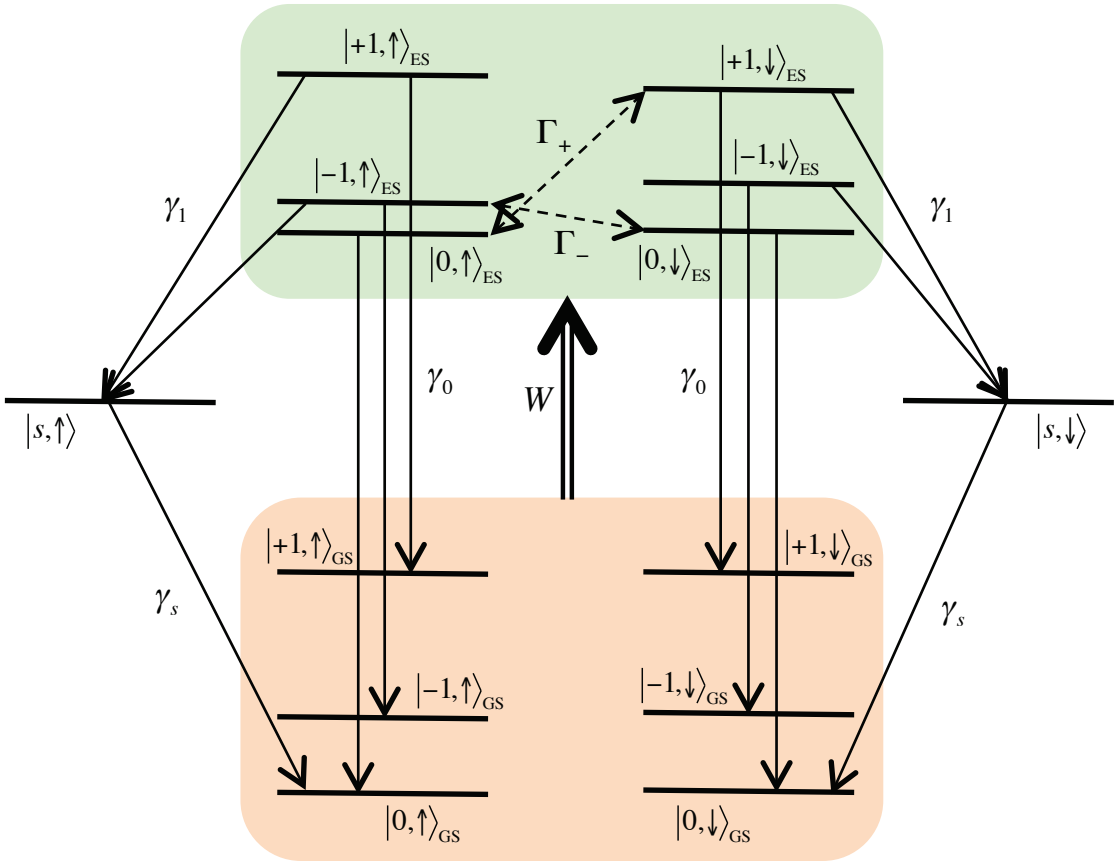

Figure 3.6: A level diagram for the electronic ground state and excited state of ^{15}NV center in diamond. The solid arrows are the nuclear spin conserving transitions, and the dashed arrows are the nuclear spin-flip transitions through the hyperfine interaction. W is an spin-conserving incoherent optical pumping rate from the ground state to the excited state.

$$
\begin{aligned}
\dot{p}_{|0,\uparrow\rangle_{\mathrm{GS}}} &= \gamma_0 p_{|0,\uparrow\rangle_{\mathrm{ES}}} - W p_{|0,\uparrow\rangle_{\mathrm{GS}}} + \gamma_s p_{|s,\uparrow\rangle} \\
\dot{p}_{|0,\downarrow\rangle_{\mathrm{GS}}} &= \gamma_0 p_{|0,\downarrow\rangle_{\mathrm{ES}}} - W p_{|0,\downarrow\rangle_{\mathrm{GS}}} + \gamma_s p_{|s,\downarrow\rangle} \\
\dot{p}_{|-1,\uparrow\rangle_{\mathrm{GS}}} &= \gamma_0 p_{|-1,\uparrow\rangle_{\mathrm{ES}}} - W p_{|-1,\uparrow\rangle_{\mathrm{GS}}} \\
\dot{p}_{|-1,\downarrow\rangle_{\mathrm{GS}}} &= \gamma_0 p_{|-1,\downarrow\rangle_{\mathrm{ES}}} - W p_{|-1,\downarrow\rangle_{\mathrm{GS}}} \\
\dot{p}_{|s,\uparrow\rangle} &= \gamma_1 (p_{|+1,\uparrow\rangle_{\mathrm{ES}}} + p_{|-1,\uparrow\rangle_{\mathrm{ES}}}) - \gamma_s p_{|s,\uparrow\rangle} \\
\dot{p}_{|s,\downarrow\rangle} &= \gamma_1 (p_{|+1,\downarrow\rangle_{\mathrm{ES}}} + p_{|-1,\downarrow\rangle_{\mathrm{ES}}}) - \gamma_s p_{|s,\downarrow\rangle},
\end{aligned}
$$

where the spin-flip transition rates

$$
\Gamma_{\pm} = \frac{A'^2_{\mathrm{ES}} \gamma_2}{\gamma_2^2 + (D_{es} \pm g_e \mu_B B - A_{\mathrm{ES}}/2)^2} \tag{3.5}
$$

are obtained from the Fermi's golden rule. γ_2 is the electron spin dephasing rate in the ES and it is given by $\gamma_2 = (\gamma_0 + 2\gamma_1)/2 + \gamma_2^* = 0.17\ \mathrm{ns}^{-1}$. We use $W = 10\gamma_0$ as the optical pumping rate. The hyperfine interaction in the GS is not included in the rate equations.

We first compare the numerical solution to the rate equations with that to the Lindblad equations. The initial electron-nuclear spin state is unpolarized, and 2 μs waiting time is included after optical pumping. Figure 3.7 depicts the nuclear spin polarization as a function of the magnetic field strength. The near complete coincidence of the rate equation result with the result of the Lindblad equations implies that the rate equation approach is sufficient to understand the dynamics of the nuclear spin polarization under optical pumping.

From the structure of the rate equations, we see that the nuclear spin polarization mechanism can be understood as a competition between Γ_+ and Γ_-. All the other transitions are nuclear spin-conserving. This is why a large amount of nuclear spin polarization is achieved not only near the anticrossing where Γ_- has a Lorentzian peak but also far away from the anticrossing where $\Gamma_- \gg \Gamma_+$ (*e.g.* $B \approx 800$ G). The time needed for the steady state to be established is determined by the slowest transition in the mechanism. Near the anticrossing, γ_s is the slowest transition and the characteristic time of the mechanism is $\sim 1/\gamma_s = 0.22$ μs. Thus 2 μs pumping time is enough to saturate the nuclear spin polarization. However, Γ_- becomes the slowest transition when the magnetic field is far from the anticrossing. At $B = 800$ G, for example, the corresponding characteristic time of the mechanism is $\sim 1/\Gamma_- \approx 1$ μs and longer than 2 μs of pumping

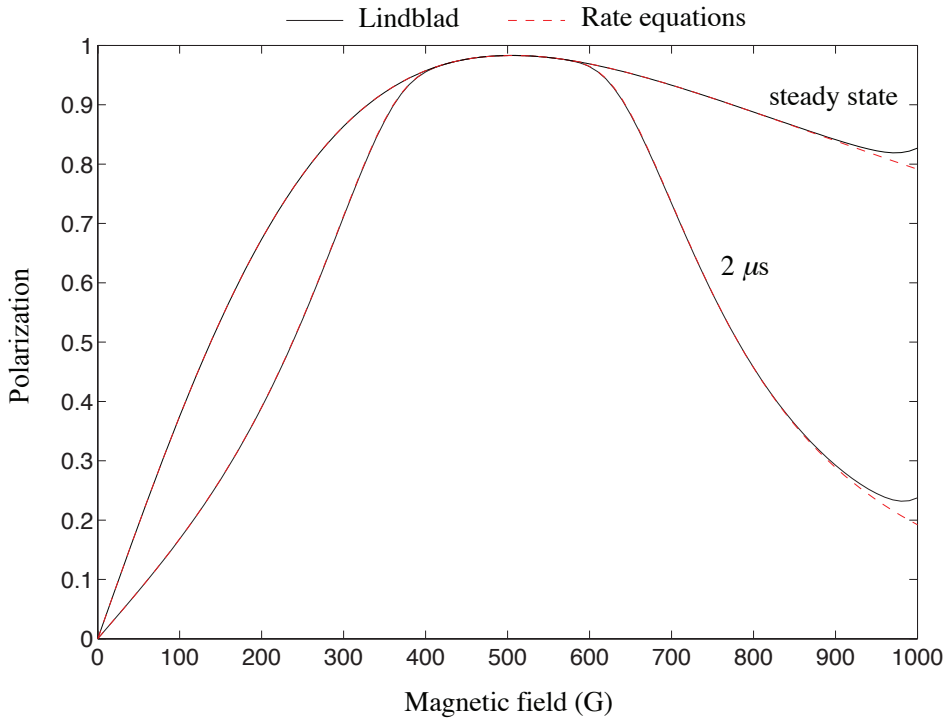

Figure 3.7: Comparison between the solutions of the Lindblad equations and the solutions of the rate equations with 2 μs of pumping time and at the steady state. The pumping rate is $W = 10\gamma_0$.

is necessary to establish the steady state.

An analytic expression for the ^{15}N nuclear spin polarization at the steady state is available from the rate equations. The population of each state does not change any more at the steady state, i.e., $\dot{p}_j = 0$ for all states. Once the pumping is turned off, the electron spin in the ES decays to the GS. In particular, the electron spin in $|\pm 1\rangle_{\mathrm{ES}}$ experiences either the spin-conserving optical decay or the intersystem crossing decay through the single state with a 50% probability since $\gamma_0 \approx \gamma_1$. Thus the final population of $|0, \uparrow (\downarrow)\rangle_{\mathrm{GS}}$ can be written as

$$p'_{|0,\uparrow(\downarrow)\rangle_{\mathrm{GS}}} = p_{|0,\uparrow(\downarrow)\rangle_{\mathrm{ES}}} + p_{|0,\uparrow(\downarrow)\rangle_{\mathrm{GS}}} + p_{|s,\uparrow(\downarrow)\rangle} + \frac{p_{|+1,\uparrow(\downarrow)\rangle_{\mathrm{ES}}}}{2} + \frac{p_{|-1,\uparrow(\downarrow)\rangle_{\mathrm{ES}}}}{2}. \tag{3.6}$$

We take $p_{|+1,\uparrow\rangle_{\mathrm{ES}}} = p_{|-1,\downarrow\rangle_{\mathrm{ES}}} = 0$ because these states do not participate in the polarization mechanism and their population rapidly goes to zero by the intersystem crossing decay under optical pumping. In addition, it is easy to show from the rate equations that $p_{|+1,\downarrow\rangle_{\mathrm{ES}}} = p_{|-1,\uparrow\rangle_{\mathrm{ES}}}$ and $p_{|s,\uparrow\rangle} = p_{|s,\downarrow\rangle}$ at the steady state. Then the steady-state nuclear spin

polarization in Eq. (3.4) is given by

$$P = \frac{1 - R_+/R_-}{1 + R_+/R_- + R_+C}, \tag{3.7}$$

where $R_\pm \equiv \Gamma_\pm/(\Gamma_\pm + \gamma_1)$ are normalized spin flip transition rates and $C \equiv (1 + 2\gamma_1/\gamma_2 + 2\gamma_1/W)/(1 + \gamma_0/W)$ is a constant defined by the relaxation rates of the electron spin and the pumping rate. From Eq. (3.7), it is confirmed that the steady-state nuclear spin polarization is a result of the competition between R_+ and R_- (equivalent to Γ_+ and Γ_-). Moreover, from the expression of C, we expect that a larger steady-state polarization may be achieved when the pumping rate W is weaker. This point will be discussed in the next section.

3.4 Effect of strain to ^{15}N nuclear spin polarization

The electron spin in the ES is affected by a local strain due to the orbital doublet of the ES. In the presence of the local strain at room temperature, the ES Hamiltonian in Eq. (3.1) becomes

$$\begin{aligned}\hat{H}_{\rm ES} &= D_{\rm ES}\hat{S}_z^2 + g_e\mu_B\vec{B}\vec{S} + A_{\rm ES}\hat{S}_z\hat{I}_z + A'_{\rm ES}\frac{\hat{S}_+\hat{I}_- + \hat{S}_-\hat{I}_+}{2} + E_{\rm ES}(\hat{S}_x^2 - \hat{S}_y^2) \\ &= \hat{H}_0 + \hat{H}_\perp + \hat{H}_{\rm str},\end{aligned} \tag{3.8}$$

where $E_{\rm ES}$ is the magnitude of anisotropy induced by the transverse strain [5, 26]. The typical value of $E_{\rm ES}$ is $\sim 50 - 100$ MHz [26]. From the Lindblad equations with $\hat{H}_{\rm ES}$ in Eq. (3.8), we can calculate the ^{15}N nuclear spin polarization at the steady state under the local transverse strain (black solid line in Fig. 3.8). We can see that the polarization has a dip near the ES level anticrossing. Therefore, maximal ^{15}N nuclear spin polarization is achieved slightly away from the level anti-crossing point.

We use the rate equations approach to understand the dip near the level anti-crossing in the presence of the local transverse strain. It is clear from $\hat{S}_x^2 - \hat{S}_y^2 = |+1\rangle\langle -1| + |-1\rangle\langle +1|$ that the transverse strain causes the mixing between $|+1\rangle_{\rm ES}$ and $|1\rangle_{\rm ES}$. Near the excite-state level anticrossing, we are allowed to treat the strain as a

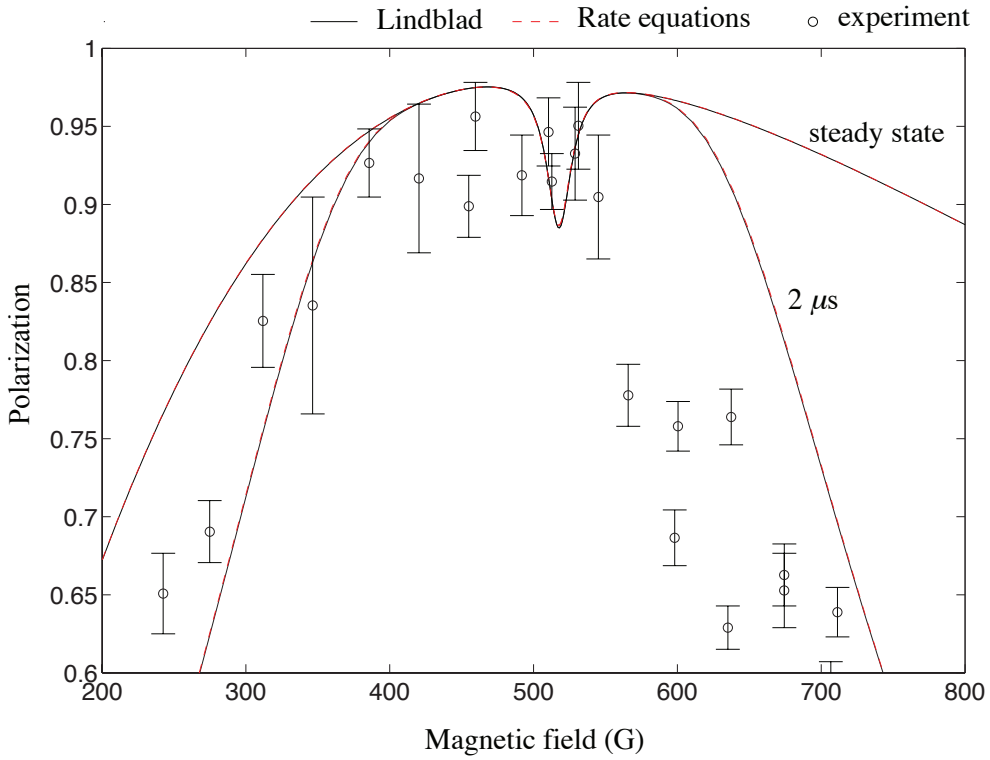

Figure 3.8: Polarization of the ^{15}N nuclear spin after 2 μs of pumping and at the steady state. The circles with the error bars denote the experimental data in [38] with permission. The pumping rate is $W = 10\gamma_0$.

perturbation to H_0 because $E_{\rm ES} \ll 2D_{\rm ES}$ [26]. Then the eigenstates of $\hat{H}_0 + \hat{H}_{\rm str}$ are

$$
\begin{aligned}
|\widetilde{+1,\uparrow}\rangle_{\rm ES} &= \left(1-\eta_\uparrow^2/2\right)|+1,\uparrow\rangle_{\rm ES} + \eta_\uparrow |-1,\uparrow\rangle_{\rm ES} \\
|\widetilde{-1,\uparrow}\rangle_{\rm ES} &= -\eta_\uparrow |+1,\uparrow\rangle_{\rm ES} + \left(1-\eta_\uparrow^2/2\right)|-1,\uparrow\rangle_{\rm ES} \\
|\widetilde{+1,\downarrow}\rangle_{\rm ES} &= \left(1-\eta_\downarrow^2/2\right)|+1,\downarrow\rangle_{\rm ES} + \eta_\downarrow |-1,\downarrow\rangle_{\rm ES} \\
|\widetilde{-1,\downarrow}\rangle_{\rm ES} &= -\eta_\downarrow |+1,\downarrow\rangle_{\rm ES} + \left(1-\eta_\downarrow^2/2\right)|-1,\downarrow\rangle_{\rm ES}
\end{aligned}
$$

with the eigenvalues

$$
\begin{aligned}
\epsilon_{+1,\uparrow} &= D_{\rm ES} + g_e\mu_B B + A_{\rm ES}/2 + \eta_\uparrow E_{\rm ES} \\
\epsilon_{-1,\uparrow} &= D_{\rm ES} - g_e\mu_B B - A_{\rm ES}/2 - \eta_\uparrow E_{\rm ES} \\
\epsilon_{+1,\downarrow} &= D_{\rm ES} + g_e\mu_B B - A_{\rm ES}/2 + \eta_\downarrow E_{\rm ES} \\
\epsilon_{-1,\downarrow} &= D_{\rm ES} - g_e\mu_B B + A_{\rm ES}/2 - \eta_\downarrow E_{\rm ES},
\end{aligned}
$$

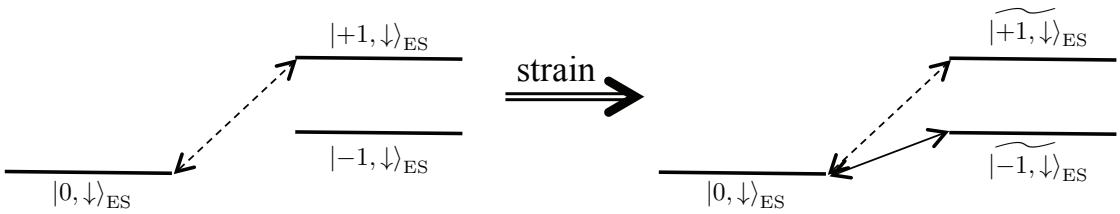

Figure 3.9: Origin of the dip in the ^{15}N nuclear spin polarization graph. In the presence of the local strain, the transition $|0,\downarrow\rangle_{\rm ES} \leftrightarrow \widetilde{|-1,\downarrow\rangle}_{\rm ES}$ is active and Γ_+ has a Lorentzian peak near the level anticrossing.

where $\eta_{\uparrow(\downarrow)} \equiv E_{\rm ES}/(2g_e\mu_B B \pm A_{\rm ES})$ is the strength of the perturbation.

Now we consider how the hyperfine interaction induced spin-flip transition rates $\Gamma_\pm$ change under the local strain. Note that both $\widetilde{|+1,\downarrow\rangle}_{\rm ES}$ and $\widetilde{|-1,\downarrow\rangle}_{\rm ES}$ contain $|+1,\downarrow\rangle_{\rm ES}$. This implies the transition $|0,\uparrow\rangle_{\rm ES} \leftrightarrow \widetilde{|-1,\downarrow\rangle}_{\rm ES}$ is also allowed in addition to the transition $|0,\uparrow\rangle_{\rm ES} \leftrightarrow \widetilde{|+1,\downarrow\rangle}_{\rm ES}$ (Fig. 3.9). Then Γ_+ can be written as

$$\Gamma_+ = \left(1-\eta_\downarrow^2\right)\frac{A_{\rm ES}'^2\gamma_2}{\gamma_2^2+\epsilon_{+1,\downarrow}^2} + \eta_\downarrow^2\frac{A_{\rm ES}'^2\gamma_2}{\gamma_2^2+\epsilon_{-1,\downarrow}^2}. \tag{3.9}$$

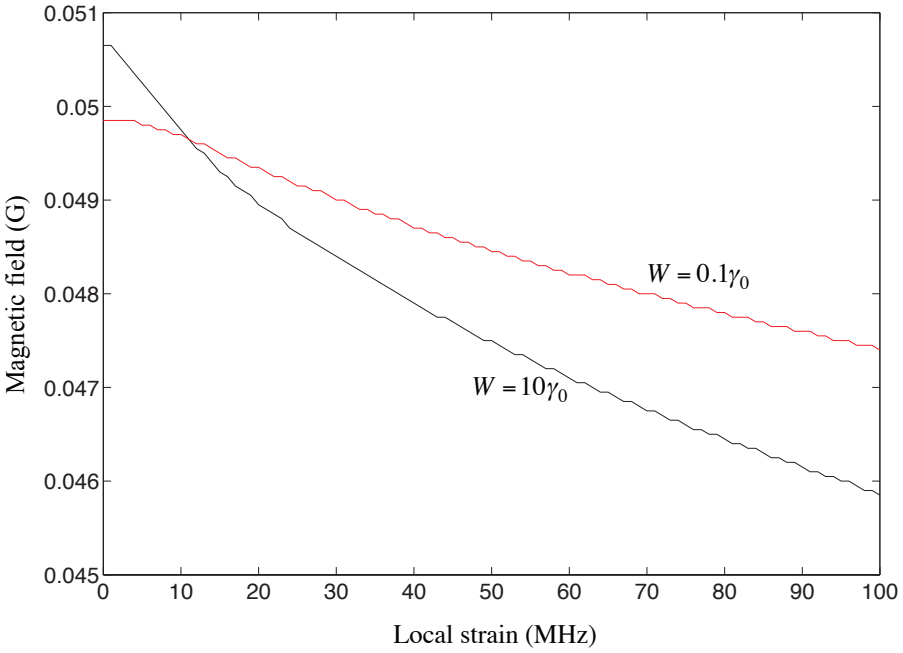

Figure 3.10: Optimal magnetic field magnitude which produces the maximum steady-state nuclear spin polarization as a function of the local strain.

Γ_+ has a Lorentzian peak at $B'_{\mathrm{LAC}} \approx 520$ G because $|\widetilde{-1,\downarrow}\rangle_{\mathrm{ES}}$ forms another anticrossing with $|0,\uparrow\rangle_{\mathrm{ES}}$ at B'_{LAC}. As a result, Γ_+ may not be negligible near B'_{LAC} in the presence of the strain while it is negligible in the absence of the strain. Γ_- is also modified by the strain to

$$\Gamma_- = \eta_\uparrow^2 \frac{A'^2_{\mathrm{ES}}\gamma_2}{\gamma_2^2 + \epsilon_{+1,\uparrow}^2} + \left(1 - \eta_\uparrow^2\right) \frac{A'^2_{\mathrm{ES}}\gamma_2}{\gamma_2^2 + \epsilon_{-1,\uparrow}^2}. \tag{3.10}$$

Fig. 3.8 (red dashed line) depicts the steady-state nuclear spin polarization obtained by plugging $\Gamma_\pm$ into Eq. (3.7). The agreement of the rate equation results with the results from the Lindblad equation proves that the transition $|0,\uparrow\rangle_{\mathrm{ES}} \leftrightarrow |\widetilde{+1,\downarrow}\rangle_{\mathrm{ES}}$ is indeed the origin of the dip near the level anticrossing.

The optimal point to achieve the largest polarization may be computable by taking the derivative of Eq. (3.7) with respect to B, but it is a tedious process. Instead we provide a numerical result for the optimal choice of magnetic field magnitude as a function of the transverse strain in Fig. 3.10. For a typical value of the local strain $E_{\mathrm{ES}} \sim 50 - 100$ MHz, the maximum polarization is achieved at $B \sim 470 - 480$ G both

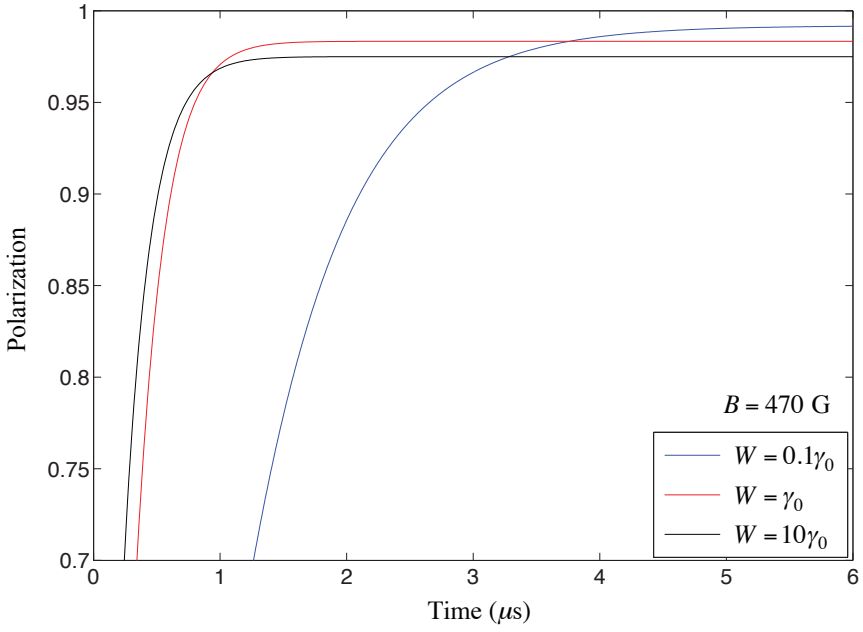

Figure 3.11: Polarization of the ^{15}N nuclear spin polarization at $B = 470$ G as a function of the duration of optical pumping. The polarization is calculated from the Lindblad equations with $E_{\mathrm{ES}} = 70$ MHz.

with a weak pumping rate ($W = 0.1\gamma_0$) and with a strong pumping rate ($W = 10\gamma_0$).

As mentioned in Sec. 3.3, a larger steady-state polarization can be obtained when the pumping rate W is weaker. We calculate the dynamics of the nuclear spin polarization at $B = 470$ G by solving the Lindblad equations with different pumping rates (Fig. 3.11). The x-axis denotes the duration of optical pumping. As expected, a weaker pumping rate produces a larger nuclear spin polarization in compensation for a longer pumping time.

In summary, in the presence of the local strain in the NV center, the maximum nuclear spin polarization occurs not at the level anticrossing ($B \approx 500$) G of the ES but near $B \sim 470$ G with a pumping rate weaker than γ_0.

3.5 Initialization of ^{14}N nuclear spin

Most nitrogen atom in nature is ^{14}N ($I = 1$) with the natural abundance of 99.6%. Since the nitrogen nuclear spin is intrinsic to the NV center, it is beneficial to make use of the nitrogen nuclear spin for quantum computation in addition to the electron spin. Several studies have been reported about the applications of the ^{14}NV system [25, 61, 62]. In these studies, the nuclear spin initialization has been done at the ES level anticrossing. However, because of the local strain, tuning the magnetic field magnitude at the anticrossing to initialize the ^{14}N nuclear spin may not be the most productive. In this section, we use the Lindblad equations to see the effect of the local strain to the initialization of the ^{14}N nuclear spin.

The GS and the ES Hamiltonians of the ^{14}NV center are given by

$$\hat{H}_{\mathrm{GS}} = D_{\mathrm{GS}}\hat{S}_z^2 + g_e\mu_B B\hat{S}_z + A_{\mathrm{GS}}\vec{S}\cdot\vec{I} + QI_z^2, \tag{3.11a}$$

$$\hat{H}_{\mathrm{ES}} = D_{\mathrm{ES}}\hat{S}_z^2 + g_e\mu_B B\hat{S}_z + A_{\mathrm{ES}}\vec{S}\cdot\vec{I} + QI_z^2 + E_{\mathrm{ES}}(S_x^2 - S_y^2), \tag{3.11b}$$

where $Q = -5.0$ MHz is the quadrupole interaction of the nitrogen. The hyperfine interactions of the ^{14}N nuclear spin are $A_{\mathrm{GS}} = -2.2$ MHz and $A_{\mathrm{ES}} = 50$ MHz [23, 61]. We assume that the ES hyperfine interaction for ^{14}N is isotropic. We use $|m_s, m_I\rangle$ as a basis of the ^{14}NV system.

The initialization mechanism of ^{14}N nuclear spin is the same with the mechanism of the ^{15}N nuclear spin. $|0, m_I\rangle_{\mathrm{ES}}$ and $|-1, m_I\rangle_{\mathrm{ES}}$ become degenerate near $B \approx 500$ G, and

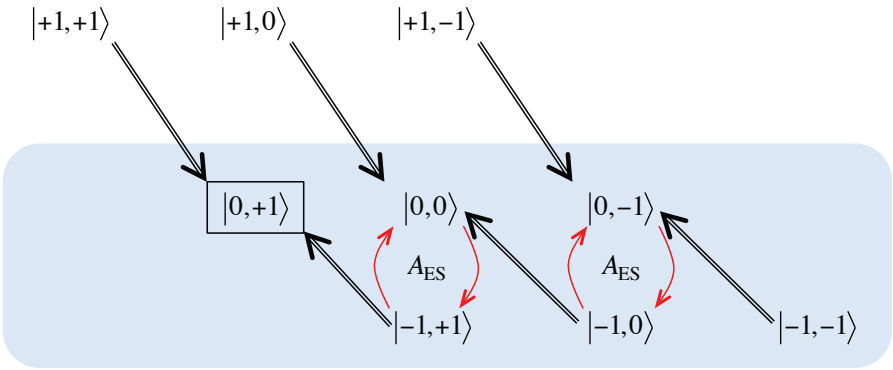

Figure 3.12: Initialization mechanism of the electron spin and the ^{14}N nuclear spin in the NV center. Black arrows represent the initialization of the electron spin by the intersystem crossing decay. Red arrows denote the precession due to the hyperfine interaction in the excited state. The spins are initialized in $|0,+1\rangle$ after optical pumping.

the spin-flip transitions $|0,0\rangle_{\mathrm{ES}} \leftrightarrow |-1,+1\rangle_{\mathrm{ES}}$ and $|0,-1\rangle_{\mathrm{ES}} \leftrightarrow |-1,0\rangle_{\mathrm{ES}}$ are resonantly active. Therefore, several cycles of optical pumping, spin-flip transitions by the hyperfine interaction, and the intersystem crossing decay initialize both the electron spin and ^{14}N nuclear spin in $|0,\uparrow\rangle_{\mathrm{GS}}$. The complete initialization diagram for both the electron spin and the ^{14}N nuclear spin is depicted in Fig 3.12.

In the presence of the local strain, however, $|+1,m_I\rangle_{\mathrm{ES}}$ and $|-1,m_I\rangle_{\mathrm{ES}}$ are weakly mixed near the anticrossing and form new eigenstates $|\widetilde{\pm 1,m_I}\rangle_{\mathrm{ES}}$. In particular, $|\widetilde{-1,0}\rangle_{\mathrm{ES}}$ has a small portion of $|+1,0\rangle_{\mathrm{ES}}$, and $|\widetilde{-1,-1}\rangle_{\mathrm{ES}}$ has a small portion of $|+1,-1\rangle_{\mathrm{ES}}$. Therefore, the transitions $|0,+1\rangle_{\mathrm{ES}} \leftrightarrow |\widetilde{-1,0}\rangle_{\mathrm{ES}}$ and $|0,0\rangle_{\mathrm{ES}} \leftrightarrow |\widetilde{-1,-1}\rangle_{\mathrm{ES}}$ depolarize the nuclear spin when the system is close to the level anticrossing.

We calculate $p'_{|0,+1\rangle_{\mathrm{GS}}}$, the steady-state population of $|0,+1\rangle_{\mathrm{GS}}$ after optical pumping by plugging the Hamiltonians (Eqs. (3.11)) into the Lindblad equations (Fig. 3.13). As expected, $p'_{|0,+1\rangle_{\mathrm{GS}}}$ has a dip near the level anticrossing in the presence of the local transverse strain. A larger steady-state population of ^{14}N nuclear spin can be achieve with a weaker pumping rate and a longer pumping time. The optimal magnetic field for the nuclear spin initialization is $B \sim 580$ G. At this magnetic field, up to 98% of the population is initialized in $|0,+1\rangle_{\mathrm{GS}}$ with $W = 0.1$. We expect that the effect of the local strain to the initialization mechanism can be confirmed by experiments [4, 26].

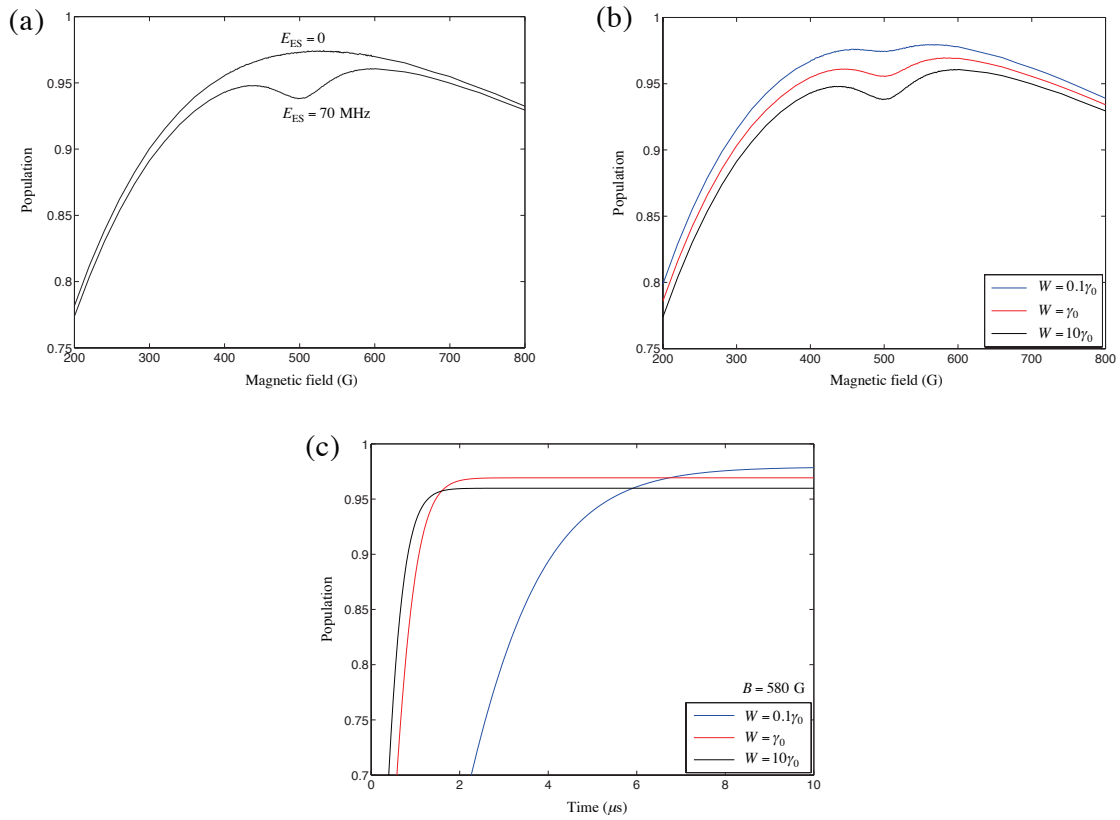

Figure 3.13: Steady-state population $p'_{|0,+1\rangle_{GS}}$ of the ^{14}NV center after optical pumping. (a) Population with and without the local strain. The pumping rate is $W = 10\gamma_0$. (b) Population with different pumping rates. The local strain is fixed at $E_{ES} = 70$ MHz. (c) Population as a function of time with different pumping times. The local strain is fixed at $E_{ES} = 70$ MHz.

3.6 Conclusions

We have studied the dynamic polarization of the nitrogen nuclear spin in the NV center under optical pumping [38] through the Lindblad equation approach and the rate equation approach. The results suggest that the experimentally observed nuclear spin polarization might be the transient value after a finite pumping time instead of the steady-state value [38]. This provides a possible solution to the discrepancy between the nuclear spin depolarization time ~ 10 μs as used in the theoretical fitting [38] and the reported nuclear spin depolarization time $\gtrsim 1$ ms [49] In the steady state, a large nuclear spin polarization can be achieved by a longer pumping even far from the level anticrossing. Our study also shows that the local strain of the NV center depolarizes the

nuclear spin near the anticrossing, so that the maximal nuclear spin polarization occurs slightly away from the anti-crossing point, in conrast to previous understanding that the maximal polarization occurs at the anti-crossing point. We expect that our study is useful to nitrogen nuclear-spin based quantum operations where a nearly pure nuclear spin is required at room temperature.

3.7 Acknowledgments

The text of chapter 2, in part, is a reprint of the material that is being prepared for publication as Bang, K.; Yang, W.; Sham, L. J. *Optical Initialization of Nitrogen Nuclear Spins in Nitrogen-Vacancy Center*. The co-authors in this publication directed, supervised, and co-worked on the research which forms the basis of this chapter.

Chapter 4

Quantum measurement of hyperfine interaction in nitrogen-vacancy center

The negatively charged nitrogen vacancy (NV) center is a candidate for the application of quantum parameter estimation (also known as quantum metrology). Quantum metrology seeks quantum measurement protocols to estimate physical parameters up to a given precision defined as $1/\Delta^2$ (with Δ being the standard deviation) using the least amount R of resources, which include the number of measurements, the total duration of the measurements, and the number of particles involved in the measurements. The classical protocol utilizes the number R of repeated measurements as a resource and, according to the central limit theorem, gives the classical limit (also known as standard quantum limit or SQL) $\Delta_{\mathrm{SQL}} = O(1/\sqrt{R})$. Quantum metrology aims to surpass the SQL and, more ambitiously, reach the quantum metrology limit (QML) $\Delta_{\mathrm{QML}} = O(1/R)$, the upper precision bound $1/\Delta^2_{\mathrm{QML}} = O(R^2)$ set by quantum mechanics. The most popular quantum measurement technique is interferometry, in which the parameter to be measured is recorded as a phase in the coherence of the system [20, 21, 32, 33]. The exceptionally long coherence time of the NV center electron spin diminishes the detrimental effect of decoherence on such measurements and makes the NV center an ideal system for quantum metrology [34]. Up to date, most of the measurement protocols utilize pure quantum states and surpass the SQL by creating quantum entanglement in the system. However, the thermal equilibrium state of the nuclear spins is highly mixed at room temperature. To estimate *reliably* the hyperfine interaction in the NV center by

a pure-state protocol, the nuclear spins must be prepared repeatedly into a given pure state. Further, the number of spins as the resources of entanglement in a single NV center is finite [51], so the advantage of quantum entanglement to parameter estimation is also limited.

Recently, Boixo and Somma [6] proposed a model of mixed-state quantum metrology by combining the mixed-state quantum computation (also known as deterministic quantum computation with one quantum bit [41] or DQC1) with the adaptive Bayesian inference. This DQC1 model utilizes the total duration T (instead of large-scale entanglement [34]) of the estimation process as a resource to approach the QML $\Delta_{\mathrm{QML}} = O(1/T)$ without creating any entanglement [14, 42]. However, its application to estimate the hyperfine interaction in the NV center requires including the effects of noise and unintended dynamics.

In this chapter, we construct an efficient quantum measurement protocol to estimate the hyperfine interaction between the electron spin and the ^{15}N nuclear spin in the NV center. This protocol is essentially a combination of the DQC1 model [6] and the spin-echo technique [68], which decouples the dynamics driven by the hyperfine interaction from the noise and unintended dynamics. It does not need the preparation of the nuclear spin state and approaches the QML $\Delta_{\mathrm{QML}} = O(1/T)$ in the ideal case. By including realistic errors (such as the nuclear spin rotation error and the electron spin decoherence) in our analysis, we show that our protocol still surpasses the SQL under typical experimental conditions.

4.1 Quantum metrology

As mentioned above, quantum metrology pursues efficient quantum methods to estimate a physical parameter beyond the SQL with a finite amount of resources. First, we introduce a conceptual framework of quantum metrology and show that quantum metrological methods can overcome the classical limit.

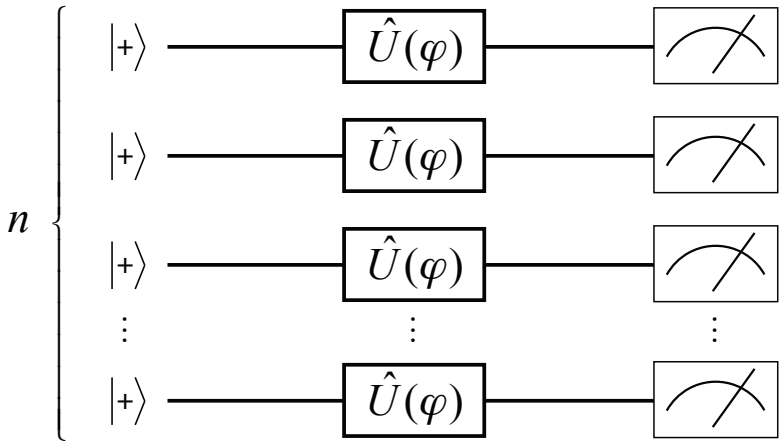

Figure 4.1: n independent qubits with the phase operation $\hat{U}(\varphi)$ and the detector.

4.1.1 Standard quantum limit

Suppose there are n identical qubits. Each qubit is separately prepared in $|+\rangle = (|0\rangle + |1\rangle) / \sqrt{2}$ (Fig. 4.1). They are independent and do interact with each other. We apply the identical phase operation to each qubit

$$\hat{U}(\varphi) = |0\rangle\langle 0| + e^{i\varphi} |1\rangle\langle 1| .$$

Then the total state of n qubits is the product of each qubit state

$$\rho_{\text{tot}} = \left[\frac{1}{2} \left(|0\rangle\langle 0| + e^{-i\varphi} |0\rangle\langle 1| + e^{i\varphi} |1\rangle\langle 0| + |1\rangle\langle 1| \right) \right]^{\otimes n} .$$

We also have n detectors attached to each qubit. Each detector measures the observable $\hat{X} = |0\rangle\langle 0| + |1\rangle\langle 1|$ of the qubit. If the measurements are made at the same time, the average value of $\hat{X}^{\otimes n}$ is given by

$$\langle \hat{X}^{\otimes n} \rangle = \text{Tr} \left[\rho_{\text{tot}} \hat{X}^{\otimes n} \right] = \cos^n \varphi. \tag{4.1}$$

The sequence of the qubit preparations, the phase operations, and the measurements are repeated N times to obtain $\langle \hat{X}^{\otimes n} \rangle$ with the standard deviation $\Delta(X^{\otimes n}) \sim 1/\sqrt{N}$. The $1/\sqrt{N}$ dependence comes from the central limit theorem.

φ is estimated from Eq. (4.1),

$$\varphi = \left[\cos^{-1} \left(\langle \hat{X}^{\otimes n} \rangle \right) \right]^{1/n} . \tag{4.2}$$

The standard deviation of the estimation of φ is given by

$$\Delta_\varphi = \frac{\Delta(X^{\otimes n})}{\left|\partial\langle\hat{X}^{\otimes n}\rangle/\partial\varphi\right|} \geq \frac{\Delta(X^{\otimes n})}{\sqrt{n}} \sim \frac{1}{\sqrt{nN}}. \tag{4.3}$$

Eq. (4.3) shows that Δ_φ decreases as $1/\sqrt{n}$. This result is obvious since the N measurements with n qubits are equivalent to the nN measurements with one qubit. Thus increasing the number of independent qubits decreases the standard deviation in the classical way. The limit $1/\sqrt{n}$ of the estimation is called the standard quantum limit (SQL) and denotes the lower bound of the standard deviation set by the classical mechanics. In quantum optics, $1/\sqrt{n}$ limitation is also called the shot-noise limit (SNL).

4.1.2 Entanglement and quantum metrology limit

Here we demonstrate that the estimation with entangled qubits can exceed the SQL. Suppose that the initial state of n qubits is maximally entangled state (Fig. 4.2)

$$|\Psi\rangle_{\text{tot},0} = \frac{1}{\sqrt{2}}\left[|0,0,\cdots,0\rangle + |1,1,\cdots,1\rangle\right].$$

After the phase operation $\hat{U}(\varphi)$ is applied to each qubit, the total state of n qubit is

$$|\Psi\rangle_{\text{tot}} = \frac{1}{\sqrt{2}}\left[|0,0,\cdots,0\rangle + e^{in\varphi}\,|1,1,\cdots,1\rangle\right].$$

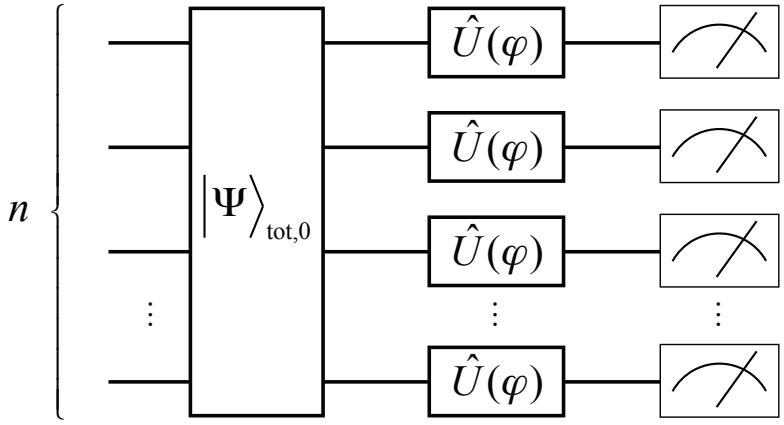

Figure 4.2: n maximally entangled qubits with the phase operation $\hat{U}(\varphi)$ and the detector.

By measuring $\hat{X}$ of each qubit N times, we can obtain $\langle \hat{X}^{\otimes n} \rangle$ which is given by

$$\langle \hat{X}^{\otimes n} \rangle = \mathrm{Tr}\left[|\Psi\rangle \langle \Psi|_{\mathrm{tot}} \hat{X}^{\otimes n} \right] = \cos(n\varphi). \tag{4.4}$$

with the standard deviation $\Delta(\hat{X}^{\otimes n}) \sim 1/\sqrt{N}$. Then the estimated value of φ is

$$\varphi = \frac{1}{n} \cos^{-1}\left(\langle \hat{X}^{\otimes n} \rangle \right), \tag{4.5}$$

with the standard deviation

$$\Delta_\varphi = \frac{\Delta(X^{\otimes n})}{\left| \partial \langle \hat{X}^{\otimes n} \rangle / \partial \varphi \right|} \geq \frac{\Delta(X^{\otimes n})}{n} \sim \frac{1}{n\sqrt{N}}. \tag{4.6}$$

It is clear from Eq. (4.6) that the maximal entanglement further decreases the standard deviation of the estimation Δ_φ by $1/\sqrt{n}$ with compared to the SQL in Eq. (4.3). The estimation becomes more precise as more qubits are entangled. This is a pure quantum mechanical effect. In the entangled state, the effect of the phase operation $\hat{U}(\varphi)$ is accumulated in the total state while it is independent when the qubits are not correlated. The limit $1/n$ of the estimation is called the quantum metrology limit (QML) and denotes the lower bound of the standard deviation set by quantum mechanics. In quantum optics, $1/n$ limitation is also called the Heisenberg limit.

4.1.3 Multiround protocol

In a real experiment, it is not easy to create a large-scale entanglement. However, it is possible to surpass the SQL without entanglement. Instead of entanglement, such an estimation method uses a sequence of identical quantum operations. Here we introduce the multiround protocol proposed by Giovannetti *et. al.* [33].

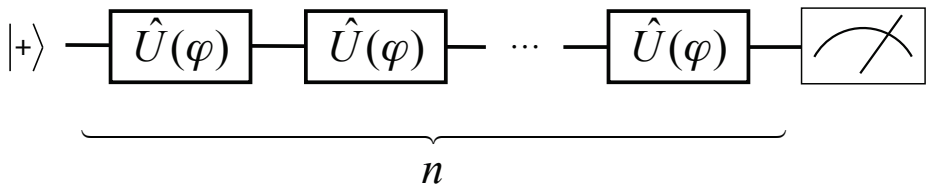

Figure 4.3: Multiround protocol with one qubit.

The simplest multiround protocol consists of one qubit, n identical phase operations, and a detector on the qubit (Fig. 4.3). The qubit is prepared in the $|+\rangle$ state. After application of n phase operations $\hat{U}(\varphi)$, the state of the qubit $|\psi\rangle$ is

$$|\psi\rangle = \left(\hat{U}(\varphi)\right)^n |+\rangle = \frac{1}{\sqrt{2}}\left[|0\rangle + e^{in\varphi}|1\rangle\right].$$

The detector measures $\hat{X}$ of the qubit. By repeating the measurement of $\hat{X}$ N times, we obtain the average of $\hat{X}$

$$\langle\hat{X}\rangle = \cos(n\varphi) \tag{4.7}$$

with the standard deviation $\Delta(X) \sim 1/\sqrt{N}$. Therefore, the standard deviation of the estimation of φ is given by

$$\Delta_\varphi = \frac{\Delta(X)}{\left|\partial\langle\hat{X}\rangle/\partial\varphi\right|} \geq \frac{\Delta(X)}{n} \sim \frac{1}{n\sqrt{N}}. \tag{4.8}$$

We have a $\sqrt{n}$ improvement in the standard deviation of the estimation with compared to Eq. (4.3). In the classical method, the amount of resources spent in the estimation is nN. The multiround protocol spends the same amount of resources with the classical method without entanglement and exceeds the SQL. Like the entanglement protocol, the phase operation is stacked in the coherence of the qubit. If the measurement is made after each operation, the information of the phase is reset after the measurement and the estimation result is limited by the SQL. Therefore, the essence of the multiround protocol is to apply a sequence of the operations before the measurement is made.

We exploit the concept of the multiround protocol to estimate the hyperfine interaction in the NV center. However, since this method requires a coherence time enough to apply several operations, it is limited by the decoherence of the NV center. At the end of this chapter, we show that our protocol is indeed restricted by the decoherence but we can still surpass the SQL within this limit.

4.2 Deterministic quantum computation with one quantum bit (DQC1)

As seen in chapter 3, it is very difficult to completely initialize the ^{15}N nitrogen nuclear spin in a pure state. Thus it would be beneficial if we can use a mixed-state

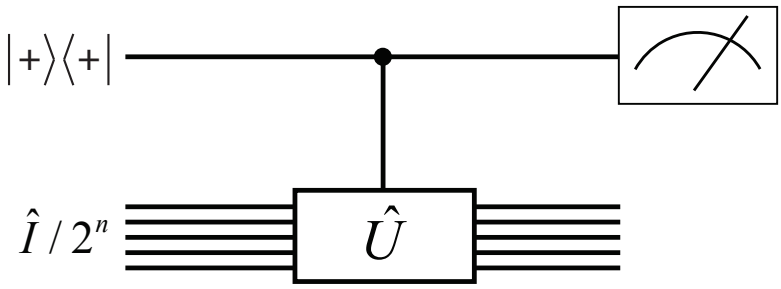

Figure 4.4: Deterministic quantum computation with one quantum bit (DQC1)

quantum algorithm in estimating the hyperfine interaction between the nitrogen nuclear spin and the electron spin in the NV center. In this section, we introduce a mixed-state quantum protocol used in this dissertation, the deterministic quantum computation with one quantum bit (DQC1).

The DQC1 model was first proposed by Knill and Laflamme [41]. It utilizes one pure control qubit (with states $\{|0\rangle, |1\rangle\}$) and n unpolarized target qubits, and performs certain operations more efficient than any classical algorithms [13, 15, 54]. Fig 4.4. depicts the circuit diagram of the DQC1 model. The unitary operation applied on the target qubits is a controlled operation. It is applied to the target qubits only if the state of the control qubit is $|1\rangle$, i.e.,

$$\tilde{U} = |1\rangle\langle 1| \otimes \hat{U}.$$

The control qubit is prepared in the $|+\rangle$ state to create the coherence. Then the initial state of the total system is a product of the control qubit and the unpolarized target qubits

$$\hat{\rho}_i = \frac{1}{2^{n+1}} \left[|0\rangle\langle 0| + |0\rangle\langle 1| + |1\rangle\langle 0| + |1\rangle\langle 1|\right] \otimes \hat{I}.$$

After the controlled operation is applied to the target qubits, the output state is given by

$$\hat{\rho}_o = \frac{1}{4}\left[(|0\rangle\langle 0| + |1\rangle\langle 1|) \otimes \hat{I} + |0\rangle\langle 1| \otimes \hat{U}^\dagger + |1\rangle\langle 0| \otimes \hat{U}\right]. \tag{4.9}$$

The reduced state of the control qubit can be obtained by taking a trace over the target qubit,

$$\hat{\rho}_o^c = \frac{1}{2}\left[|0\rangle\langle 0| + |1\rangle\langle 1| + \frac{\mathrm{Tr}[\hat{U}^\dagger]}{2^n}|0\rangle\langle 1| + \frac{\mathrm{Tr}[\hat{U}]}{2^n}|1\rangle\langle 0|\right]. \tag{4.10}$$

The coherence of the control qubit contains the normalized trace of $\hat{U}$. This information

can be extracted by measuring expectation values of $\hat{X}$ and $\hat{Y}$ on the control qubit,

$$\langle \hat{X} \rangle = \mathrm{Re}\left(\frac{\mathrm{Tr}[\hat{U}]}{2^n}\right), \ \langle \hat{Y} \rangle = -\mathrm{Im}\left(\frac{\mathrm{Tr}[\hat{U}]}{2^n}\right), \tag{4.11}$$

where $\{\hat{X}, \hat{Y}, \hat{Z}\}$ are the three Pauli operators of the control qubit denoted by

$$\begin{aligned}
\hat{X} &\equiv |1\rangle\langle 0| + |0\rangle\langle 1|, \\
\hat{Y} &\equiv i(|1\rangle\langle 0| - |0\rangle\langle 1|), \\
\hat{Z} &\equiv |0\rangle\langle 0| - |1\rangle\langle 1|.
\end{aligned}$$

The speed of the DQC1 model for the calculation of the normalized trace of $\hat{U}$ is known faster than existing classical algorithms [13].

Unlike other quantum algorithms, the output $\hat{\rho}_0$ in Eq. (4.9) is an unentangled state. This can be seen in the following way. From the spectral theorem, an arbitrary $\hat{U}$ can be written as

$$\hat{U} = \sum_{j=1}^{2^n} e^{i\phi_j} \left|v_j\right\rangle \left\langle v_j\right|, \tag{4.12}$$

where $\left|v_j\right\rangle$ is an eigenstate of $\hat{U}$ with a corresponding eigenvalue $e^{i\phi_j}$. Plugging Eq. (4.12) into Eq. (4.9), we have

$$\begin{aligned}
\hat{\rho}_o &= \frac{1}{2^{n+1}} \sum_{j=1}^{2^n} \left[|0\rangle\langle 0| + |1\rangle\langle 1| + e^{-i\phi_j}|0\rangle\langle 1| + e^{i\phi_j}|1\rangle\langle 0|\right] \otimes \left|v_j\right\rangle \left\langle v_j\right| \\
&= \frac{1}{2^n} \sum_{j=1}^{2^n} \left|\phi_j\right\rangle \left\langle \phi_j\right| \otimes \left|v_j\right\rangle \left\langle v_j\right|,
\end{aligned} \tag{4.13}$$

where $\left|\phi_j\right\rangle = \left(|0\rangle + e^{i\phi_j}|1\rangle\right)/\sqrt{2}$. Since $\hat{\rho}_o$ can be written in a separable form, $\hat{\rho}_0$ is an unentangled state [66, 37].

The correlation in charge of the exponential speedup of the DQC1 model is known as quantum discord, but there is an argument about the role of quantum discord in the DQC1 model. Detailed discussions about quantum discord and the DQC1 model can be found in several literatures including [12, 14, 42].

4.3 Two-qubit parameter estimation

The application of the DQC1 model to parameter estimation was introduced by Boixo and Somma [6]. They proposed a method to estimate an interaction between the

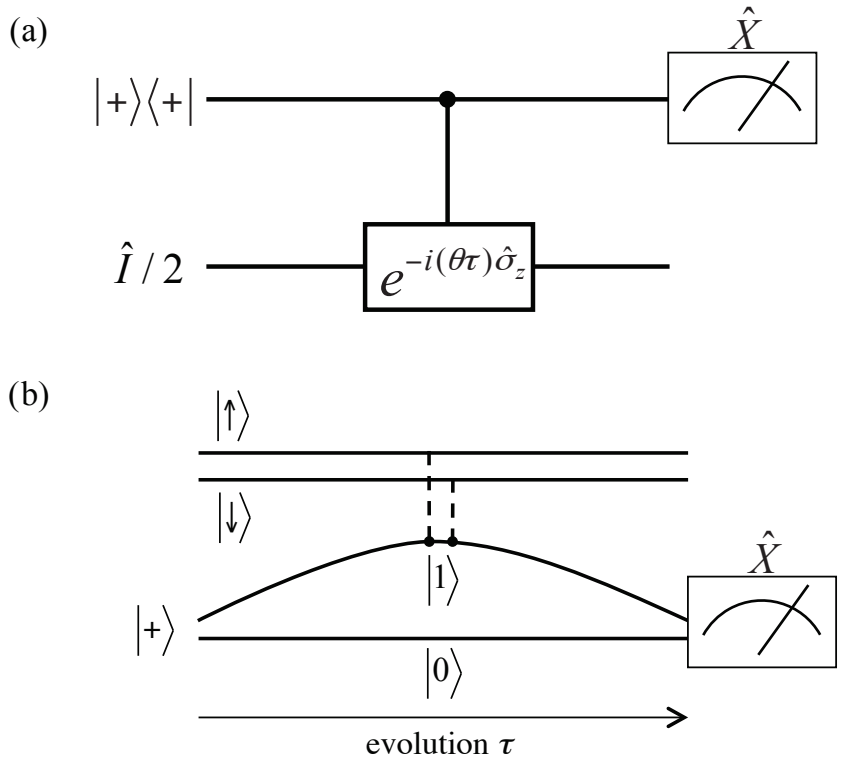

Figure 4.5: (a) Two-qubit DQC1 model with one control qubit in the pure state $|+\rangle \equiv (|0\rangle + |1\rangle)/\sqrt{2}$ and one target qubit in the unpolarized state $\hat{I}/2$. (b) Interferometric diagram of the DQC1 model

control qubit and n target qubits with the DQC1 model. Since we are interested in the estimation of the hyperfine interaction between two spins in the NV center, we briefly explain the two-qubit version of their model.

Two-qubit DQC1 model has one pure control qubit in the $|+\rangle$ state and one unpolarized target qubit (with states $\{|\uparrow\rangle, |\downarrow\rangle\}$). We use $\{\hat{\sigma}_x, \hat{\sigma}_y, \hat{\sigma}_z\}$ as the Pauli operators of the target qubit. We assume that the two qubits in the DQC1 model are coupled by the interaction

$$\hat{H}_{\mathrm{DQC1}} = |1\rangle\langle 1| \otimes \theta\hat{\sigma}_z. \tag{4.14}$$

θ is the parameter to be estimated. We use the evolution operator

$$\hat{U} = e^{-i(\theta\tau)\hat{\sigma}_z} \tag{4.15}$$

as the unitary operator to estimate of θ, (Fig. 4.5(a)). We know from the previous section that the coherence of the control qubit contains the parameter θ we are interested after

the evolution with a duration τ. We measure $\hat{X}$ to retrieve the information of θ. By repeating the evolution followed by the measurement of $\hat{X}$, we can obtain the average value of $\hat{X}$

$$\langle \hat{X} \rangle = \cos(\theta\tau), \tag{4.16}$$

which is a straightforward result from Eq. (4.11) and (4.15).

The DQC1 parameter estimation algorithm can be understood from the interferometric point of view (Fig. 4.5(b)). We assume that $|0\rangle$ and $|1\rangle$ are degenerate so that the system is described only by Eq. (4.14). Then the interaction $\hat{H}_{\mathrm{DQC1}}$ makes the energy splitting ω_c of the control qubit dependent on the state of the target qubit: $\omega_{c,\uparrow} = \theta$ for the target qubit in the spin-up state $|\uparrow\rangle$ and $\omega_{c,\downarrow} = -\theta$ for the target qubit in the spin-down state $|\downarrow\rangle$. The DQC1 parameter estimation aims to estimate the interaction strength θ with the standard deviation $\Delta_\theta = O(1/T)$ approaching the QML, where T is the total duration of the estimation process [6]. The procedures are simple: the application of the two-qubit interaction $\hat{H}_{\mathrm{DQC1}}$ for a duration τ, followed by a measurement of $\hat{X}$:

- If the target qubit is in the spin-up state $|\uparrow\rangle$, then $\hat{H}_{\mathrm{DQC1}}$ drives the precession of the control qubit with angular frequency $\omega_{c,\uparrow}$,

  $$\frac{|0\rangle + |1\rangle}{\sqrt{2}} \otimes |\uparrow\rangle \rightarrow \frac{|0\rangle + e^{-i\omega_{c,\uparrow}\tau}|1\rangle}{\sqrt{2}} \otimes |\uparrow\rangle .$$

  Before the measurement, the interaction strength θ is encoded as a phase $e^{-i\omega_{c,\uparrow}\tau}$ of the control qubit. The repeated measurements of $\hat{X}$ estimate the average value $\langle \hat{X} \rangle_\uparrow = \cos(\omega_{c,\uparrow}\tau) = \cos(\theta\tau)$, which yields the phase.

- If the target qubit is in the spin-down state $|\downarrow\rangle$, then $\hat{H}_{\mathrm{DQC1}}$ drives the precession of the control qubit with angular frequency $\omega_{c,\downarrow}$,

  $$\frac{|0\rangle + |1\rangle}{\sqrt{2}} \otimes |\downarrow\rangle \rightarrow \frac{|0\rangle + e^{-i\omega_{c,\downarrow}\tau}|1\rangle}{\sqrt{2}} \otimes |\downarrow\rangle .$$

  Before the measurement, the interaction strength θ is encoded as a phase $e^{-i\omega_{c,\downarrow}\tau}$ of the control qubit. The repeated measurements of $\hat{X}$ estimate the average value $\langle \hat{X} \rangle_\downarrow = \cos(\omega_{c,\downarrow}\tau) = \cos(\theta\tau)$, which extracts the phase.

- Now the target qubit is in the unpolarized state, i.e., an equal, incoherent mixture of $|\uparrow\rangle$ and $|\downarrow\rangle$. Then the repeated measurements of $\hat{X}$ estimates the equally weighted average of $\langle\hat{X}\rangle_\uparrow$ and $\langle\hat{X}\rangle_\downarrow$:

$$\langle\hat{X}\rangle = \frac{1}{2}(\langle\hat{X}\rangle_\uparrow + \langle\hat{X}\rangle_\downarrow) = \cos(\theta\tau).$$

  A distinctive feature of the above parameter estimation process is the absence of any two-qubit entanglement [42].

For a given standard deviation Δ_X ($\ll 1$ under typical situations) in estimating $\langle\hat{X}\rangle$, the DQC1 model gives an estimate to the interaction strength θ with a standard deviation

$$\Delta_\theta = \frac{\Delta_X}{|\partial\langle\hat{X}\rangle/\partial\theta|} = \frac{\Delta_X}{\tau|\sin(\theta\tau)|} \geq \frac{\Delta_X}{\tau}. \tag{4.17}$$

By regarding the duration τ of the estimation as a resource, the QML scaling $\Delta_\theta = O(1/\tau)$ is achieved if τ could be chosen such that $|\sin(\theta\tau)| \approx 1$. However, due to the limited prior knowledge about θ (the parameter to be estimated), we cannot always ensure $|\sin(\theta\tau)| \approx 1$, especially when a small standard deviation $\Delta_\theta \to 0$ (corresponding to large $\tau \to \infty$) is required.

To address this issue, Boixo and Somma quantified the prior knowledge about θ by a standard deviation Δ_0 and utilized the adaptive Bayesian inference to reduce the standard deviation successively [6]. The essential idea of this approach can be understood *qualitatively* as follows. In order to ensure $|\sin(\theta\tau)| \approx 1$ and hence the QML, the largest τ is roughly $1/\Delta_0$. Under this restriction, the minimal standard deviation for the estimation of θ is given by Eq. (4.17) as $\sim \Delta_X\Delta_0 \ll \Delta_0$. Therefore, the DQC1 measurements with standard deviation Δ_X refines our knowledge about the interaction strength θ from a large standard deviation Δ_0 to a much smaller one $\sim \Delta_X\Delta_0$. By iterating this procedure, the standard deviation Δ_θ would decrease successively as $\Delta_0 \to \Delta_X\Delta_0 \to \Delta_X^2\Delta_0 \to \cdots$. With the aid of the adaptive Bayesian inference, Boixo and Somma performed a quantitative analysis about this iteration and concluded that the QML $\Delta_\theta = O(1/T)$ could be achieved for an arbitrary desired standard deviation, where $T = \sum\tau$ is the total duration of the estimation process [6].

4.4 DQC1 parameter estimation to NV center

4.4.1 Two-qubit DQC1 parameter estimation with an arbitrary target qubit state

While the original DQC1 model and Boixo's method use the unpolarized target qubit, we verify that the two-qubit DQC1 model in Fig. 4.5(a) can be extended to an arbitrary polarized target qubit. This feature is very important since the nitrogen nuclear spin acquires a partial polarization during the initialization of the electron spin.

We replace the initial state of the target qubit $\hat{I}/2$ in Fig. 4.5 with $\hat{I}/2 + q_z\hat{\sigma}_z/2$, where q_z is the polarization of the target qubit. In this case, the third bullet in Sec. 4.3 is revised as

- The target qubit is in an incoherent mixture of $|\uparrow\rangle$ [with weight $(1 + q_z)/2$] and $|\downarrow\rangle$ [with weight $(1 - q_z)/2$]. Then the repeated measurements of $\hat{X}$ estimate the weighted average of $\langle\hat{X}\rangle_\uparrow$ and $\langle\hat{X}\rangle_\downarrow$:

$$\langle\hat{X}\rangle = \frac{1+q_z}{2}\langle\hat{X}\rangle_\uparrow + \frac{1-q_z}{2}\langle\hat{X}\rangle_\downarrow = \cos(\theta\tau).$$

In other words, $\langle\hat{X}\rangle$ is independent on the initial state of the target qubit. Thus the estimation of θ is also independent on the target qubit state. The detailed proof of this extended two-qubit DQC1 model can be found in Appendix.

4.4.2 Direct application of DQC1 parameter estimation to NV center

We consider a negatively charged NV center in diamond consisting of a substitutional ^{15}N atom and a neighboring carbon vacancy. Its electronic ground state is a two-electron spin triplet described by a spin-1 operator $\hat{\mathbf{S}}$, with a zero-field splitting $D \approx 2.87$ GHz (described by the term $D\hat{S}_z^2$) between the $|m_s = 0\rangle$ state and the $|m_s = \pm 1\rangle$ states. Under an external magnetic field B along the N-V axis (defined as the z direction), the Zeeman term $g_e\mu_B B\hat{S}_z$ with $g_e = 2.0023$ shifts the state $|m_s = +1\rangle$ away from the other two states under a moderate magnetic field $B \sim 0.2$ T (see Fig. 4.6). Thus we identify $|0\rangle \equiv |m_s = 0\rangle$ and $|1\rangle \equiv |m_s = -1\rangle$ as the two states of the control qubit of the

DQC1 model and use $\hat{X}, \hat{Y}, \hat{Z}$ as the three Pauli matrices for this qubit. The electron spin $\hat{\mathbf{S}}$ is coupled to the neighboring ^{15}N nuclear spin-1/2 $\hat{\mathbf{I}}$ (with the two-fold degeneracy lifted by the Zeeman term $g_N \mu_N B \hat{I}_z$, where $g_N = -0.5664$ [23]) through the hyperfine interaction $A\hat{S}_z\hat{I}_z + (A_\perp/2)(\hat{S}_+\hat{I}_- + \hat{S}_-\hat{I}_+)$, where $A \approx 3.03$ MHz and $A_\perp \approx 3.65$ MHz [23, 55]. We regard this nuclear spin-1/2 as the mixed-state target qubit of the DQC1 model and use $\hat{\sigma}_x, \hat{\sigma}_y, \hat{\sigma}_z$ as the three Pauli matrices $2\hat{I}_x, 2\hat{I}_y, 2\hat{I}_z$ for this qubit. The diagonal part $A\hat{S}_z\hat{I}_z$ of the hyperfine interaction makes the nuclear (electron) spin splitting energy dependent on the state of the electron (the nucleus). Thus $A\hat{S}_z\hat{I}_z$ plays the central role in coherent control and readout of the electron and nuclear spin states. The hyperfine interaction strength A is the parameter to be estimated.

In the two-qubit subspace, the Hamiltonian $\hat{H} = \hat{H}_0 + \hat{H}_{\text{mix}}$ consists of the diagonal part

$$\hat{H}_0 = \frac{1}{2} g_N \mu_N B \hat{\sigma}_z + |1\rangle\langle 1| \otimes (D' - \frac{1}{2} A \hat{\sigma}_z)$$

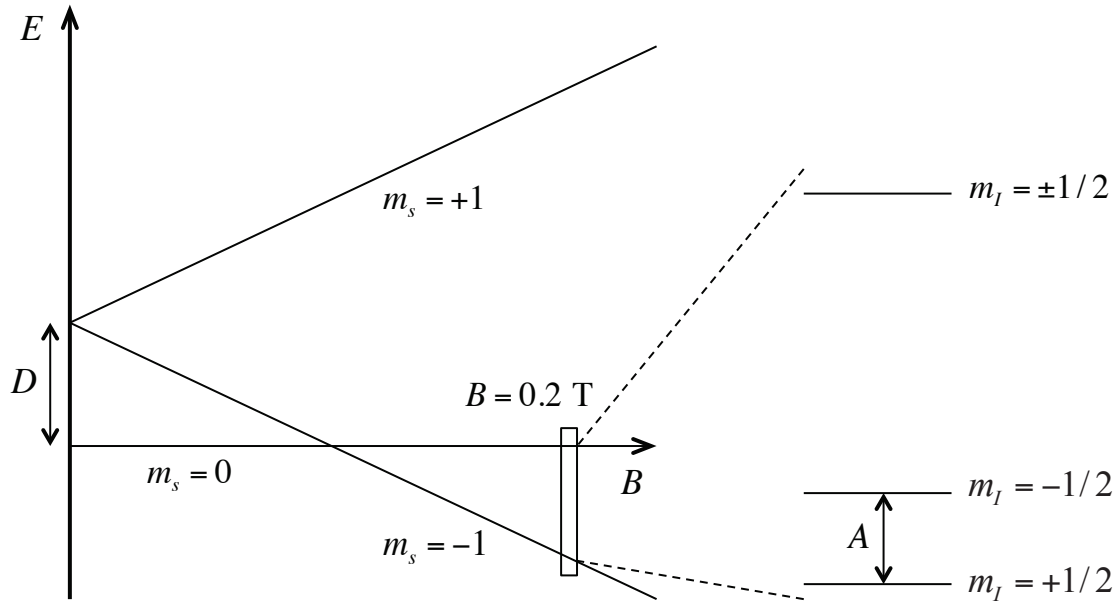

Figure 4.6: Energy level diagram of the ground state of an NV center in diamond. The hyperfine energy splitting at $B = 0.2$ T is sketched within the $|m_s = 0\rangle$ and $|m_s = -1\rangle$ manifold. $D = 2.87$ GHz is the zero field splitting of the electron spin, and A is the longitudinal hyperfine interaction to be estimated. The nuclear Zeeman splitting is omitted in the diagram.

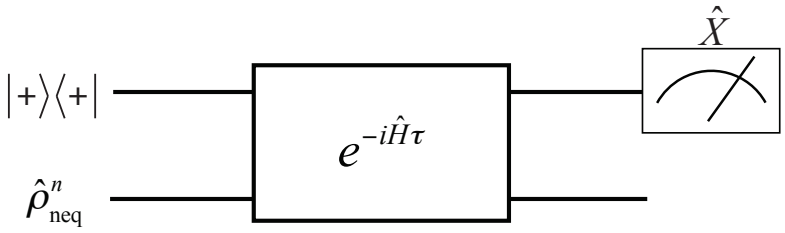

Figure 4.7: Direct application of the DQC1 model to estimate the hyperfine interaction strength A in NV center. Since the Hamiltonian $\hat{H}$ includes the spin-flip hyperfine interaction $\hat{H}_{\rm mix}$, the evolution operator has a different form from the $\hat{H}_{\rm DQC1}$ in Eq. (4.14)

and the off-diagonal part

$$\hat{H}_{\rm mix} = (A_\perp/\sqrt{2})(|0,\downarrow\rangle\langle 1,\uparrow| + |1,\uparrow\rangle\langle 0,\downarrow|).$$

The diagonal part $\hat{H}_0$ accounts for the free nuclear spin precession with angular frequency $g_N\mu_N B$, the free electron spin precession with angular frequency $D' \equiv D - g_e\mu_B B$, and the projection $|1\rangle\langle 1| \otimes (-A\hat{\sigma}_z/2)$ of the diagonal hyperfine interaction $A\hat{S}_z\hat{I}_z$ in the two-qubit subspace. The off-diagonal part $\hat{H}_{\rm mix}$ is the projection of the off-diagonal hyperfine interaction $(A_\perp/2)(\hat{S}_+\hat{I}_- + \hat{S}_-\hat{I}_+)$ in the two-qubit subspace. The diagonal hyperfine interaction term $|1\rangle\langle 1|\otimes(-A\hat{\sigma}_z/2)$ in $\hat{H}_0$ corresponds to $\hat{H}_{\rm DQC1}$ in Eq. (4.14) with $\theta \leftrightarrow (-A/2)$. It makes the precession frequency ω_e of the electron spin dependent on the hyperfine interaction strength A and the nuclear spin state: $\omega_{e,\uparrow} = D' - A/2$ for the nuclear spin state being $|\uparrow\rangle$ and $\omega_{e,\downarrow} = D' + A/2$ for the nuclear spin state being $|\downarrow\rangle$. Therefore, following the procedure in Fig. 4.5(a), the interaction strength A is encoded as a phase of the electron spin and subsequently extracted by estimating $\langle\hat{X}\rangle$.

As schematically shown in Fig. 4.7, the electron spin needs to be prepared in the superposition $(|0\rangle + |1\rangle)/\sqrt{2}$. This can be achieved by optical pumping followed by a coherent rotation [36]. However, this preparation process inevitably influences the nuclear spin and changes its state from the unpolarized thermal equilibrium state $\hat{\rho}^n_{\rm eq} = \hat{I}/2$ to a state $\hat{\rho}^n_{\rm neq} = \hat{I}/2 + q_z\hat{\sigma}_z/2$ with a finite polarization $q_z = {\rm Tr}[\hat{\rho}^n_{\rm neq}\hat{\sigma}_z]$ [38]. Then the two qubits evolve under the Hamiltonian $\hat{H}$ for a duration τ, followed by a measurement of $\langle\hat{X}\rangle$. Below we calculate $\langle\hat{X}\rangle$ without $\hat{H}_{\rm mix}$ and then taking it into account by perturbation theory.

Without $\hat{H}_{\rm mix}$, the two qubits are driven by $\hat{H}_0$, which has four eigenstates $|0,\uparrow\rangle$,

$|0,\downarrow\rangle, |1,\uparrow\rangle, |1,\downarrow\rangle$. The physics is similar to the DQC1 model described in the previous subsection:

- If the nuclear spin is in the spin-up state $|\uparrow\rangle$, then $\hat{H}_0$ drives the precession of the electron spin qubit with angular frequency $\omega_{e,\uparrow}$ and the repeated measurements of $\hat{X}$ estimate $\langle\hat{X}\rangle_\uparrow = \cos(\omega_{e,\uparrow}\tau)$.

- If the nuclear spin is in the spin-down state $|\downarrow\rangle$, then $\hat{H}_0$ drives the precession of the electron spin qubit with angular frequency $\omega_{e,\downarrow}$ and the repeated measurements of $\hat{X}$ estimate $\langle\hat{X}\rangle_\downarrow = \cos(\omega_{e,\downarrow}\tau)$.

- Now the nuclear spin is in an incoherent mixture of $|\uparrow\rangle$ [with weight $(1+q_z)/2$] and $|\downarrow\rangle$ [with weight $(1-q_z)/2$]. Then the repeated measurements of $\hat{X}$ estimate the weighted average of $\langle\hat{X}\rangle_\uparrow$ and $\langle\hat{X}\rangle_\downarrow$:

$$\begin{aligned}\langle\hat{X}\rangle &= \frac{1+q_z}{2}\langle\hat{X}\rangle_\uparrow + \frac{1-q_z}{2}\langle\hat{X}\rangle_\downarrow \\ &= \frac{1+q_z}{2}\cos\left[\left(D' - \frac{A}{2}\right)\tau\right] + \frac{1-q_z}{2}\cos\left[\left(D' + \frac{A}{2}\right)\tau\right] \\ &= \cos(D'\tau)\cos\left(\frac{A\tau}{2}\right) + q_z\sin(D'\tau)\sin\left(\frac{A\tau}{2}\right) \end{aligned} \tag{4.18}$$

Then we consider the complications caused by the off-diagonal part $\hat{H}_{\text{mix}}$. To reduce its detrimental effect on the parameter estimation, we consider a suitable magnetic field strength (e.g., $B = 0.2$ T, as indicated in Fig. 4.6 and used in our estimation, see Sec. 4.6.2) so that $|D'| \gg |A_\perp|$. In this case, we can use perturbation theory to treat $\hat{H}_{\text{mix}}$, which modifies the eigenstates and eigenenergies of the two-qubit Hamiltonian $\hat{H} = \hat{H}_0 + \hat{H}_{\text{mix}}$:

1. $\hat{H}_{\text{mix}}$ changes the eigenstates of $\hat{H}$ from $[|0,\uparrow\rangle, |0,\downarrow\rangle, |1,\uparrow\rangle, |1,\downarrow\rangle]$ to $[|0,\uparrow\rangle, |\widetilde{0,\downarrow}\rangle, |\widetilde{1,\uparrow}\rangle, |1,\downarrow\rangle]$, where

$$\begin{aligned}|\widetilde{0,\downarrow}\rangle &= [1 - O(\eta^2)]\,|0,\downarrow\rangle + O(\eta)\,|1,\uparrow\rangle\,, \\ |\widetilde{1,\uparrow}\rangle &= [1 - O(\eta^2)]\,|1,\uparrow\rangle + O(\eta)\,|0,\downarrow\rangle\,,\end{aligned}$$

   and $\eta \equiv A_\perp/(D' + g_N\mu_N B - A/2) \sim 10^{-3}$ for $B = 0.2$ T. In other words, $\hat{H}_{\text{mix}}$ introduces new $O(\eta)$ components into the eigenstates. It can be readily verified that this changes $\langle\hat{X}\rangle$ by $O(\eta^2)$.

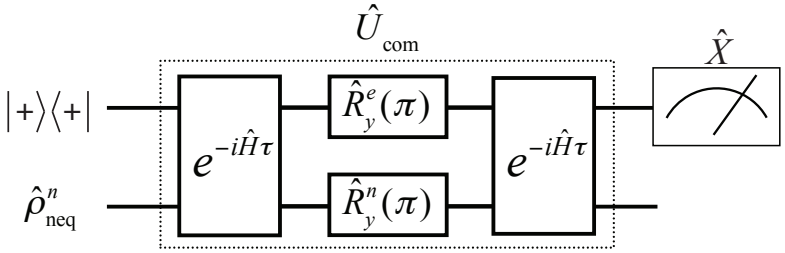

Figure 4.8: Combination of spin echo and the DQC1 model.

2. $\hat{H}_{\text{mix}}$ changes the eigenenergy of $|0,\downarrow\rangle$ ($|1,\uparrow\rangle$) by a small amount $-\delta$ ($+\delta$), where $\delta = \eta A_\perp/2 + O(\eta^2 A_\perp)$. This in turn changes the precession frequencies of the electron spin from $\omega_{e,\mu}$ to $\tilde{\omega}_{e,\mu} = \omega_{e,\mu} + \delta$ ($\mu = \uparrow, \downarrow$). Therefore, the average value $\langle\hat{X}\rangle$ is obtained from Eq. (4.18) by renormalizing $\omega_{e,\mu}$ with $\tilde{\omega}_{e,\mu}$ ($\mu = \uparrow, \downarrow$).

A detailed calculation about the above process is included in Appendix. Collecting both corrections discussed above, we obtain

$$\langle\hat{X}\rangle = \cos[(D' + \delta)\tau]\cos(\frac{A}{2}\tau) + q_z \sin[(D' + \delta)\tau]\sin(\frac{A}{2}\tau) + O(\eta^2). \tag{4.19}$$

It contains not only A but also undesired parameters such as D' (free electron spin precession frequency), δ (energy shift by $\hat{H}_{\text{mix}}$), and q_z (partial nuclear spin polarization). For an accurate estimation of A, it is desirable to eliminate these undesired parameters from $\langle\hat{X}\rangle$ by modifying the DQC1 protocol.

4.5 Quantum estimation circuit of hyperfine interaction

4.5.1 Eliminating undesired parameters by spin echo

To remove the dependence on the undesired parameters in $\langle\hat{X}\rangle$, we combine the DQC1 model with the spin-echo technique by replacing the free evolution $e^{-i\hat{H}\tau}$ in Fig. 4.7 with the composite evolution [see Fig. 4.8]

$$\hat{U}_{\text{com}} = e^{-i\hat{H}\tau}\hat{R}^n_y(\pi)\hat{R}^e_y(\pi)e^{-i\hat{H}\tau},$$

which consists of an electron spin π rotation $\hat{R}^e_y(\pi) = e^{-i\pi\hat{Y}/2} = -i\hat{Y}$ and a nuclear spin π rotation $\hat{R}^n_y(\pi) = e^{-i\pi\hat{\sigma}_y/2} = -i\hat{\sigma}_y$ sandwiched by the free evolution $e^{-i\hat{H}\tau}$. Using the

relation $e^{-i\hat{H}\tau}\hat{Y} = \hat{Y}e^{-i(\hat{Y}\hat{H}\hat{Y})\tau}$ (and $e^{-i\hat{H}\tau}\hat{\sigma}_y = \hat{\sigma}_y e^{-i(\hat{\sigma}_y\hat{H}\hat{\sigma}_y)\tau}$), $\hat{U}_{\rm com}$ is rewritten as

$$\hat{U}_{\rm com} = \hat{R}^e_y(\pi)\hat{R}^n_y(\pi)\left(e^{-i(\hat{\sigma}_y\hat{Y}\hat{H}\hat{Y}\hat{\sigma}_y)\tau}e^{-i\hat{H}\tau}\right). \tag{4.20}$$

This composite evolution contains a spin echo (the part inside the parenthesis) for the electron and the nucleus, which eliminates the free precession of the electron spin and the nuclear spin. To analyze $\hat{U}_{\rm com}$ in more detail, we first ignore the off-diagonal part $\hat{H}_{\rm mix}$ and then take it into account by perturbation theory.

Without $\hat{H}_{\rm mix}$, the Hamiltonian $\hat{H}'_0 \equiv \hat{\sigma}_y\hat{Y}\hat{H}_0\hat{Y}\hat{\sigma}_y$ is given by

$$\begin{aligned}\hat{H}'_0 &= \hat{\sigma}_y\hat{Y}\left[\frac{1}{2}g_N\mu_N B\hat{\sigma}_z + |1\rangle\langle 1|\otimes(D' - \frac{A}{2}\hat{\sigma}_z)\right]\hat{Y}\hat{\sigma}_y \\ &= -\frac{1}{2}g_N\mu_N B\hat{\sigma}_z + |0\rangle\langle 0|\otimes(D' + \frac{A}{2}\hat{\sigma}_z) \\ &= -\frac{1}{2}g_N\mu_N B\hat{\sigma}_z + \frac{A}{2}\hat{\sigma}_z - |1\rangle\langle 1|\otimes(D' + \frac{A}{2}\hat{\sigma}_z) + D'. \end{aligned}\tag{4.21}$$

D' in the last line is a constant and can be dropped since it does not contribute to the dynamics of the system. Then $\hat{H}'_0$ commutes with $\hat{H}_0$ and $\hat{U}_{\rm com}$ reduces to

$$\hat{U}^{(0)}_{\rm com} = R^e_y(\pi)R^n_y(\pi)e^{-i(\hat{H}'_0+\hat{H}_0)\tau} = R^e_y(\pi)R^n_y(\pi)e^{-iA\tau\hat{\sigma}_z/2}e^{-i\hat{H}_{\rm echo}\tau},$$

where $\hat{H}_{\rm echo} = |1\rangle\langle 1|\otimes(-A\hat{\sigma}_z)$ corresponds to $\hat{H}_{\rm DQC1}$ in Eq. (4.14) with $\theta \leftrightarrow -A$. The operation $R^n_y(\pi)e^{-iA\tau\hat{\sigma}_z/2}$ on the nuclear spin alone can be dropped since it does not influence our measurement on the electron spin. Therefore, the composite evolution becomes $\hat{U}^{(0)}_{\rm com} = R^e_y(\pi)e^{-i\hat{H}_{\rm echo}\tau}$, in which all the undesired parameters have been eliminated.

In the presence of $\hat{H}_{\rm mix}$, $\hat{H}'$ consists of the diagonal part $\hat{H}_0$ and the off-diagonal part $\hat{H}_{\rm mix}$. Note that we have $\hat{\sigma}_y\hat{Y}\hat{H}_{\rm mix}\hat{Y}\hat{\sigma}_y = \hat{H}_{\rm mix}$. Similar to the two-step analysis leading to Eq. (4.42), $\hat{H}_{\rm mix}$ modifies the eigenstates and eigenenergies of $\hat{H} = \hat{H}_0 + \hat{H}_{\rm mix}$ and $\hat{H}' = \hat{H}'_0 + \hat{H}_{\rm mix}$:

1. $\hat{H}_{\rm mix}$ introduces new $O(\eta)$ components into the eigenstates of $\hat{H}$ and $\hat{H}'$. This changes $\langle\hat{X}\rangle$ by $O(\eta^2)$.

2. For the Hamiltonian $\hat{H}$, the presence of $\hat{H}_{\rm mix}$ changes the eigenenergy of $|0,\downarrow\rangle$ ($|1,\uparrow\rangle$) by $-\delta$ ($+\delta$). For the Hamiltonian $\hat{H}'$, the presence of $\hat{H}_{\rm mix}$ changes the eigenenergy of $|0,\downarrow\rangle$ ($|1,\uparrow\rangle$) by $+\delta$ ($-\delta$). In other words, the opposite energy shifts for $\hat{H}$ and $\hat{H}'$ induced by $\hat{H}_{\rm mix}$ cancel each other in the evolution $\hat{U}_{\rm com}$.

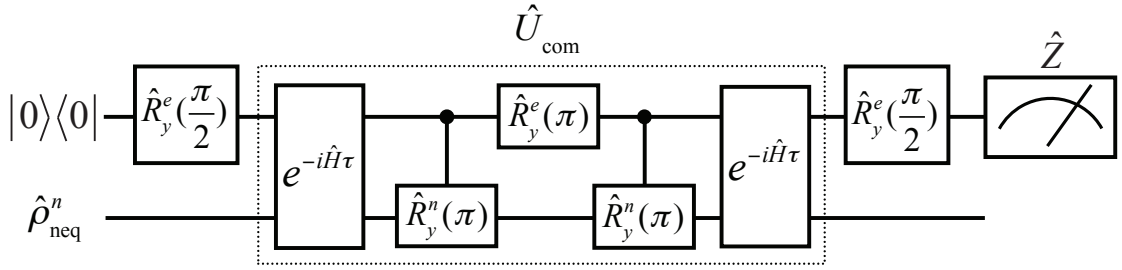

Figure 4.9: Quantum circuit for a single estimation of the hyperfine interaction strength A in the NV center. The nuclear spin is initially in a partially polarized sate $\hat{\rho}_{\text{neq}}^n = (\hat{I} + q_z\hat{\sigma}_z)/2$.

For $\langle\hat{X}\rangle$, the composite evolution including both corrections discussed above is equivalent to

$$\hat{U}_{\text{com}} = \hat{R}_y^e(\pi)e^{-i\hat{H}_{\text{echo}}\tau} + O(\eta^2),$$

i.e., the spin echo eliminates all the named undesired parameters and the effective evolution $\hat{U}_{\text{com}}$ for the NV center recovers the DQC1 evolution $e^{-i\hat{H}_{\text{DQC1}}\tau}$ up to a trivial electron spin π rotation $\hat{R}_y^e(\pi)$. A detailed calculation of $\langle\hat{X}\rangle$ is found in Appendix.

4.5.2 Quantum estimation circuit

Fig. 4.9 gives the sequence of quantum operations for a single estimation of the hyperfine interaction strength A in the NV center:

1. The electron spin is prepared into the pure state $|0\rangle$ by optical pumping [36]. A subsequent $\pi/2$ rotation $\hat{R}_y^e(\pi/2)$ initializes the electron spin into the superposition $|+\rangle = (|0\rangle + |1\rangle)/\sqrt{2}$. The nuclear spin is a partially polarized state $\hat{\rho}_n = \hat{I}/2 + q_z\hat{\sigma}_z/2$. This initial density matrix $\hat{\rho}_{\text{initial}} = |+\rangle\langle+| \otimes \hat{\rho}_n$ coincides with the initial density matrix $\hat{\rho}_{\text{DQC1}} = |+\rangle\langle+| \otimes \hat{\rho}_{\text{tar}}$ of the DQC1 model, where the target qubit state $\hat{\rho}_{\text{tar}}$ also has an arbitrary polarization.

2. The two qubits experience a composite evolution (within the dashed box in Fig. 4.9), which consists of a free evolution $e^{-i\hat{H}\tau}$, a controlled nuclear spin π rotation $\tilde{R}_y^n(\pi) = |1\rangle\langle 1| \otimes (-i\hat{\sigma}_y) + |0\rangle\langle 0|$, an electron spin rotation $\hat{R}_y^e(\pi)$, another controlled nuclear spin π rotation $\tilde{R}_y^n(\pi)$, and another free evolution $e^{-i\hat{H}\tau}$. The equal-

ity $\tilde{R}_y^n(\pi)\hat{R}_y^e(\pi)\tilde{R}_y^n(\pi) = \hat{R}_y^n(\pi)\hat{R}_y^e(\pi)$ shows that this composite evolution coincides with $\hat{U}_{\rm com}$ in Sec. 4.5.1.

3. A $\pi/2$ rotation $\hat{R}_y^e(\pi/2)$ is applied to the electron spin, followed by a measurement of $\hat{Z}$ through optical methods [8, 7]. This measurement estimates

$$\begin{aligned}\langle\hat{Z}\rangle &= \mathrm{Tr}\,\hat{Z}\hat{R}_y^e(\pi/2)\hat{U}_{\rm com}\hat{\rho}_{\rm initial}\hat{U}_{\rm com}^\dagger[\hat{R}_y^e(\pi/2)]^\dagger \\ &= \mathrm{Tr}\,\hat{X}e^{-i\hat{H}_{\rm echo}\tau}\hat{\rho}_{\rm initial}e^{i\hat{H}_{\rm echo}\tau} + O(\eta^2).\end{aligned}$$

Since the evolution $e^{-i\hat{H}_{\rm echo}\tau} = e^{-i\hat{H}_{\rm DQC1}\tau}|_{\theta\to -A}$ has the same form as the DQC1 model, the average value is

$$\langle\hat{Z}\rangle = \cos(A\tau) + O(\eta^2). \tag{4.22}$$

The electron spin rotation $\hat{R}_y^e(\pi/2)$ $[\hat{R}_y^e(\pi)]$ in the circuit is achieved by a $\pi/2$ pulse (π pulse) with the central frequency $|D'|$ and the bandwidth $\gg A/2$, so that both transitions $|0,\uparrow\rangle \leftrightarrow |1,\uparrow\rangle$ and $|0,\downarrow\rangle \leftrightarrow |1,\downarrow\rangle$ are equally excited. The controlled nuclear spin rotation $\tilde{R}_y^n(\pi)$ is achieved by a π pulse centered at the resonant frequency $A - g_N\mu_N B - \delta$ of the transition $|1,\uparrow\rangle \to |1,\downarrow\rangle$. The duration τ of the free evolution can be chosen in the experiment as $\tau > 1/A \sim 0.1\ \mu$s. The electron spin rotation occurs within a few nanoseconds and hence can be regarded as instantaneous [27, 28]. However, the controlled nuclear spin π rotation takes $\tau_n \sim$ a few microseconds, comparable to the free evolution time τ. Detailed analysis in appendix shows that incorporation of τ_n amounts to replacing the free evolution time τ in Eq. (4.22) by the sum $(\tau + \tau_n)$. For brevity, we use τ to denote $(\tau + \tau_n)$ from now on.

In arriving at Eq. (4.22), we have assumed that all the gate operations in the circuit and the measurements of $\hat{Z}$ are free of errors. In a realistic experiment, the most basic errors include the deviation of the nuclear spin rotation angle from π in the controlled π rotation $\tilde{R}_y^n(\pi)$ and the finite electron spin coherence time T_2^e:

- Nuclear spin rotation error. The two controlled nuclear spin π rotations $\tilde{R}_y^n(\pi)$ in the quantum estimation circuit (Fig. 4.9) are subjected to random errors, which may come from our limited prior knowledge (which becomes more and more precise after each successive estimation step) about the interaction strength A or

other experimental sources. For the actual rotation angle $(\pi + 2\epsilon)$ differing from π by an error 2ϵ, the actual controlled rotation $\tilde{R}_y^n(\pi, \epsilon) = \tilde{R}_y^n(\pi) + \tilde{\delta}_y^n(\pi)$ differs from the ideal one $\tilde{R}_y^n(\pi)$ by

$$\tilde{\delta}_y^n(\pi) = |1\rangle\langle 1| \otimes (-\epsilon + i\frac{\epsilon^2}{2}\hat{\sigma}_y) + O(\epsilon^3).$$

For the first controlled rotation being $\tilde{R}_y^n(\pi, \epsilon_a)$ and the second controlled rotation being $\tilde{R}_y^n(\pi, \epsilon_b)$, the actual quantity estimated by the quantum circuit $M(\tau)$ is

$$\begin{aligned}\langle \hat{Z}_\epsilon \rangle = &\left(1 - \frac{\langle \epsilon_a^2 \rangle + \langle \epsilon_b^2 \rangle}{2}\right)\cos(A\tau) \\ &+ \langle \epsilon_a \epsilon_b \rangle + \langle \epsilon_a \rangle O(\eta) + \langle \epsilon_b \rangle O(\eta) + O(\eta^2),\end{aligned}$$

The first source of error is our ignorance about A. In the k-th estimation step, our limited prior knowledge about A (as quantified by the standard deviation Δ_{k-1}, see Sec. 4.6.1) and hence the resonant frequency $A - g_N\mu_N B - \delta$ of the transition $|1, \uparrow\rangle \rightarrow |1, \downarrow\rangle$ makes it impossible to construct an exact π pulse for this transition. The typical detuning for this transition is Δ_{k-1}. The typical rotation angle deviates from the ideal value π by an amount $\pi\Delta_{k-1}^2/(2\Omega^2) \sim 10^{-3}$, the same order of magnitude as $O(\eta)$, for the Rabi frequency $\Omega = 500$ kHz used in our estimation. Thus every term in the second line of the above equation has the same order of $\sim 10^{-6}$, which allows us to replace the second line by $O(\eta^2)$. For ϵ_a and ϵ_b being independent, we obtain

$$\langle \hat{Z}_\epsilon \rangle = (1 - \varepsilon^2)\cos(A\tau) + O(\eta^2),$$

where $\varepsilon^2 = \langle \epsilon_a^2 \rangle = \langle \epsilon_b^2 \rangle$. For other experimental sources, the errors are typically random with $\langle \epsilon_a \rangle = \langle \epsilon_b \rangle = \langle \epsilon_a \epsilon_b \rangle = 0$, so that the above equation still holds.

- Electron spin decoherence. The electron spin in the NV center is subjected to decoherence by the surrounding ^{13}C nuclear spin bath. The coherence time of the electron spin in the ground state is $T_2^e \sim 350\ \mu$s under the natural abundance of the ^{12}C isotope (98.8%), and it is extended to 1.8 ms under the ultrapure ^{12}C abundance (99.7%) at room temperature [29, 3]. By incorporating the electron spin relaxation (with the relaxation time $T_1^e = 5.9$ ms [48]) and decoherence in

the Lindblad form, it is straightforward to show that the quantity estimated by the quantum circuit is no longer Eq. (4.22) but instead

$$\langle \hat{Z}_d \rangle = e^{-2\tau/T_2^e} \cos(A\tau) + O(\eta^2).$$

In summary, in the presence of errors, the quantity estimated by the quantum circuit in Fig. 4.9 is given by

$$\langle \hat{Z} \rangle = Q(\tau) \cos(A\tau) + O(\eta^2), \tag{4.23}$$

where $Q(\tau) = 1 - \varepsilon^2$ for the nuclear spin rotation error of magnitude ε and $Q(\tau) = e^{-2\tau/T_2^e}$ for a finite electron spin coherence time T_2^e. In our estimation, we use $B = 0.2$ T so that the correction for the hyperfine interaction $O(\eta^2) \sim 10^{-6}$.

4.6 Quantum measurement protocol

In this section, first we describe in detail the procedure of the entire estimation protocol: the successive adaptation of the quantum circuit for dramatically reduced standard deviation by combining our prior knowledge with the outcomes of the previous measurements through adaptive Bayesian inference. Next, we demonstrate that this protocol approaches the QML $\Delta_{\mathrm{QML}} = O(1/T)$ for the ideal case. Finally, we include the essential errors (the nuclear spin rotation error and the electron spin decoherence) and show that our protocol still exceeds the SQL.

4.6.1 Estimation procedure

We use $M(\tau)$ to denote the quantum estimation circuit in Fig. 4.9, whose total duration is 2τ. A single run of the circuit $M(\tau)$ returns two outcomes: $+1$ for the electron spin in the state $|0\rangle$ or -1 for the electron spin in the state $|1\rangle$, with corresponding probabilities $p_{\pm 1} = [1 \pm \langle \hat{Z} \rangle]/2$. An estimator of the average value $\langle \hat{Z} \rangle$ [Eq. (4.23)] is obtained by averaging over the outcomes of repeated running of the circuit. For example, averaging over N measurements produces Z, a single estimator of $\langle \hat{Z} \rangle$. By the central limit theorem, for relatively large N (e.g., $N \gtrsim 100$), *this estimator obeys the Gaussian distribution* $\mathcal{N}(\langle \hat{Z} \rangle, \zeta)$ centered at $\langle \hat{Z} \rangle$ with a standard deviation $\zeta = 1/\sqrt{N}$. Alternatively, we

can also say that *the average value* $\langle\hat{Z}\rangle$ *obeys the Gaussian distribution* $\mathcal{N}(Z,\zeta)$, which actually means that the difference $\langle\hat{Z}\rangle - Z$ obeys the Gaussian distribution $\mathcal{N}(0,\zeta)$.

The estimation begins with a prior knowledge of the hyperfine interaction strength A. It is quantified by a Gaussian distribution $\mathcal{N}(A_0,\Delta_0)$ centered at A_0 with a relatively large standard deviation Δ_0, which quantifies our ignorance about A. This prior knowledge tells us, with a 95% confidence, that A lies within the interval $[A_0 - 1.96\Delta_0, A_0 + 1.96\Delta_0]$. From the prior knowledge $\mathcal{N}(A_0,\Delta_0)$, we construct the quantum circuit $M(\tau_1)$ for the first estimation, which provides a new knowledge about A, as quantified by a Gaussian distribution $\mathcal{N}(\bar{A}_1,\bar{\Delta}_1)$. Through the Bayesian inference, this new knowledge is combined with the prior knowledge to produce an updated knowledge about A, quantified by a Gaussian distribution $\mathcal{N}(A_1,\Delta_1)$ with a smaller standard deviation $\Delta_1 < \Delta_0$. Therefore, the first estimation step refines our knowledge about A from $\mathcal{N}(A_0,\Delta_0)$ to $\mathcal{N}(A_1,\Delta_1)$ (with $\Delta_1 < \Delta_0$), which in turn serves as the prior knowledge of the next estimation step. By iterating this procedure, the standard deviation of the Gaussian distribution quantifying our ignorance about A would decrease successively as $\Delta_0 > \Delta_1 > \Delta_2 > \cdots$. The iteration is stopped at the K-th step when the desired standard deviation Δ_{desire} is achieved: $\Delta_K \leq \Delta_{\text{desire}}$. Below, we describe the above estimation procedures in more detail.

Gaining knowledge about A from measurements

In the k-th estimation step ($k = 1, 2, \cdots$), the prior knowledge about the hyperfine interaction strength A is quantified by the Gaussian distribution $N(A_{k-1},\Delta_{k-1})$. Suppose that τ_k has been properly chosen (to be discussed shortly). By running the circuit $M(\tau_k)$ for a relatively large number N_k ($\gtrsim 100$) of times, we obtain an estimator Z_k of $\langle\hat{Z}\rangle_k \equiv Q(\tau_k)\cos(A\tau_k) + O(\eta^2)$ with a standard deviation $\zeta_k = 1/\sqrt{N_k}$. This knowledge tells us that $\langle\hat{Z}\rangle_k$ obeys the Gaussian distribution $\mathcal{N}(Z_k,\zeta_k)$. We need to convert this distribution of $\langle\hat{Z}\rangle_k$ to a distribution of A. For a general τ_k, the relation between $\langle\hat{Z}\rangle_k$ and A is nonlinear and the conversion from $\langle\hat{Z}\rangle_k$ to A results in a non-Gaussian distribution of A, with a characteristic width

$$\frac{\zeta_k}{|\partial\langle\hat{Z}\rangle_k/\partial A|} = \frac{\zeta_k}{Q(\tau_k)\tau_k|\sin(A\tau_k)|}.$$

Now we determine τ_k according to two requirements:

1. The distribution of A should be Gaussian (i.e., the relation between $\langle\hat{Z}\rangle_k$ and A should be linear), so that analytical results can be obtained. Based on our prior knowledge $\mathcal{N}(A_{k-1}, \Delta_{k-1})$ about A, the conditions $A_{k-1}\tau_k = \pi/2 + 2\pi \times$ integer and $\Delta_{k-1}\tau_k \ll 1$ enable the Taylor expansion $\langle\hat{Z}\rangle_k = (A_{k-1} - A)Q(\tau_k)\tau_k + \delta_k + O(\eta^2)$ with $\delta_k \approx Q(\tau_k)(\Delta_{k-1}\tau_k)^3/6$. For $\delta_k, O(\eta^2) \ll \zeta_k, |\langle\hat{Z}\rangle_k|$, the correction terms $\delta_k + O(\eta^2)$ can be safely dropped, so that the relation between $\langle\hat{Z}\rangle_k$ and A becomes linear and the distribution of A becomes Gaussian $\mathcal{N}(\bar{A}_k, \bar{\Delta}_k)$ with

$$\bar{A}_k = A_{k-1} - \frac{Z_k}{Q(\tau_k)\tau_k}, \tag{4.24a}$$

$$\bar{\Delta}_k = \frac{\zeta_k}{Q(\tau_k)\tau_k} = \frac{1}{Q(\tau_k)\tau_k\sqrt{N_k}}. \tag{4.24b}$$

   The distribution $\mathcal{N}(\bar{A}_k, \bar{\Delta}_k)$ of A tells us, with a 95% confidence, that A lies in the interval $[\bar{A}_k - 1.96\bar{\Delta}_k, \bar{A}_k + 1.96\bar{\Delta}_k]$.

2. For maximal precision of the estimation, the standard deviation $\bar{\Delta}_k$ should be minimized, i.e., $Q(\tau_k)\tau_k$ should be maximized.

Eq. (4.24b) shows that the standard deviation $\bar{\Delta}_k$ of the measurement of A is equal to the standard deviation $\zeta_k = 1/\sqrt{N_k}$ of the measurement of $\langle\hat{Z}\rangle_k$ divided by $Q(\tau_k)\tau_k$:

- For $Q(\tau_k) = 1$ (i.e., no errors), the standard deviation $\bar{\Delta}_k$ is reduced upon the increase of τ_k, which can be interpreted as a repetition of the circuit operations (as enclosed in the dashed box in Fig. 4.9) before the measurement is made. This is equivalent to a multiround protocol suggested by Giovannetti *et al*. [33]. Therefore, the dependence $\bar{\Delta}_k \propto 1/\tau_k$ implies the QML.

- The standard deviation $\bar{\Delta}_k$ is reduced upon the increase of N_k. The dependence $\bar{\Delta}_k \propto 1/\sqrt{N_k}$ implies the SQL.

In summary, for optimal performance, we should first choose ζ_k (or equivalently N_k) subjected to the constraint

$$O(\eta^2) \ll \zeta_k \ll 1 \tag{4.25}$$

and then choose τ_k to maximize $Q(\tau_k)\tau_k$, subjected to the constraints

$$A_{k-1}\tau_k = \frac{\pi}{2} + 2m_k\pi, \tag{4.26a}$$

$$\frac{(\Delta_{k-1}\tau_k)^3}{6} \ll \zeta_k, \tag{4.26b}$$

$$Q(\tau_k)\Delta_{k-1}\tau_k \gg O(\eta^2), \tag{4.26c}$$

where $m_k \in \mathbb{Z}$ and $O(\eta^2) \sim 10^{-6}$ for $B = 0.2$ T. The constraint $\zeta_k \ll 1$ ensures the validity of our Gaussian distribution assumption for $\langle\hat{Z}\rangle_k$, while other constraints ensure the validity of the formula $\langle\hat{Z}\rangle_k \approx (A_{k-1} - A)Q(\tau_k)\tau_k$. The error of the linear expansion can be dropped if $\delta_k \ll \zeta_k$, which gives Eq. (4.26b) with $Q(\tau_k) \leq 1$. Eq. (4.26c) denotes the condition to drop $O(\eta^2)$ in $\langle\hat{Z}\rangle_k$. Note that the constraints [Eqs. (4.26)] on τ_k have no solution under certain conditions, e.g., when $Q(\tau_k) \lesssim O(\eta^2)/(\zeta_k)^{1/3}$. Therefore, for more flexible choice of τ_k, the standard deviation ζ_k of the measurement of $\langle\hat{Z}\rangle_k$ should not be too small.

Combining new knowledge with prior knowledge

In the previous subsection, we have spent N_k runs of the circuit $M(\tau_k)$ to obtain the new knowledge $\mathcal{N}(\bar{A}_k, \bar{\Delta}_k)$ about A. To make use of the resources spent in obtaining the prior knowledge $\mathcal{N}(A_{k-1}, \Delta_{k-1})$, we use the Bayesian inference, which combines our new knowledge $\mathcal{N}(\bar{A}_k, \bar{\Delta}_k)$ with the prior knowledge $\mathcal{N}(A_{k-1}, \Delta_{k-1})$. It gives an updated Gaussian distribution $\mathcal{N}(A_k, \Delta_k)$ centered at

$$A_k = \frac{A_{k-1}/\Delta_{k-1}^2 + \bar{A}_k/\bar{\Delta}_k^2}{1/\Delta_{k-1}^2 + 1/\bar{\Delta}_k^2} \tag{4.27a}$$

(which is a weighted average of A_{k-1} with weight $1/\Delta_{k-1}^2$ and $\bar{A}_k$ with weight $1/\bar{\Delta}_k^2$) with a standard deviation Δ_k determined by

$$\frac{1}{\Delta_k^2} = \frac{1}{\Delta_{k-1}^2} + \frac{1}{\bar{\Delta}_k^2}. \tag{4.27b}$$

This updated knowledge $\mathcal{N}(A_k, \Delta_k)$ tells us, with a 95% confidence, that A lies in the refined interval $[A_k - 1.96\Delta_k, A_k + 1.96\Delta_k]$. The inequalities $\Delta_k < \Delta_{k-1}$ and $\Delta_k < \bar{\Delta}_k$ reveal that the combination of $\mathcal{N}(A_{k-1}, \Delta_{k-1})$ and $\mathcal{N}(\bar{A}_k, \bar{\Delta}_k)$ gives us a more precise knowledge about A.

For very accurate measurement compared with the prior knowledge, i.e., $\bar{\Delta}_k \ll \Delta_{k-1}$, Eqs. (4.27a) and (4.27b) reduce to $A_k \approx \bar{A}_k$ and $\Delta_k \approx \bar{\Delta}_k$, suggesting that the updated knowledge is dominated by the measurement. By contrast, for inaccurate measurement $\bar{\Delta}_k \gg \Delta_{k-1}$, the updated knowledge $A_k \approx A_{k-1}$ and $\Delta_k \approx \Delta_{k-1}$ is dominated by the prior knowledge.

4.6.2 Ideal case: approaching quantum metrology limit

In this subsection, we demonstrates the QML scaling of our estimation protocol in the ideal case, i.e., in the absence of any errors (e.g., operation errors, relaxation, and decoherence). For simplicity, we assume that in each estimation step, we run the quantum circuit for the same number of times $N_1 = N_2 = \cdots \equiv N$, corresponding to $\zeta_1 = \zeta_2 = \cdots \equiv \zeta \equiv 1/\sqrt{N}$.

Up to the K-th estimation step, the total duration of the our estimation process (identified as the total amount of resources spent) is

$$R_K = N \sum_{k=1}^{K} 2\tau_k \equiv N\tau_K^{\text{tot}}.$$

To see the scaling of the precision $1/\Delta_K^2$ with respect to R_K, we take the first estimation step as a reference. Further, we take $\Delta_0 = \infty$ to exclude the contribution from the prior knowledge $\mathcal{N}(A_0, \Delta_0)$, so that all our knowledge about A comes from the resources R_K spent in our protocol. Then, the QML limit $\Delta_{K,\text{QML}}$ is defined by $\Delta_{K,\text{QML}}/\Delta_1 \equiv 1/(R_K/R_1)$, while the SQL limit $\Delta_{K,\text{SQL}}$ is defined by $\Delta_{K,\text{SQL}}/\Delta_1 \equiv 1/\sqrt{R_K/R_1}$. Using $R_1 = 2N\tau_1$ and $\Delta_1 = 1/(\tau_1\sqrt{N})$, we obtain

$$\frac{1}{\Delta_{K,\text{QML}}^2} = N\left(\sum_{k=1}^{K} \tau_k\right)^2, \tag{4.28}$$

$$\frac{1}{\Delta_{K,\text{SQL}}^2} = N\tau_1 \sum_{k=1}^{K} \tau_k, \tag{4.29}$$

$$\frac{1}{\Delta_K^2} = N \sum_{k=1}^{K} \tau_k^2.$$

First, we compare Δ_K with the QML limit $\Delta_{K,\text{QML}}$ and the SQL limit $\Delta_{K,\text{SQL}}$ and discuss the condition for approaching the QML:

1. The inequality $\Delta_K > \Delta_{K,\mathrm{QML}}$ can be readily verified. This manifests the QML precision $1/\Delta_{K,\mathrm{QML}}^2$ as the upper precision bound. To achieve the QML, $\{\tau_k\}$ should satisfy $\tau_K \gg \tau_{K-1} \gg \cdots \gg \tau_1$, so that the total amount of resources is dominated by the final estimation step and hence $\Delta_K \approx \Delta_{K,\mathrm{QML}} \approx 1/(\tau_K \sqrt{N})$. This condition is equivalent to a dramatic reduction of the standard deviation of the measurement for each successive estimation step: $\bar{\Delta}_K \ll \bar{\Delta}_{K-1} \ll \cdots \ll \bar{\Delta}_1$. This ensures that in each estimation step (say, the k-th step), the standard deviation of the estimation, $\Delta_k \approx \bar{\Delta}_k \approx 1/(\tau_k \sqrt{N})$, is dominated by the standard deviation $\bar{\Delta}_k$ of the measurement instead of the standard deviation $\Delta_{k-1} \approx \bar{\Delta}_{k-1}$ of the prior knowledge [cf. Eq. (4.27b)]. The condition $\tau_K \gg \tau_{K-1} \gg \cdots \gg \tau_1$ is also equivalent to

$$\Delta_{k-1}\tau_k \gg \zeta, \tag{4.30}$$

since $\Delta_{k-1}\tau_k \approx \bar{\Delta}_{k-1}\tau_k = (\tau_k/\tau_{k-1})\zeta$.

2. For $\tau_1 = \tau_2 = \cdots = \tau_K$, the precision $1/\Delta_K^2 = NK\tau_1^2$ coincides with the SQL precision $1/\Delta_{K,\mathrm{SQL}}^2$ since in this case our protocol reduces to simple repetition of the same quantum circuit $M(\tau_1)$.

Then we give the best choice $\{\tau_k^{\mathrm{ideal}}\}$ satisfying the QML condition Eq. (4.30) for the ideal case according to the description in Sec. 4.6.1. We choose $\{\tau_k^{\mathrm{ideal}}\}$ by taking the largest m_k such that $\Delta_{k-1}\tau_k \approx c$ at every step, where c is a constant satisfying $c \gg \zeta$ and $c^3 \ll 6\zeta$. Then $\{\tau_k^{\mathrm{ideal}}\}$ automatically satisfies the QML condition Eq. (4.30) and the linear expansion condition Eq. (4.26b). From $\Delta_{k-1}\tau_k \approx c$, we have $\Delta_k \approx \bar{\Delta}_k \approx (\zeta/c)^k\Delta_0$, i.e., the standard deviation $\Delta_k \approx \bar{\Delta}_k$ is dramatically reduced by each successive estimation step. We also have $\tau_k^{\mathrm{ideal}} \approx (c/\zeta)^k\tau_0$ (with τ_0 defined through $\Delta_0 \equiv \zeta/\tau_0$), i.e., an exponential increase of τ_k^{ideal} with k. Note that, for $B = 0.2$ T, we have $O(\eta^2) \sim 10^{-6}$. Therefore ζ can be as small as $\sim 10^{-5}$.

Finally we provide a numerical simulation for the estimation process. The parameters for the simulation are $A = 3.06$ MHz, $B = 0.2$ T, $N = 1000$, corresponding to $\zeta \approx 0.03$. We take $c = 0.2$, which satisfies $c \gg \zeta$ and $c^3 \ll 6\zeta$. The prior knowledge is $A_0 = 3.03$ MHz with a standard deviation $\Delta_0 = 0.03$ MHz, which has been reported by a previous experiment [23]. Each controlled nuclear spin π rotation uses a 1-μs square pulse with the Rabi frequency $\Omega = 500$ kHz. The electron spin rotations are regarded as

Table 4.1: A sample numerical simulation result for the estimation of the hyperfine interaction A in the NV center, without any errors or decays of the system. $k = 0$ denotes the prior information for the first estimation step. $A = 3.06$ MHz is used in the simulation.

k	τ_k (μs)	A_k (MHz)	Δ_k (MHz)
0	0	3.03	0.03
1	1.07	3.058 7	0.004 6
2	6.95	3.059 48	0.000 72
3	44.52	3.060 17	0.000 11
4	285.05	3.060 022	0.000 017
5	1,825.24	3.059 996 9	0.000 002 7

instantaneous, as mentioned at the end of Sec. 4.5.2. In Fig. 4.10, the proximity of Δ_K (circles) to $\Delta_{K,\mathrm{QML}}$ (solid line) confirms the QML scaling of the estimation.

4.6.3 Realistic case: surpassing standard quantum limit

In this subsection, we take into account the nuclear spin rotation error and electron spin decoherence and discuss the optimal choice of $\{\tau_k\}$ and the resulting precision

$$\frac{1}{\Delta_K^2} = N \sum_{k=1}^{K} [Q(\tau_k)\tau_k]^2$$

of the estimation, derived from Eq. (4.24b) and (4.27b):

- Nuclear spin rotation error $Q(\tau) = 1 - \varepsilon^2 \equiv Q$. This error is equivalent to an increase of ζ to $\tilde{\zeta} \equiv \zeta/Q$. Then QML condition Eq. (4.30) becomes $\Delta_{k-1}\tau_k \gg \tilde{\zeta}$. For a general Q that is not too small (i.e., $1 \geq Q \gg \zeta$), the conclusion in the ideal case remains valid with $\zeta \to \tilde{\zeta}$, i.e., $\{\tau_k\}$ is chosen as $\tau_k \approx (c/\tilde{\zeta})^k(\tau_0/Q)$, where c is a constant subjected to $c \gg \tilde{\Delta}_Z$ and $c^3 \ll 6\tilde{\Delta}_Z$. In the simulation, we consider a typical error $\varepsilon = 0.1$ (corresponding to $\sim 3\%$ error in the rotation angle). Then we have $Q \approx 1$, and this allows us to set $c = 0.2$, the same value with the ideal case. As a result, we can choose $\tau_k \approx \tau_k^{\mathrm{ideal}}$ and Δ_K is nearly the same as the ideal case. Therefore, the QML scaling is preserved for the realistic nuclear

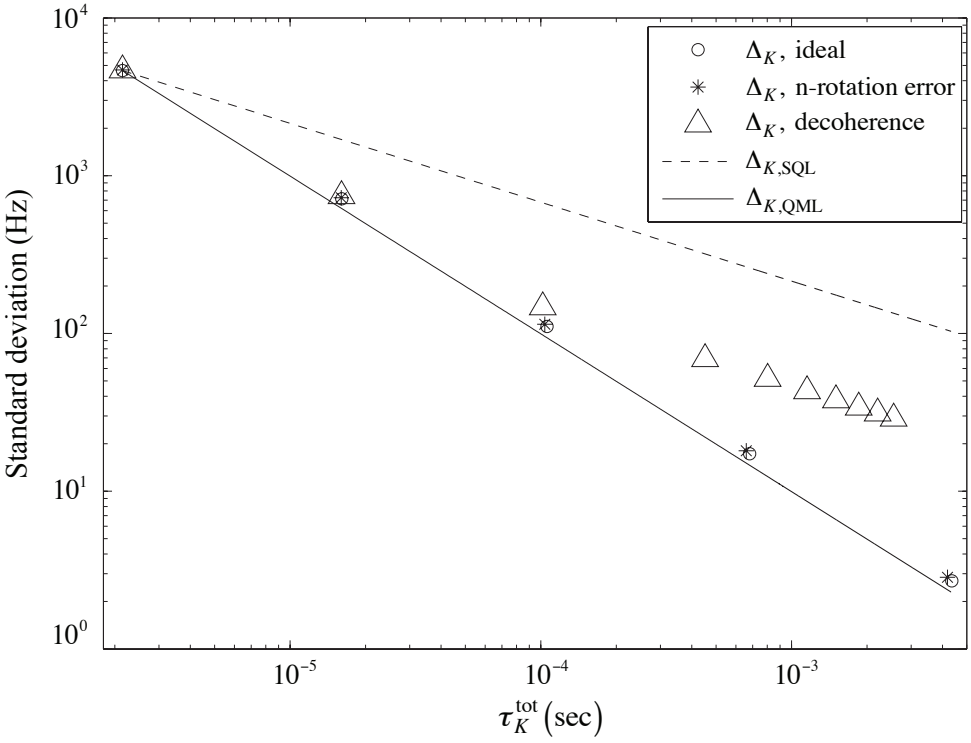

Figure 4.10: Comparison of the standard deviation Δ_K of our protocol with the QML limit $\Delta_{K,\rm QML}$ (solid line) and the SQL limit $\Delta_{K,\rm SQL}$ (dashed line). How to choose the optimum τ_k is explained in the main text. $\Delta_\epsilon = 0.1$ (Q=0.99) is used for the nuclear spin rotation error. For the electron spin decoherence, we use $T_2^e = 350\ \mu$s as the electron spin coherence time.

spin rotation error, as confirmed by the nearly complete coincidence between Δ_K (stars) and $\Delta_{K,\rm QML}$ (solid line) in Fig. 4.10.

- Electron spin decohence $Q(\tau) = e^{-2\tau/T_2^e}$. According to Sec. 4.6.1, we should choose τ_k to maximize $Q(\tau_k)\tau_k$, subjected to the constraints in Eqs. (4.26). We use $\Delta_{k-1}\tau_k \approx c = 0.2$ in the simulation. In the presence of the electron spin decoherence, $Q(\tau)$ decreases as τ increases. Thus the QML condition $c \gg \zeta/Q(\tau_k)$ is no longer valid at some point. This is why Δ_k starts to deviate from the QML line at $k = 3$ in Fig. 4.10. Note that the estimation of $k = 3$ still surpasses the SQL. The maximum of $Q(\tau)\tau$ occurs at $\tau = T_2^e/2$, meaning that the standard deviation $\bar{\Delta}_k$ of the quantum circuit $M(\tau_k)$ is the smallest when $\tau_k \approx T_2^e/2$. Further increase of τ_k makes the precision of $M(\tau_k)$ worse. Once τ_k reaches $\tau_k \approx T_2^e/2$ at $k = k_c$, the

Table 4.2: A sample numerical simulation result for the estimation of the hyperfine interaction A in the NV center, with the electron spin decoherence error. $k = 0$ denotes the prior information for the first estimation step. $A = 3.06$ MHz is used in the simulation. We have $\tau_4 = T_2^e/2$ at the fourth estimation.

k	τ_k (μs)	A_k (MHz)	Δ_k (MHz)
0	0	3.03	0.03
1	1.07	3.054 8	0.004 7
2	6.96	3.060 34	0.000 74
3	42.89	3.060 01	0.000 15
4	175.24	3.060 049	0.000 069
5	175.24	3.060 041	0.000 052
6	175.24	3.060 044	0.000 043

estimation for $k > k_c$ is performed with $\tau_k = \tau_{k_c}$. Therefore, for $K = k_c + \tilde{K}$, further estimation steps beyond k_c (i.e., $k = k_c + 1, \cdots, k_c + \tilde{K}$) increases the precision $1/\Delta_K^2$ by the SQL trend:

$$\frac{1}{\Delta_{k_c+\tilde{K}}^2} - \frac{1}{\Delta_{k_c}^2} \approx N\tilde{K}(T_2^e/2)^2.$$

For $T_2^e = 350\ \mu$s, we have $k_c = 4$. Fig. 4.10 shows that Δ_K surpasses the SQL for $K < 4$, while it decreases parallel to the SQL for $K \geq 4$.

4.7 Conclusions

We have proposed an efficient quantum measurement protocol to estimate the hyperfine interaction between the electron spin and the ^{15}N nuclear spin in the NV center. The essential idea of our protocol is the combination of the DQC1 parameter estimation [6] with the spin-echo technique. The spin echo eliminates the independent dynamics of the electron spin and the nuclear spin in the DQC1 model, but keeps the dynamics due to their interactions, whose strength is to be estimated. This protocol does not require the preparation of the nuclear spin state. We quantify the resources R as the total duration $\sum \tau$ of the estimation process. In the absence of any errors, the precision $1/\Delta^2$ (with Δ

being the standard deviation) of the estimation approaches the quantum metrology limit (QML) $1/\Delta^2_{\mathrm{QML}} = O(R^2)$. This QML scaling is robust against the typical nuclear spin rotation error in realistic experimental conditions. In the presence of electron spin decoherence, the precision $1/\Delta^2$ keeps its QML scaling when $\tau \ll T_2^e/2$. Once τ becomes close to T_2^e further estimation steps increase the precision $1/\Delta^2$ according to the scaling $1/\Delta^2_{\mathrm{SQL}} = O(R)$ of the standard quantum limit (SQL). Due to the QML scaling in the initial stage, the overall precision still surpasses the SQL. We expect that this method can be applied to other solid state systems such as quantum dots or cold atoms to measure the interaction between two spins.

4.8 Appendix

4.8.1 Extended two-qubit DQC1 model

Here we consider an arbitrary target qubit state in the two-qubit DQC1 model.

The circuit diagram of the two-qubit DQC1 model with a general target qubit state ρ_{tar} is illustrated in Fig. 4.11. An arbitrary initial state of the mixed-state target qubit can be written as

$$\hat{\rho}_{\mathrm{tar}} = \frac{\hat{I} + \vec{q}\cdot\vec{\sigma}}{2},$$

with the polarization $\left|\vec{q}\right| \leq 1$. An arbitrary unitary operation is expressed as

$$\hat{U} = e^{i\varphi}\exp\left(-i\frac{\hat{n}\cdot\vec{\sigma}\phi}{2}\right). \tag{4.31}$$

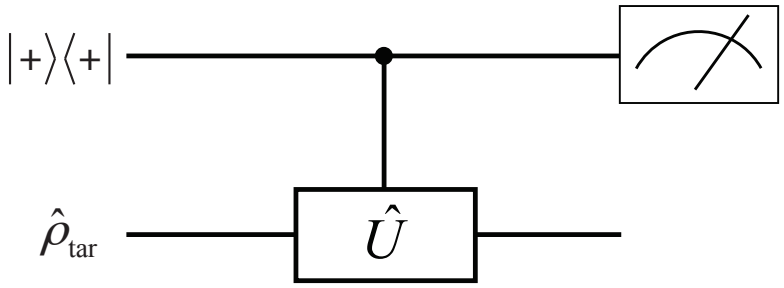

Figure 4.11: Two-qubit DQC1 model with one control qubit in the pure state $|+\rangle \equiv (|0\rangle + |1\rangle)/\sqrt{2}$ and one target qubit in an arbitrary state ρ_{tar}.

After the controlled operation, we have the output state of the system

$$\hat{\rho}_o = \frac{1}{2}\left[|0\rangle\langle 0| \otimes \hat{\rho}_{\text{tar}} + |0\rangle\langle 1| \otimes \hat{\rho}_{\text{tar}}\hat{U}^\dagger + |1\rangle\langle 0| \otimes \hat{U}\hat{\rho}_{\text{tar}} + |1\rangle\langle 1| \otimes \hat{U}\hat{\rho}_{\text{tar}}\hat{U}^\dagger\right]. \tag{4.32}$$

The reduced state of the control qubit is

$$\hat{\rho}_o^c = \frac{1}{2}\left[|0\rangle\langle 0| + \text{Tr}[\hat{\rho}_{\text{tar}}\hat{U}^\dagger]\,|0\rangle\langle 1| + \text{Tr}[\hat{U}\hat{\rho}_{\text{tar}}]\,|1\rangle\langle 0| + \text{Tr}[\hat{U}\hat{\rho}_{\text{tar}}\hat{U}^\dagger]\,|1\rangle\langle 1|\right]. \tag{4.33}$$

We are interested in the coherence of the control qubit. $\hat{U}\hat{\rho}_{\text{tar}}$ is further calculated to

$$\begin{aligned}\hat{U}\hat{\rho}_{\text{tar}} &= e^{i\varphi}\left[\cos\left(\frac{\phi}{2}\right) - i\hat{n}\cdot\vec{\sigma}\sin\left(\frac{\phi}{2}\right)\right]\frac{\hat{I}+\vec{q}\cdot\vec{\sigma}}{2} \\ &= \frac{e^{i\varphi}}{2}\left[\cos\left(\frac{\phi}{2}\right)\left(\hat{I}+\vec{q}\cdot\vec{\sigma}\right) - i\sin\left(\frac{\phi}{2}\right)(\hat{n}\cdot\vec{\sigma} + \hat{n}\cdot\vec{q} + i\,(\hat{n}\times\vec{q})\cdot\vec{\sigma})\right].\end{aligned} \tag{4.34}$$

From $\text{Tr}[\vec{\sigma}] = 0$, we have

$$\text{Tr}[\hat{U}\hat{\rho}_{\text{tar}}] = e^{i\varphi}\left[\cos\left(\frac{\phi}{2}\right) - i\hat{n}\cdot\vec{q}\sin\left(\frac{\phi}{2}\right)\right], \tag{4.35}$$

$$\text{Tr}[\hat{\rho}_{\text{tar}}\hat{U}^\dagger] = e^{-i\varphi}\left[\cos\left(\frac{\phi}{2}\right) + i\hat{n}\cdot\vec{q}\sin\left(\frac{\phi}{2}\right)\right]. \tag{4.36}$$

If we choose an measurement operator as $\hat{M} \equiv \cos\varphi\hat{X} + \sin\varphi\hat{Y}$ in the DQC1 model, then the average value of M is

$$\langle\hat{M}\rangle = \text{Tr}[\hat{\rho}_c\hat{M}] = \cos\phi. \tag{4.37}$$

This result is independent on $\vec{q}$. In other words, for a given $\hat{U}$, there is a certain direction of the measurement of which the average value is independent on the initial state of the target qubit. We use this property to construct a parameter estimation algorithm for the NV center in the next section.

4.8.2 Calculation of $\langle\hat{X}\rangle$ of the DQC1 model

Here we provide the calculation for $\langle\hat{X}\rangle$ under the Hamiltonian $\hat{H} = \hat{H}_0 + \hat{H}_{\text{mix}}$ discussed in Sec. 4.4.2. $\hat{H}_{\text{mix}}$ is treated as a perturbation. The initial state of the NV center is $\hat{\rho}_i = |+\rangle\langle+| \otimes \hat{\rho}_{\text{neq}}$, where $\hat{\rho}_{\text{neq}} = (\hat{I} + q_z\hat{\sigma}_z)/2$ denotes a partially polarized qubit. We use the matrix representation with a basis $[|0,\uparrow\rangle, |0,\downarrow\rangle, |1,\uparrow\rangle, |1,\downarrow\rangle]$. $\hat{H}_0$ is

represented by

$$\hat{H}_0 \doteq \begin{bmatrix} \frac{g_N\mu_N B\hat{\sigma}_z}{2} & 0 & 0 & 0 \\ 0 & -\frac{g_N\mu_N B\hat{\sigma}_z}{2} & 0 & 0 \\ 0 & 0 & D' - \frac{A}{2} + \frac{g_N\mu_N B\hat{\sigma}_z}{2} & 0 \\ 0 & 0 & 0 & D' + \frac{A}{2} - \frac{g_N\mu_N B\hat{\sigma}_z}{2} \end{bmatrix}$$
$$= \begin{bmatrix} E_{|0,\uparrow\rangle} & 0 & 0 & 0 \\ 0 & E_{|0,\downarrow\rangle} & 0 & 0 \\ 0 & 0 & E_{|1,\uparrow\rangle} & 0 \\ 0 & 0 & 0 & E_{|1,\downarrow\rangle} \end{bmatrix}, \tag{4.38}$$

and $\hat{H}$ is written as

$$\hat{H} \doteq \begin{bmatrix} E_{|0,\uparrow\rangle} & 0 & 0 & 0 \\ 0 & E_{|0,\downarrow\rangle} & \frac{A_\perp}{\sqrt{2}} & 0 \\ 0 & \frac{A_\perp}{\sqrt{2}} & E_{|1,\uparrow\rangle} & 0 \\ 0 & 0 & 0 & E_{|1,\downarrow\rangle} \end{bmatrix}$$
$$= \hat{V}\hat{\Lambda}\hat{V}^\dagger, \tag{4.39}$$

where

$$\hat{\Lambda} \doteq \begin{bmatrix} E_{|0,\uparrow\rangle} & 0 & 0 & 0 \\ 0 & \lambda_{|0,\downarrow\rangle} & 0 & 0 \\ 0 & 0 & \lambda_{|1,\uparrow\rangle} & 0 \\ 0 & 0 & 0 & E_{|1,\downarrow\rangle} \end{bmatrix} \tag{4.40}$$

is a diagonal matrix with the eigenvalues of $\hat{H}$ and

$$\hat{V} \doteq \begin{bmatrix} 1 & 0 & 0 & 0 \\ 0 & 1 - \frac{\eta^2}{2} & \eta & 0 \\ 0 & -\eta & 1 - \frac{\eta^2}{2} & 0 \\ 0 & 0 & 0 & 1 \end{bmatrix} \tag{4.41}$$

is a matrix composed of the eigenvectors of $\hat{H}$ in its columns up to the second order in $\eta \equiv A_\perp/[\sqrt{2}(D' + g_N\mu_N B - A/2)]$. The corresponding evolution operator is represented

up to the second order in η by

$$\hat{U}(\tau) = e^{-i\hat{H}\tau} = \hat{V}e^{-i\hat{\Lambda}\tau}\hat{V}^\dagger$$
$$= \begin{bmatrix} e^{-iE_{|0,\uparrow\rangle}\tau} & 0 & 0 & 0 \\ 0 & (1-\eta^2)e^{-i\lambda_{|0,\downarrow\rangle}\tau} + \eta^2 e^{-i\lambda_{|1,\uparrow\rangle}\tau} & \eta\left(e^{-i\lambda_{|1,\downarrow\rangle}\tau} - e^{-i\lambda_{|0,\downarrow\rangle}\tau}\right) & 0 \\ 0 & \eta\left(e^{-i\lambda_{|1,\uparrow\rangle}\tau} - e^{-i\lambda_{|0,\downarrow\rangle}\tau}\right) & \eta^2 e^{-i\lambda_{|0,\downarrow\rangle}\tau} + (1-\eta^2)e^{-i\lambda_{|1,\uparrow\rangle}\tau} & 0 \\ 0 & 0 & 0 & e^{-iE_{|1,\downarrow\rangle}\tau} \end{bmatrix}.$$

After the evolution, the output state of the system is

$$\hat{\rho}_o = \hat{U}\hat{\rho}_i\hat{U}^\dagger = \frac{1}{2}\begin{bmatrix} \hat{\rho}^e_{00} & \hat{\rho}^e_{01} \\ \hat{\rho}^e_{10} & \hat{\rho}^e_{11} \end{bmatrix},$$

where $\{\hat{\rho}^e_{jk}\}$ is a 2×2 matrix and $\hat{\rho}^e_{01} = (\hat{\rho}^e_{10})^\dagger$. Since we are interested in the coherence of the electron spin, we need to compute $\mathrm{Tr}[\hat{\rho}^e_{10}]$ only, which is given by

$$\mathrm{Tr}[\hat{\rho}^e_{10}] = \frac{1+q_z}{2}e^{-i\tilde{\omega}^e_\uparrow\tau} + \frac{1-q_z}{2}e^{-i\tilde{\omega}^e_\downarrow\tau} + O(\eta^2),$$

where $\tilde{\omega}^e_\uparrow = \lambda_{|1,\uparrow\rangle} - E_{|0,\uparrow\rangle}$ ($\tilde{\omega}^e_\downarrow = E_{|1,\downarrow\rangle} - \lambda_{|0,\downarrow\rangle}$) is a transition frequency of the electron spin as described in Sec. 4.4.2. Note that the first order in η does not appear in $\mathrm{Tr}[\rho^e_{10}]$. Therefore, we have $\langle\hat{X}\rangle$ as

$$\begin{aligned}\langle\hat{X}\rangle &= \frac{1}{2}\left(\mathrm{Tr}[\hat{\rho}^e_{10}] + \mathrm{Tr}[\hat{\rho}^e_{01}]\right) + O(\eta^2) \\ &= \frac{1+q_z}{2}\cos(\tilde{\omega}^e_\uparrow) + \frac{1-q_z}{2}\cos(\tilde{\omega}^e_\downarrow) + O(\eta^2) \\ &= \cos[(D'+\delta)\tau]\cos\left(\frac{A}{2}\tau\right) + q_z\sin[(D'+\delta)\tau]\sin\left(\frac{A}{2}\tau\right) + O(\eta^2),\end{aligned}$$

where $\delta = \eta A_\perp/2 + O(\eta^2 A_\perp)$ is an energy shift by the perturbed Hamiltonian $\hat{H}_{\mathrm{mix}}$.

4.8.3 Calculation of $\langle\hat{X}\rangle$ of the spin-echo DQC1 circuit

Here we calculate $\langle\hat{X}\rangle$ of the spin-echo DQC1 circuit discussed in Sec. 4.5.1. The composite evolution $\hat{U}_{\mathrm{com}}$ in Eq. (4.20) governs the dynamics of the system. Using

Eq. (4.21), $\hat{H}'$ is given by

$$\begin{aligned}\hat{H}' &= \hat{H}'_0 + \hat{H}_{\text{mix}} \\ &= \begin{bmatrix} E_{|1,\downarrow\rangle} & 0 & 0 & 0 \\ 0 & E_{|1,\uparrow\rangle} & \frac{A_\perp}{\sqrt{2}} & 0 \\ 0 & \frac{A_\perp}{\sqrt{2}} & E_{|0,\downarrow\rangle} & 0 \\ 0 & 0 & 0 & E_{|0,\uparrow\rangle} \end{bmatrix} \\ &= \hat{V}^\dagger \hat{\Lambda}' \hat{V} \end{aligned} \tag{4.42}$$

with a basis $[|0,\uparrow\rangle, |0,\downarrow\rangle, |1,\uparrow\rangle, |1,\downarrow\rangle]$, where

$$\hat{\Lambda}' \doteq \begin{bmatrix} E_{|1,\downarrow\rangle} & 0 & 0 & 0 \\ 0 & \lambda_{|1,\uparrow\rangle} & 0 & 0 \\ 0 & 0 & \lambda_{|0,\downarrow\rangle} & 0 \\ 0 & 0 & 0 & E_{|0,\uparrow\rangle} \end{bmatrix}.$$

The corresponding evolution operator of $\hat{H}'$ is

$$\begin{aligned} e^{-i\hat{H}'\tau} &= \hat{V}^\dagger e^{-i\hat{\Lambda}'\tau} \hat{V} \\ &= \begin{bmatrix} e^{-iE_{|1,\downarrow\rangle}\tau} & 0 & 0 & 0 \\ 0 & (1-\eta^2)e^{-i\lambda_{|1,\uparrow\rangle}\tau} + \eta^2 e^{-i\lambda_{|0,\downarrow\rangle}\tau} & \eta\left(e^{-i\lambda_{|1,\downarrow\rangle}\tau} - e^{-i\lambda_{|0,\downarrow\rangle}\tau}\right) & 0 \\ 0 & \eta\left(e^{-i\lambda_{|1,\uparrow\rangle}\tau} - e^{-i\lambda_{|0,\downarrow\rangle}\tau}\right) & \eta^2 e^{-i\lambda_{|1,\uparrow\rangle}\tau} + (1-\eta^2)e^{-i\lambda_{|0,\downarrow\rangle}\tau} & 0 \\ 0 & 0 & 0 & e^{-iE_{|0,\uparrow\rangle}\tau} \end{bmatrix}. \end{aligned}$$

Therefore, the composite evolution $\hat{U}_{\text{com}}$ becomes

$$\begin{aligned} \hat{U}_{\text{com}} =& \hat{R}^e_y(\pi)\hat{R}^n_y(\pi)\left(e^{-i(\hat{\sigma}_y\hat{Y}\hat{H}\hat{Y}\hat{\sigma}_y)\tau} e^{-i\hat{H}\tau}\right) \\ =& \hat{R}^e_y(\pi)\hat{R}^n_y(\pi)\begin{bmatrix} e^{-i(E_{|0,\uparrow\rangle}+E_{|1,\downarrow\rangle})\tau} & 0 & 0 & 0 \\ 0 & e^{-i(\lambda_{|0,\downarrow\rangle}+\lambda_{|1,\uparrow\rangle})\tau} & O(\eta) & 0 \\ 0 & O(\eta) & e^{-i(\lambda_{|0,\downarrow\rangle}+\lambda_{|1,\uparrow\rangle})\tau} & 0 \\ 0 & 0 & 0 & e^{-i(E_{|0,\uparrow\rangle}+E_{|1,\downarrow\rangle})\tau} \end{bmatrix} \\ &+ \hat{R}^e_y(\pi)\hat{R}^n_y(\pi)O(\eta^2) \\ =& \hat{R}^e_y(\pi)\hat{R}^n_y(\pi)\left[e^{-iA\tau\hat{\sigma}_z/2} e^{-i\hat{H}_{\text{echo}}\tau} + O(\eta)\left(|0,\downarrow\rangle\langle 1,\uparrow| + |1,\uparrow\rangle\langle 0,\downarrow|\right)\right] + O(\eta^2), \end{aligned} \tag{4.43}$$

where $\hat{H}_{\text{echo}} = |1\rangle\langle 1| \otimes (-A\hat{\sigma}_z)$. In particular, all higher order energy shifts as well as the second order in $A_\perp$ by the perturbed Hamiltonian $\hat{H}_{\text{mix}}$ are completely erased since $\lambda_{|0,\downarrow\rangle} + \lambda_{|1,\uparrow\rangle} = E_{|0,\downarrow\rangle} + E_{|1,\uparrow\rangle} = -A/2$.

We use $\hat{\rho}_i = |+\rangle\langle +| \otimes (\hat{I} + q_z\hat{\sigma}_z)/2$ as the initial state. After the composite evolution, the output state is

$$\hat{\rho}_o = \hat{U}_{\text{com}}\rho_i\hat{U}_{\text{com}}^\dagger.$$

$\langle\hat{X}\rangle$ can be obtained by

$$\langle\hat{X}\rangle = \text{Tr}\left[\hat{X}\hat{\rho}_o\right] = -\cos(A\tau) + O(\eta^2).$$

As long as the initial nuclear spin state has no off-diagonal elements, $O(\eta)$ of $\hat{U}_{\text{com}}$ in Eq. (4.43) does not appear in $\langle\hat{X}\rangle$.

4.8.4 Accounting for finite duration of controlled nuclear spin rotation

In this section, we assume that each of the two controlled nuclear spin π rotation in the quantum protocol (Fig. 4.9) is driven by a square π pulse with a duration $\tau_n \sim 1\ \mu$s and prove that inclusion of this finite duration amounts to a trivial renormalization $\tau \to \tau + \tau_n$ in Eq. (4.22).

In Fig. 4.9, the initial state $\hat{\rho}_{\text{i}} = |+\rangle\langle +| \otimes \hat{\rho}_{\text{neq}}$ is prepared at $t = -\tau - \tau_n$. The first free evolution $e^{-i\hat{H}\tau}$ occurs during $t \in [-\tau - \tau_n, -\tau_n]$, followed by a controlled nuclear spin π rotation during $t \in [-\tau_n, 0]$. A fast electron spin π rotation is applied at $t = 0$, another controlled nuclear spin π rotation during $t \in [0, \tau_n]$, and another free evolution $e^{-i\hat{H}\tau}$ during $t \in [\tau_n, \tau + \tau_n]$.

First we calculate the evolution operator driven by a square π pulse applied during $t \in [t_1, t_2]$, with a central frequency $\omega = A - g_N\mu_N B - \delta$ (where $+\delta$ is the energy correction to $|1,\uparrow\rangle$ by the off-diagonal hyperfine interaction) resonant with the transition $|1,\uparrow\rangle \to |1,\downarrow\rangle$. During this pulse, the Hamiltonian $\hat{H}(t) = \hat{H} + \hat{V}(t)$ of the electron-nuclear spin qubits acquires an additional term

$$\hat{V}(t) = \frac{i\Omega_R}{2}(e^{-i\omega t}|1,\downarrow\rangle\langle 1,\uparrow| - e^{i\omega t}|1,\uparrow\rangle\langle 1,\downarrow|),$$

with a constant Rabi frequency $\Omega_R = \pi/(t_2 - t_1)$. With the aid of the interaction picture $|\Psi_I(t)\rangle \equiv e^{i\hat{H}t}|\Psi(t)\rangle$, the evolution operator $\hat{U}_V(t_2, t_1)$ during $t \in [t_1, t_2]$ can be calculated straightforwardly as $\hat{U}_V(t_2, t_1) = e^{-i\hat{H}t_2}e^{-i\hat{H}_I(t_2-t_1)}e^{i\hat{H}t_1}$, where $\hat{H}_I(t) \equiv e^{i\hat{H}t}\hat{V}(t)e^{-i\hat{H}t}$. Similar to the discussions in Sec. 4.4.2, we have $\hat{H}_I(t) = (\Omega_R/2)\,|1\rangle\langle 1| \otimes \hat{\sigma}_y + O(\Omega_R\eta)$, where $\eta \sim 10^{-3}$ for the external magnetic field $B = 0.2$ T used in our estimation. Therefore, the evolution $e^{-i\hat{H}_I(t_2-t_1)} \approx \tilde{R}_y^n(\pi)$ coincides with the instantaneous controlled rotation and hence

$$\hat{U}_V(t_2, t_1) = e^{-i\hat{H}t_2}\tilde{R}_y^n(\pi)e^{i\hat{H}t_1}.$$

With the aid of this result, we can compute $\hat{U}_{\rm com}$ again

$$\begin{aligned}\hat{U}_{\rm com} &= e^{-i\hat{H}\tau}\hat{U}_V(\tau_n, 0)\hat{R}_y^e(\pi)\hat{U}_V(0, -\tau_n)e^{-i\hat{H}\tau} \\ &= e^{-i\hat{H}(\tau+\tau_n)}\tilde{R}_y^n(\pi)\hat{R}_y^e(\pi)\tilde{R}_y^n(\pi)e^{-i\hat{H}(\tau+\tau_n)}. \end{aligned} \tag{4.44}$$

Thus, the evolution operator for the composite evolution (as enclosed by the dashed box) in Fig. 4.9 is equal to $\hat{U}_{\rm com}|_{\tau\to(\tau+\tau_n)}$. Therefore, inclusion of the finite duration τ_n of the controlled nuclear spin rotation amounts to replacing τ with $(\tau + \tau_n)$ in Eq. (4.22). Note that the nuclear spin relaxation time and decoherence time $\gtrsim 1$ ms [25, 49] are much longer than $\tau_n \sim 1$ μs and hence have negligible influence on this result.

4.8.5 Bayesian inference

The Bayesian inference provides a posterior distribution based on a prior distribution and its associated likelihood function. We use the first estimation step of A in the main text as an example.

The prior distribution of A is given by the Gaussian distribution $\mathcal{N}(A_0, \Delta_0)$,

$$f(A) = \frac{1}{\sqrt{2\pi}\Delta_0}\exp\left(-\frac{(A - A_0)^2}{2\Delta_0^2}\right).$$

And we construct the quantum estimation circuit $M(\tau_1)$ based on the prior information we have, with the constraints in Eq. (4.26). The circuit $M(\tau_1)$ produces an estimator Z_1 of $\langle\hat{Z}\rangle_1 = \cos(A\tau_1)$, which obeys the Gaussian distribution $\mathcal{N}(\langle\hat{Z}\rangle, \zeta)$. This information is converted to the distribution of $\bar{A}_1$ by the linear expansion. $\bar{A}_1$ also obeys the Gaussian distribution $\mathcal{N}(A, \bar{\Delta}_1)$,

$$f(\bar{A}_1 \mid A) = \frac{1}{\sqrt{2\pi}\Delta_1}\exp\left(-\frac{(\bar{A}_1 - A)^2}{2\bar{\Delta}_1^2}\right). \tag{4.45}$$

The distribution of $\bar{A}_1$ is conditioned on A because it is obtained from the prior distribution of A. Thus $f(\bar{A}_1 \mid A)$ is considered as the likelihood of $\bar{A}_1$. Note that Eq. (4.45) can also be interpreted as the Gaussian distribution of A with the mean value of $\bar{A}_1$ and the standard deviation of $\bar{\Delta}_1$, which we have done in the first part of Sec. 4.6.1.

The posterior distribution of A is computed according to the Bayes' rule

$$f(A \mid \bar{A}_1) = \frac{f(\bar{A}_1 \mid A) \cdot f(A)}{f(\bar{A}_1)}.$$

The joint distribution $f(\bar{A}_1 \mid A) \cdot f(A)$ is

$$f(\bar{A}_1 \mid A) \cdot f(A) = \frac{1}{\sqrt{2\pi}\Delta_0} \exp\left(-\frac{(A - A_0)^2}{2\Delta_0^2}\right) \times \frac{1}{\sqrt{2\pi}\Delta_1} \exp\left(-\frac{(\bar{A}_1 - A)^2}{2\bar{\Delta}_1^2}\right).$$

The exponent of the above equation is

$$\begin{aligned} -\frac{(A - A_0)^2}{2\Delta_0^2} - \frac{(\bar{A}_1 - A)^2}{2\bar{\Delta}_1^2} &= -\frac{1}{2}\left[\left(\frac{1}{\Delta_0^2} + \frac{1}{\bar{\Delta}_1^2}\right)A^2 - 2\left(\frac{A_0}{\Delta_0^2} + \frac{A_1}{\bar{\Delta}_1^2}\right)A + \cdots\right] \\ &= -\frac{(A - A_1)^2}{2\Delta_1^2} + g(\bar{A}_1), \end{aligned}$$

where

$$A_1 = \frac{A_0/\Delta_0^2 + \bar{A}_1/\bar{\Delta}_1^2}{1/\Delta_0^2 + 1/\bar{\Delta}_1^2}, \tag{4.46a}$$

$$\frac{1}{\Delta_1^2} = \frac{1}{\Delta_0^2} + \frac{1}{\bar{\Delta}_1^2}. \tag{4.46b}$$

These are the formulae used in Eq. (4.27a) and (4.27b). Since the distribution $f(\bar{A}_1)$ has no dependence on A, the posterior distribution $f(A \mid \bar{A}_1)$ is the Gaussian distribution centered at A_1 with the standard deviation Δ_1.

As seen in Eqs. (4.46), the posterior distribution contains both the resources spent in obtaining the prior information and the resources spent in the estimation circuit $M(\tau_1)$. As a result, the standard deviation of the posterior distribution Δ_1 is smaller than Δ_0 and $\bar{\Delta}_1$.

4.9 Acknowledgments

The text of chapter 4, in part, is a reprint of the material that has been submitted for publication as Bang, K.; Yang, W.; Sham, L. J. *Quantum measurement of hyper-*

fine interaction in nitrogen-vacancy center. The co-authors in this publication directed, supervised, and co-worked on the research which forms the basis of this chapter.

Chapter 5

Conclusions

5.1 Summary

In this dissertation, we have studied on the optical initialization of the nitrogen nuclear spin in the NV center and the quantum measurement of the hyperfine interaction between the electron spin and ^{15}N nuclear spin in the NV center.

In chapter 3, we have calculated the dynamics of the optical initialization of the nitrogen nuclear spin in the NV center under optical pumping. The nitrogen nuclear spin can be deterministically prepared in a given pure state by incoherent optical pumping. So far, the known understanding of the optical initialization mechanism was not sufficient to explain the earlier experiment. Our semi-classical calculation successfully explains the experimental data and provides a quantitative understanding of the initialization mechanism of the nitrogen nuclear spin which is based on the level anticrossing in the excited state. The mechanism is a competition between the two spin-mixing transitions in the excited state due to the hyperfine interaction. Since one transition is dominant over the other, a large amount of polarization can be achieve not only near the level anticrossing ($B \approx 500$ G) but over a wide range of the magnetic field. While the experiments using the nitrogen nuclear spins have not considered the effect of the local strain in the NV center, we have found that the local strain induces the depolarization the nuclear spin at the level anticrossing. As a result, the optimal point of the initialization is not at the level anticrossing but near $B \approx 470$ G for the ^{15}N nuclear spin and $B \approx 580$ G for the ^{14}N nuclear spin. We also suggest that a weaker pumping at these

optimal magnetic fields produces a better purity of the prepared qubit.

In chapter 4, we have proposed a quantum measurement protocol to estimate the hyperfine interaction between the electron spin and the ^{15}N nuclear spin in the NV center. The underlying concept of the protocol is the mixed-state quantum computation (DQC1) with the spin-echo technique. The spin-echo eliminates the independent dynamics of the electron spin and the nuclear spin but keeps only the hyperfine interaction in the coherence of the electron spin. While most quantum metrological techniques require pure qubits and entanglement between them, the suggested protocol does not require the preparation of the ^{15}N nuclear spin and entanglement. Instead, the protocol utilizes the total duration of the operations $\sum \tau$ as a resource of the estimation. In principle, by exponentially increasing the operation time, the precision of the estimation approaches the quantum metrology limit (QML). In the presence of the nuclear spin rotation error, the precision of the estimation still approaches the QML if the error in the rotation angle is a few %. In other words, the protocol is robust against the nuclear spin rotation error. In the presence of the electron spin decoherence, the estimation is close to the QML when the operation time is much shorter than the coherence time of the electron spin ($\tau \ll T_2^e$). However, τ cannot increase arbitrary large because the decoherence erases the coherence of the electron spin where the information of the hyperfine interaction is stored. Thus τ increases at each step only until $\tau = T_2^e/2$ where the precision of the estimation is optimal. For further estimation steps, τ is fixed and the resulting precision of the estimation follows the trend of the standard quantum limit (SQL). In the benefit of the QML scaling in the first a few steps, the overall estimation still exceeds the SQL.

5.2 Future works

First of all, our two studies will contribute to the practical use of the nitrogen nuclear spin in the NV center as a quantum memory. In quantum computation, the initialization and the coherent control of a qubit are key requirements for the implementation of quantum computers [17]. Our work on the initialization of the nitrogen nuclear spin proposes the optimal conditions to increase the purity of the prepared nitrogen spin. The

work on the estimation of the hyperfine interaction in the NV center provides a precise quantum measurement technique of the hyperfine interaction, which allows a coherent control of the nitrogen nuclear spin with a higher accuracy. By improving the yield of the initialization and the accuracy of the coherent control, the nitrogen nuclear spin in the NV center approaches the realization of a room-temperature quantum memory.

There are still a lot of work to be done for the nitrogen nuclear spin as a quantum memory. First of all, the initialization mechanism needs to be robust against the alignment of the magnetic field. While our proposal for the initialization of the nitrogen nuclear spin works if the external magnetic field is well-aligned, it does not work even for a small misalignment ($\sim 1^\circ$). However, it is important to initialize several qubits together with a single operation for a scalable quantum memory. For this purpose, the robust initialization mechanism should be introduced in the future.

For a room-temperature scalable quantum memory, the entanglement between flying qubits (photons) and stationary qubits (electron and nuclear spins in the NV center) is to be created at room temperature. So far, the spin-photon entanglement in the NV center has only been achieved at low temperature [64]. At room temperature, the local strain and the vibration of the NV center prevent a generation of the entanglement. While a recent study shows that the local strain can be electrically tuned [4], the vibration of the diamond lattice is difficult to be frozen at room temperature. Thus the creation of the entanglement may be related with the vibrational mode of the NV center, which has been intensively studied [1, 24, 45].

Readout of the nitrogen spin state is another important issue to be done in the future. A single-shot readout of the nitrogen nuclear spin has been demonstrated recently, but the timescale of the measurement is about 5 ms [49], which is long with compared to the operation time of the nuclear spin ($0.1-50\,\mu$s). The slow readout of the qubit may drop the efficiency of a quantum memory. One possible solution for the fast readout of the nuclear spin is using the mapping of the nuclear spin to the electron spin and the subsequent readout of the electron spin [25]. In this case, a single-shot readout of the electron spin at room temperature needs to be accomplished [7].

We would like to close this dissertation with mentioning possible applications of the quantum measurement protocol suggested in chapter 4. The proposed method is de-

signed to measure the hyperfine interaction in the NV center efficiently. We claim that our measurement method can be extended to other coupled systems such as quantum dots or trapped ions. In particular, it can be applied to the system in which only one qubit can be initialized but the other is not. In quantum computation, a precise knowledge of the coupling constant is important to minimize an error in the creation of the entanglement. Our method can estimate the coupling constant between two qubits with spending less amount of resources. As a result, the operation error from the detuning may drop to 0.001%, which is a requirement for quantum computation [17].

Bibliography

[1] Tesfaye A. Abtew, Y. Y. Sun, Bi-Ching Shih, Pratibha Dev, S. B. Zhang, and Peihong Zhang. Dynamic jahn-teller effect in the nv^- center in diamond. *Phys. Rev. Lett.*, 107:146403, 2011.

[2] V. M. Acosta, A. Jarmola, E. Bauch, and D. Budker. Optical properties of the nitrogen-vacancy singlet levels in diamond. *Phys. Rev. B*, 82(20):201202, 2010.

[3] G. Balasubramanian, P. Neumann, D. Twitchen, M. Markham, R. Kolesov, N. Mizuochi, J. Isoya, J. Achard, J. Beck, J. Tissler, V. Jacques, P. R. Hemmer, F. Jelezko, and J. Wrachtrup. Ultralong spin coherence time in isotopically engineered diamond. *Nature Mater.*, 8(5):383–387, 2009.

[4] L. C. Bassett, F. J. Heremans, C. G. Yale, B. B. Buckley, and D. D. Awschalom. Electrical tuning of single nitrogen-vacancy center optical transitions enhanced by photoinduced fields. *Phys. Rev. Lett.*, 107:266403, 2011.

[5] A. Batalov, V. Jacques, F. Kaiser, P. Siyushev, P. Neumann, L. J. Rogers, R. L. McMurtrie, N. B. Manson, F. Jelezko, and J. Wrachtrup. Low temperature studies of the excited-state structure of negatively charged nitrogen-vacancy color centers in diamond. *Phys. Rev. Lett.*, 102(19):195506, 2009.

[6] S. Boixo and R. D. Somma. Parameter estimation with mixed-state quantum computation. *Phys. Rev. A*, 77:052320, 2008.

[7] B. B. Buckley, G. D. Fuchs, L. C. Bassett, and D. D. Awschalom. Spin-light coherence for single-spin measurement and control in diamond. *Science*, 330(6008):1212–1215, 2010.

[8] L. Childress, M. V. Gurudev Dutt, J. M. Taylor, A. S. Zibrov, F. Jelezko, J. Wrachtrup, P. R. Hemmer, and M. D. Lukin. Coherent dynamics of coupled electron and nuclear spin qubits in diamond. *Science*, 314(5797):281–285, 2006.

[9] L. Childress, J. M. Taylor, A. S. Sørensen, and M. D. Lukin. Fault-tolerant quantum communication based on solid-state photon emitters. *Phys. Rev. Lett.*, 96:070504, 2006.

[10] I. Chiorescu, Y. Nakamura, C. J. P. M. Harmans, and J. E. Mooij. Coherent quantum dynamics of a superconducting flux qubit. *Science*, 299(5614):1869–1871, 2003.

[11] J. I. Cirac and P. Zoller. Quantum computations with cold trapped ions. *Phys. Rev. Lett.*, 74:4091–4094, 1995.

[12] B. Dakić, V. Vedral, and Č. Brukner. Necessary and sufficient condition for nonzero quantum discord. *Phys. Rev. Lett.*, 105(19):190502, 2010.

[13] A. Datta, S. T. Flammia, and C. M. Caves. Entanglement and the power of one qubit. *Phys. Rev. A*, 72:042316, 2005.

[14] A. Datta, A. Shaji, and C. M. Caves. Quantum discord and the power of one qubit. *Phys. Rev. Lett.*, 100(5):050502, 2008.

[15] A. Datta and G. Vidal. Role of entanglement and correlations in mixed-state quantum computation. *Phys. Rev. A*, 75:042310, 2007.

[16] P. Delaney, J. C. Greer, and J. A. Larsson. Spin-polarization mechanisms of the nitrogen-vacancy center in diamond. *Nano Letters*, 10:610–614, 2010.

[17] David P. DiVincenzo. The physical implementation of quantum computation. *Fortschritte der Physik*, 48(9-11):771–783, 2000.

[18] M. W. Doherty, F. Dolde, H. Fedder, F. Jelezko, J. Wrachtrup, N. B. Manson, and L. C. L. Hollenberg. Theory of the ground-state spin of the nv^- center in diamond. *Phys. Rev. B*, 85:205203, 2012.

[19] M W Doherty, N B Manson, P Delaney, and L C L Hollenberg. The negatively charged nitrogen-vacancy centre in diamond: the electronic solution. *New Journal of Physics*, 13(2):025019, 2011.

[20] J. P. Dowling. Quantum optical metrology –the lowdown on high-n00n states. *Contemp. Phys.*, 49(2):125–143, 2008.

[21] J. A. Dunningham. Using quantum theory to improve measurement precision. *Contemp. Phys.*, 47(5):257–267, 2006.

[22] M. V. G. Dutt, L. Childress, L. Jiang, E. Togan, J. Maze, F. Jelezko, A. S. Zibrov, P. R. Hemmer, and M. D. Lukin. Quantum register based on individual electronic and nuclear spin qubits in diamond. *Science*, 316:1312–1316, 2007.

[23] S. Felton, A. M. Edmonds, M. E. Newton, P. M. Martineau, D. Fisher, D. J. Twitchen, and J. M. Baker. Hyperfine interaction in the ground state of the negatively charged nitrogen vacancy center in diamond. *Phys. Rev. B*, 79:075203, 2009.

[24] Kai-Mei C. Fu, Charles Santori, Paul E. Barclay, Lachlan J. Rogers, Neil B. Manson, and Raymond G. Beausoleil. Observation of the dynamic jahn-teller effect in the excited states of nitrogen-vacancy centers in diamond. *Phys. Rev. Lett.*, 103:256404, 2009.

[25] G. D. Fuchs, G. Burkard, P. V. Klimov, and D. D. Awschalom. A quantum memory intrinsic to single nitrogen-vacancy centres in diamond. *Nature Phys.*, 7(10):789–793, 2011.

[26] G. D. Fuchs, V. V. Dobrovitski, R. Hanson, A. Batra, C. D. Weis, T. Schenkel, and D. D. Awschalom. Excited-state spectroscopy using single spin manipulation in diamond. *Phys. Rev. Lett.*, 101(11):117601, 2008.

[27] G. D. Fuchs, V. V. Dobrovitski, D. M. Toyli, F. J. Heremans, and D. D. Awschalom. Gigahertz dynamics of a strongly driven single quantum spin. *Science*, 325:1520, 2009.

[28] G. D. Fuchs, V. V. Dobrovitski, D. M. Toyli, F. J. Heremans, C. D. Weis, T. Schenkel, and D. D. Awschalom. Excited-state spin coherence of a single nitrogen-vacancy centre in diamond. *Nature Phys.*, 6:668–672, 2010.

[29] T. Gaebel, M. Domhan, I. Popa, C. Wittmann, P. Neumann, F. Jelezko, J. R. Rabeau, N. Stavrias, A. D. Greentree, S. Prawer, J. Meijer, J. Twamley, P. R. Hemmer, and J. Wrachtrup. Room-temperature coherent coupling of single spins in diamond. *Nature Phys.*, 2(6):408–413, 2006.

[30] A. Gali, M. Fyta, and E. Kaxiras. Ab initio supercell calculations on nitrogen-vacancy center in diamond: Electronic structure and hyperfine tensors. *Phys. Rev. B*, 77:155206, 2008.

[31] Adam Gali. Identification of individual ^{13}C isotopes of nitrogen-vacancy center in diamond by combining the polarization studies of nuclear spins and first-principles calculations. *Phys. Rev. B*, 80:241204, 2009.

[32] V. Giovannetti, S. Lloyd, and L. Maccone. Quantum-enhanced measurements: Beating the standard quantum limit. *Science*, 306(5700):1330–1336, 2004.

[33] V. Giovannetti, S. Lloyd, and L. Maccone. Quantum metrology. *Phys. Rev. Lett.*, 96:010401, 2006.

[34] G. Goldstein, P. Cappellaro, J. R. Maze, J. S. Hodges, L. Jiang, A. S. Sørensen, and M. D. Lukin. Environment-assisted precision measurement. *Phys. Rev. Lett.*, 106:140502, 2011.

[35] A. Gruber, A. Dräbenstedt, C. Tietz, L. Fleury, J. Wrachtrup, and C. von Borczyskowski. Scanning confocal optical microscopy and magnetic resonance on single defect centers. *Science*, 276(5321):2012–2014, 1997.

[36] J. Harrison, M. J. Sellars, and N. B. Manson. Optical spin polarisation of the n-v centre in diamond. *J. Lumin.*, 107(1-4):245–248, 2004.

[37] Michał Horodecki, Paweł Horodecki, and Ryszard Horodecki. Mixed-state entanglement and distillation: Is there a "bound" entanglement in nature? *Phys. Rev. Lett.*, 80:5239–5242, 1998.

[38] V. Jacques, P. Neumann, J. Beck, M. Markham, D. Twitchen, J. Meijer, F. Kaiser, G. Balasubramanian, F. Jelezko, and J. Wrachtrup. Dynamic polarization of single nuclear spins by optical pumping of nitrogen-vacancy color centers in diamond at room temperature. *Phys. Rev. Lett.*, 102(5):057403, 2009.

[39] F. Jelezko, T. Gaebel, I. Popa, M. Domhan, A. Gruber, and J. Wrachtrup. Observation of coherent oscillation of a single nuclear spin and realization of a two-qubit conditional quantum gate. *Phys. Rev. Lett.*, 93(13):130501, 2004.

[40] F. Jelezko, I. Popa, A. Gruber, C. Tietz, J. Wrachtrup, A. Nizovtsev, and S. Kilin. Single spin states in a defect center resolved by optical spectroscopy. *Appl. Phys. Lett.*, 81:2160–2162, 2002.

[41] E. Knill and R. Laflamme. Power of one bit of quantum information. *Phys. Rev. Lett.*, 81:5672–5675, 1998.

[42] B. P. Lanyon, M. Barbieri, M. P. Almeida, and A. G. White. Experimental quantum computing without entanglement. *Phys. Rev. Lett.*, 101:200501, 2008.

[43] J. A. Larsson and P. Delaney. Electronic structure of the nitrogen-vacancy center in diamond from first-principles theory. *Phys. Rev. B*, 77(16):165201, 2008.

[44] A. Lenef and S. C. Rand. Electronic structure of the n-v center in diamond: Theory. *Phys. Rev. B*, 53:13441–, 1996.

[45] J R Maze, A Gali, E Togan, Y Chu, A Trifonov, E Kaxiras, and M D Lukin. Properties of nitrogen-vacancy centers in diamond: the group theoretic approach. *New Journal of Physics*, 13(2):025025, 2011.

[46] J. R. Maze, P. L. Stanwix, J. S. Hodges, S. Hong, J. M. Taylor, P. Cappellaro, L. Jiang, M. V. Gurudev Dutt, E. Togan, A. S. Zibrov, A. Yacoby, R. L. Walsworth, and M. D. Lukin. Nanoscale magnetic sensing with an individual electronic spin in diamond. *Nature*, 455(7213):644–647, 2008.

[47] P. Meystre and M. Sargent. *Elements of Quantum Optics*. Springer, Berlin, 2007.

[48] Boris Naydenov, Florian Dolde, Liam T. Hall, Chang Shin, Helmut Fedder, Lloyd C. L. Hollenberg, Fedor Jelezko, and Jörg Wrachtrup. Dynamical decoupling of a single-electron spin at room temperature. *Phys. Rev. B*, 83:081201, 2011.

[49] P. Neumann, J. Beck, M. Steiner, F. Rempp, H. Fedder, P. Hemmer, J. Wrachtrup, and F. Jelezko. Single-shot readout of a single nuclear spin. *Science*, 329:542, 2010.

[50] P. Neumann, R. Kolesov, B. Naydenov, J. Beck, F. Rempp, M. Steiner, V. Jacques, G. Balasubramanian, M. L. Markham, D. J. Twitchen, S. Pezzagna, J. Meijer, J. Twamley, F. Jelezko, and J. Wrachtrup. Quantum register based on coupled electron spins in a room-temperature solid. *Nat Phys*, 6:249–253, 2010.

[51] P. Neumann, N. Mizuochi, F. Rempp, P. Hemmer, H. Watanabe, S. Yamasaki, V. Jacques, T. Gaebel, F. Jelezko, and J. Wrachtrup. Multipartite entanglement among single spins in diamond. *Science*, 320(5881):1326–1329, 2008.

[52] M. A. Nielsen and I. L. Chuang. *Quantum Computation and Quantum Information*. Cambridge University Press, Cambridge, 2000.

[53] J. R. Petta, A. C. Johnson, J. M. Taylor, E. A. Laird, A. Yacoby, M. D. Lukin, C. M. Marcus, M. P. Hanson, and A. C. Gossard. Coherent manipulation of coupled electron spins in semiconductor quantum dots. *Science*, 309(5744):2180–2184, 2005.

[54] D. Poulin, R. Blume-Kohout, R. Laflamme, and H. Ollivier. Exponential speedup with a single bit of quantum information: Measuring the average fidelity decay. *Phys. Rev. Lett.*, 92:177906, 2004.

[55] J. R. Rabeau, P. Reichart, G. Tamanyan, D. N. Jamieson, S. Prawer, F. Jelezko, T. Gaebel, I. Popa, M. Domhan, and J. Wrachtrup. Implantation of labelled single nitrogen vacancy centers in diamond using [sup 15]n. *Applied Physics Letters*, 88(2):023113, 2006.

[56] L. Robledo, H. Bernien, T. van der Sar, and R. Hanson. Spin dynamics in the optical cycle of single nitrogen-vacancy centres in diamond. *New Journal of Physics*, 13(2):025013, 2011.

[57] L. Robledo, L. Childress, H. Bernien, B. Hensen, P. F. A. Alkemade, and R. Hanson. High-fidelity projective read-out of a solid-state spin quantum register. *Nature*, 477(7366):574–578, 2011.

[58] L J Rogers, R L McMurtrie, M J Sellars, and N B Manson. Time-averaging within the excited state of the nitrogen-vacancy centre in diamond. *New Journal of Physics*, 11(6):063007, 2009.

[59] J. J. Sakurai. *Modern Quantum Mechanics*. Addison-Wesley, Massachusetts, 1994.

[60] Fazhan Shi, Xing Rong, Nanyang Xu, Ya Wang, Jie Wu, Bo Chong, Xinhua Peng, Juliane Kniepert, Rolf-Simon Schoenfeld, Wolfgang Harneit, Mang Feng, and

Jiangfeng Du. Room-temperature implementation of the deutsch-jozsa algorithm with a single electronic spin in diamond. *Phys. Rev. Lett.*, 105:040504–, 2010.

[61] B. Smeltzer, J. McIntyre, and L. Childress. Robust control of individual nuclear spins in diamond. *Phys. Rev. A*, 80(5):050302, 2009.

[62] M. Steiner, P. Neumann, J. Beck, F. Jelezko, and J. Wrachtrup. Universal enhancement of the optical readout fidelity of single electron spins at nitrogen-vacancy centers in diamond. *Phys. Rev. B*, 81:035205, 2010.

[63] J. M. Taylor, P. Cappellaro, L. Childress, L. Jiang, D. Budker, P. R. Hemmer, A. Yacoby, R. Walsworth, and M. D. Lukin. High-sensitivity diamond magnetometer with nanoscale resolution. *Nat Phys*, 4(10):810–816, 2008.

[64] E. Togan, Y. Chu, A. S. Trifonov, L. Jiang, J. Maze, L. Childress, M. V. G. Dutt, A. S. Sorensen, P. R. Hemmer, A. S. Zibrov, and M. D. Lukin. Quantum entanglement between an optical photon and a solid-state spin qubit. *Nature*, 466:730–734, 2010.

[65] L. M. K. Vandersypen and I. L. Chuang. Nmr techniques for quantum control and computation. *Rev. Mod. Phys.*, 76:1037–1069, 2005.

[66] V. Vedral, M. B. Plenio, M. A. Rippin, and P. L. Knight. Quantifying entanglement. *Phys. Rev. Lett.*, 78(12):2275–2279, 1997.

[67] J. Wrachtrup and F. Jelezko. Processing quantum information in diamond. *Journal of Physics: Condensed Matter*, 18(21):S807, 2006.

[68] W. Yang, Z. Y. Wang, and R. B. Liu. Preserving qubit coherence by dynamical decoupling. *Frontiers of Physics*, 6:2, 2011.